5-2010

Neutron scattering study of the high Tc superconductors

Jun Zhao
Department of Physics and Astronomy, jzhao5@utk.edu

To the Graduate Council:

I am submitting herewith a dissertation written by Jun Zhao entitled "Neutron scattering study of the high Tc superconductors." I have examined the final electronic copy of this dissertation for form and content and recommend that it be accepted in partial fulfillment of the requirements for the degree of Doctor of Philosophy, with a major in Physics.

Pengcheng Dai, Major Professor

We have read this dissertation and recommend its acceptance:

Pengcheng Dai, Jaime A. Fernandez-Baca, Takeshi Egami, Norman Mannella, James R. Thompson

Accepted for the Council:

Carolyn R. Hodges

Vice Provost and Dean of the Graduate School

(Original signatures are on file with official student records.)

To the Graduate Council:

I am submitting herewith a dissertation written by Jun Zhao entitled "Neutron scattering study of high T_c superconductors" I have examined the final electronic copy of this dissertation for form and content and recommend that it be accepted in partial fulfillment of the requirements for the degree of Doctor of Philosophy, with a major in Physics.

Pengcheng Dai

Major Professor

We have read this dissertation
and recommend its acceptance:

Takeshi Egami

James R. Thompson

Jaime A. Fernandez-Baca

Norman Mannella

Accepted for the Council:

Carolyn R. Hodges
Vice Provost
and Dean of the Graduate School

(Original signatures are on file with official student records.)

Neutron scattering study of high T_c superconductors

A Dissertation

Presented for the

Doctor of Philosophy

Degree

The University of Tennessee, Knoxville

Jun Zhao

May 2010

Dedication

To my parents.

Acknowledgments

First I am greatly indebted to my advisor, Professor Pengcheng Dai, for his guidance and help throughout the years. His passion for research and great insight have been a great inspiration to me.

I feel grateful to all my colleagues in neutron scattering group at UTK for their support and help. I would also like to thank Shiliang Li, Stephen Wilson, Clarina da la Cruz and Songxue Chi for working closely with me on neutron scattering experiments.

I appreciate Dr. Jeff Lynn, Dr. Qing Huang, Dr. D. T. Adroja, Dr. R. Bewley, Dr. L.P. Regnualt and other instrument scientists at NCNR, ISIS, ILL for providing technical assistance in the neutron scattering experiments.

I send my thanks to collaborators in Professor Jiangping Hu's group and Dr. Daoxin Yao from Purdue University for helpful discussions in data analysis.

I thank Dr. Zhongxian Zhao, Dr. Nanlin Wang and Dr. Xianhui Chen's groups for providing excellent samples for us.

Last but not the least, my gratitude also extends to my family who have been assisting, supporting and caring for me all of my life.

Abstract

We carried out systematic neutron scattering experiments to investigate the magnetic properties and their relationship to the high-T_c superconductivity, when the materials are tuned from their antiferromagnetic (AF) parent compounds to the superconducting regime.

We observed resonance mode in the electron doped cuprate $Nd_{1.85}Ce_{0.15}CuO_4$, demonstrating that the resonance is a general phenomenon in cuprate superconductors regardless of hole- or electron-doping. In $Pr_{0.88}LaCe_{0.12}CuO_4$, the local susceptibility displays two distinct energy scales that are broadly consistent with the bosonic modes revealed by scanning tunneling microscopy experiments. These results indicate the presence of very strong electron spin excitations couplings in electron doped cuprates.

Shortly after the discovery of high-T_c superconductivity in the Fe pnictides, we discovered that the magnetic phase diagram of $CeFeAsO_{1-x}F_x$ is remarkably similar to that of the cuprates. Besides CeFeAsO, similar magnetic and lattice structures are also observed in PrFeAsO and $SrFe_2As_2$ systems. Neutron scattering measurements show that in $SrFe_2As_2$, the spectrum of magnetic excitations consists of a Bragg peak at the elastic position, a spin gap, and sharp spin-wave excitations at higher energies. Based on the observed dispersion relation, we estimated the effective magnetic exchange coupling using a Heisenberg model.

In order to study the nature of the exchange interactions in the parent compound of Fe pnictides, we studied the high energy spin-wave excitations in $CaFe_2As_2$. Although the spin waves in the entire Brillouin zone can be described by an effective three-dimensional anisotropic Heisenberg Hamiltonian, the magnetism in this system is neither purely local nor purely itinerant; rather it is a complicated mix of the two.

When the Fe pnictide is tuned into superconducting regime with doping, the low energy spin fluctuation is dominated by a resonance mode. In the optimally electron doped

$BaFe_{1.9}Ni_{0.1}As_2$, application of a magnetic field that suppresses the superconductivity and superconducting gap energy also reduces the intensity and energy of the resonance. These results suggest that the energy of the resonance is proportional to the electron pairing energy, and thus indicate that spin fluctuations are intimately related to the mechanism of high T_c superconductivity.

Preface

Portions of this dissertation are derived from published work. The publication information of each work is listed with its corresponding chapter.

Chapter 2:

Jun Zhao, Pengcheng Dai, Shiliang Li, Paul G. Freeman, Y. Onose, Y. Tokura

Phys. Rev. Lett. **99** 017001 (2007)

Chapter 4:

Jun Zhao, Q. Huang, C. de la Cruz, S. Li, J. W. Lynn, Y. Chen, M. A. Green, G. F. Chen, G. Li, Z. Li, J. L. Luo, N. L. Wang, Pengcheng Dai,

Nature Materials **75**, 953 (2008)

Chapter 5:

Jun Zhao, Q. Huang, Clarina de la Cruz, J. W. Lynn, M. D. Lumsden, Z. A. Ren, Jie Yang, Xiaolin Shen, Xiaoli Dong, Zhongxian Zhao, Pengcheng Dai

Phys. Rev. B **78** 132504 (2008)

Chapter 6:

Jun Zhao, W. Ratcliff II, J. W. Lynn, G. F. Chen, J. L. Luo, N. L. Wang, Jiangping Hu, Pengcheng Dai

Phys. Rev. B **78**, 140504 (R) (2008).

Chapter 7:

Jun Zhao, Dao-Xin Yao, Shiliang Li, Tao Hong, Y. Chen, S. Chang, W. Ratcliff II, J. W. Lynn, H. A. Mook, G. F. Chen, J. L. Luo, N. L. Wang, E. W. Carlson, Jiangping Hu, Pengcheng Dai

Phys. Rev. Lett. **101**, 167203 (2008)

Chapter 8:

Jun Zhao, D. T. Adroja, Dao-Xin Yao, R. Bewley, Shiliang Li, X. F. Wang, G. Wu, X. H. Chen, Jiangping Hu, Pengcheng Dai

Nature Physics **5**, 555 (2009)

Contents

List of Figures

Chapter 1

Introduction

1.1 Conventional superconductivity

Superconductors are the materials characterized by zero resistivity and exclusion of the interior magnetic field (Meissner effect) below certain critical temperature (superconducting transition temperature T_c) [1, 2]. The superconductivity phenomenon was first discovered by Karmerlingh Onnes in 1911 when he was measuring the resistivity of mercury at low temperature using liquid helium as a refrigerant [1]. The resistivity of mercury abruptly dropped to close to zero below 4.2 K, which signified the discovery of superconductivity. Shortly after that, superconductivity was also observed in various other materials including simple elements such as tin, lead and some metallic alloys. These simplest superconductors with relatively low T_cs are referred as conventional superconductors. The mechanism of conventional superconductivity was not clear until Bardeen, Cooper and Schrieffer developed the BCS theory in 1957 (ref. [3]), 46 years after the initial discovery. In the BCS theory, superconductivity is a macroscopic effect which results from Bose condensation of electron "Cooper pairs". The key question concerning the pairing mechanism of the electron "Cooper pair" can be understood as the consequence of strong electron phonon coupling: when an electron moving through a conductor will attract nearby positive charges in the lattice and induce some deformation on the lattice. This deformation of the lattice causes another electron, with opposite "spin", to move into the region of higher positive charge density. The two electrons are then held together through the lattice vibrations

(phonons) with a certain binding energy, forming a "Cooper pair" as a boson [3], which carries the supercurrent with no resistance when the thermal fluctuation energy is much lower than the electron pair binding energy at low temperature. In the frame work of BCS theory, the "Cooper pair" is electron pair in singlet state with opposite spin and momentum. The symmetry of conventional superconducting gap is isotropic s wave (momentum independent) with total spin S=0. BCS theory gives the superconducting transition temperature as the function of the electron-phonon coupling potential and the Debye cutoff energy in a simple form:

$$k_B T_c = 1.14 E_D e^{-1/N(0)V} \tag{1.1}$$

where E_D is the Debye energy, $N(0)$ is the density of states on Fermi surface and V is the electron phonon coupling constant. In standard BCS theory, the T_c of the conventional superconductor is usually lower than 30 K due to the weak electron phonon coupling and low Debye energy in realistic materials.

1.2 High T_c superconductivity

1.2.1 Discovery of high T_c superconductivity

In 1986, high T_c superconductivity was discovered by Muller et al [4] in the cuprate $La_{2-x}Ba_xCuO_4$ with $T_c = 30$ K which is higher than the superconductors known at the time. This discovery fascinated the whole world and tremendous effort had been put forth searching for new high T_c superconductors after the initial break through. A lot of similar cuprate superconductors such as $YBa_2Cu_3O_{7-\delta}$ ($T_c = 90$ K) and $HgBa_2Ca_2Cu_3O_8$ ($T_c = 163$ K under pressure) were discovered [5, 6], pushing the T_c way above the liquid nitrogen temperature. The high T_c superconductors are probably one of the most important and potentially most useful discoveries ever, not only because the high T_c above liquid nitrogen temperature makes the widespread technological applications in industry possible, but also because the physics behind the phenomenon is so complicated and it challenged our understanding of condensed matter physics. Theoretical calculations showed that the electron phonon coupling strength in cuprate is not strong enough to lead to so high T_c,

suggesting a deviation from the standard BCS theory. In addition, besides the very high transition temperature, cuprate superconductors display exotic properties even in the normal state (above T_c). For example, the resistivity of optimally doped cuprate exhibits linear temperature dependence over wide temperature ranges, which is deviated from the Fermi liquid behavior.

1.2.2 Magnetic structure and phase diagram of high T_c superconductors

In conventional superconductors, magnetic moments in the lattice are always harmful for superconductivity because the "pair breaking" interaction between the moment and "Cooper pairs". Surprisingly, all the high T_c cuprate superconductors have universal "parent" compounds which are antiferromagnetic (Mott) insulators. In general, the parent compounds of cuprates are comprised of one or more sheets of flat copper oxygen layers separated by rare earth ions. Although the conventional band theory suggests the $d_{x^2-y^2}$ orbital of Cu^{2+} contributes to the density of states near Fermi surface and the parent compound should be metal, it is actually an insulator because of the large electron on-site Coulomb repulsion which is not considered in conventional band theory. On-site Coulomb repulsion splits the conduction band into two Hubbard bands and only the lower band is filled by electrons. Since there is a several eV energy gap between upper band and lower band, the unpaired $d_{x^2-y^2}$ electron of copper is localized in each site and carries 1/2 spin which is responsible for the magnetic properties of cuprates.

Neutron scattering experiment showed that the copper spin is antiferromagnetically ordered in the parent compound [13], the static order is rapidly suppressed and the superconductivity appears with doping charge carriers (holes or electrons) into the copper oxygen plane. There are several ways of doping, including replacing rare earth ions by other metal ions with different chemical valences; or introducing/removing oxygen into/from the system. The region between the copper oxygen layers is referred as the "charge reservoir". The lattice and magnetic structure of a typical hole doped cuprate $La_{2-x}Sr_xCuO_4$ is depicted in Fig. 1.1 (ref. [13]). Each copper is surrounded by by an octahedron of oxygen sites. Holes are doped into the system by substituting La^{3+} with Sr^{2+}. When sufficient holes or electrons are doped into the CuO_2 planes, the static antiferromagnetic order is

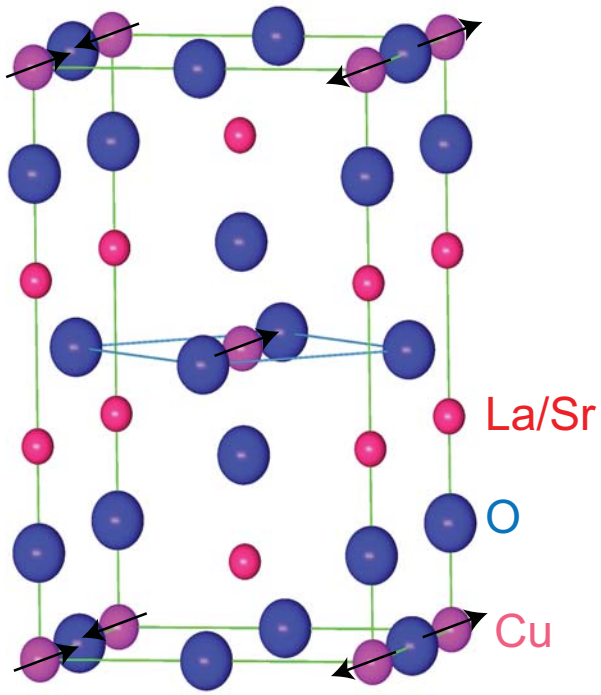

Figure 1.1: Magnetic and lattice structure of single layed cuprate $La_{2-x}Sr_xCuO_4$. The arrows denote the spin directions of Cu.

suppressed and superconductivity emerges, resulting a general phase diagram shown in Fig. 1.2. After the static order is suppressed, the T_c increases as the increasing doping level and reaches a maximum value termed optimum doping. The T_c decreases as further doping beyond the optimum value, forming a superconducting dome (Fig. 1.2). Although the static antiferromagntic order is suppressed, the antiferomagnetic fluctuations persists in all the superconducting concentrations. The vicinity of superconductivity to a magnetically ordered state is the key motivation to consider the mechanism of the high T_c superconductivity is linked to magnetic degrees of freedom. Unlike phonon in conventional superconductors, the magnon is much more difficult to measure and to be described. In spite of more than twenty years of intensive research, the role of the magnetism in high T_c superconductivity is still under debate and the mechanism of high T_c superconductivity is still a big mystery.

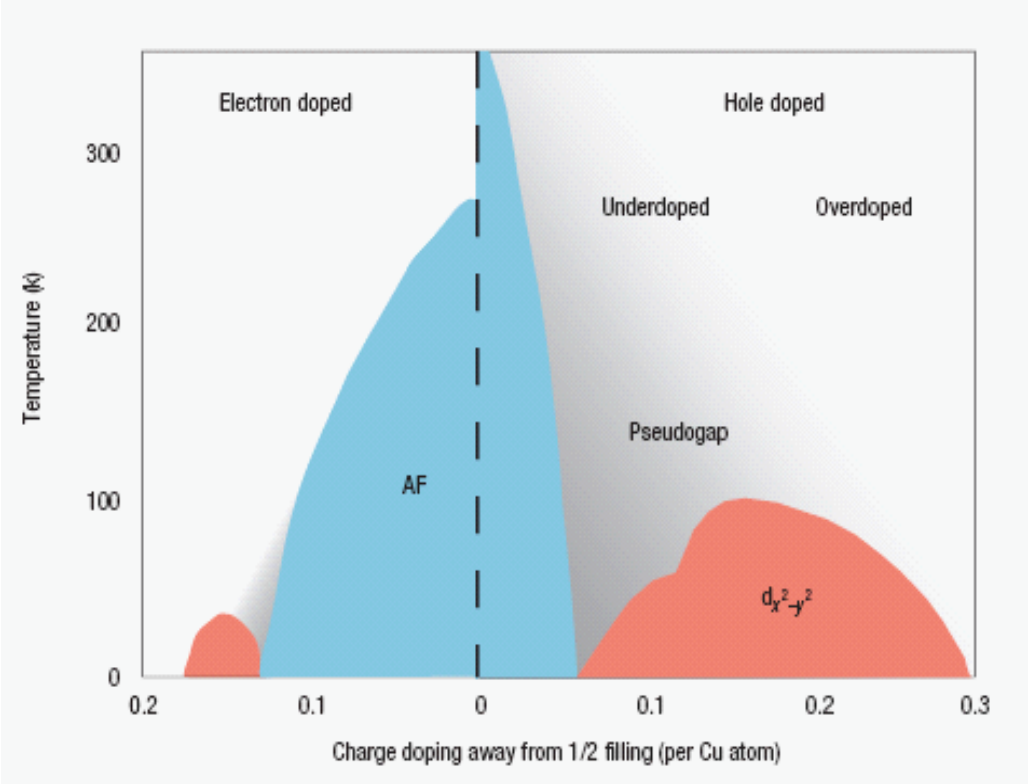

Figure 1.2: Phase diagram of cuprates as function of electron and hole dopings.

1.3 Fe based superconductors

For more than twenty years, high-temperature (high-T_c) superconductivity was believed to be unique in copper oxide based materials (cuprates). However, everything changed in the early part of 2008, when a class of high T_c superconductors based on iron (iron pnictides) was discovered [7]. Hosono et al. first observed 26 K superconductivity in Fe pnictide $LaFeAsO_{1-x}F_x$. Subsequent research discovered that replacing the lanthanum in $LaFeAsO_{1-x}F_x$ with other rare earth elements such as cerium, samarium, neodymium and praseodymium leads to superconducting transition temperature as high as 55 K [8–11]. The $RFeAsO_{1-x}F_x$ (R=rare earth) is usually referred as "1111" system. Several other subsets of the Fe based superconductors were also discovered, including "122","111" and "11" systems. All four systems have similar structures (Fig 1.3) and properties. "122″ ($A_{1-x}K_xFe_2As_2$, $AFe_{2-x}B_xAs_2$; A=Ca,Sr,Ba; B=Co,Ni,Rh) and "11″ ($FeSe_{1-x}Te_x$) systems have attracted a lot of interest due to their relative ease of growing single crystals. These discoveries greatly excited the scientific community, because electron phonon coupling in this system is also not strong enough to produce so high T_c just like that of cuprates [14]. Hence, Fe based superconductors are another class of high T_c superconductors which could help to understand the long standing issue, mechanism of high T_c superconductivity. Soon after the discovery of Fe based superconductors, scientists quickly realized that these two systems share a lot of common properties. First of all, they both have layered structure and have a CuO_2 or FeAs plane, where the superconductivity happens, suggested by band structure calculations (See Fig 1.1 and 1.3 for the typical structures of copper oxides and Fe pnictides). Secondly, both parent compounds of the copper oxides and Fe pnictides superconductors are antiferromagnets, although the latter is semimetal instead of insulator as in cuprates. The identical magnetic ground states of the parent compounds strongly indicate the antiferromagnetism plays key roles in both systems.

The parent compound of first discovered Fe based superconductor, known chemically as LaFeAsO, stacks iron and arsenic layers, where the electrons flow, between planes of lanthanum and oxygen, which is referred as charge reservoir. Superconductivity can be achieved by replacing the oxygen with fluorine, as electrons are induced in to the FeAs layers. Neutron scattering experiments showed that LaFeAsO undergoes an abrupt structural

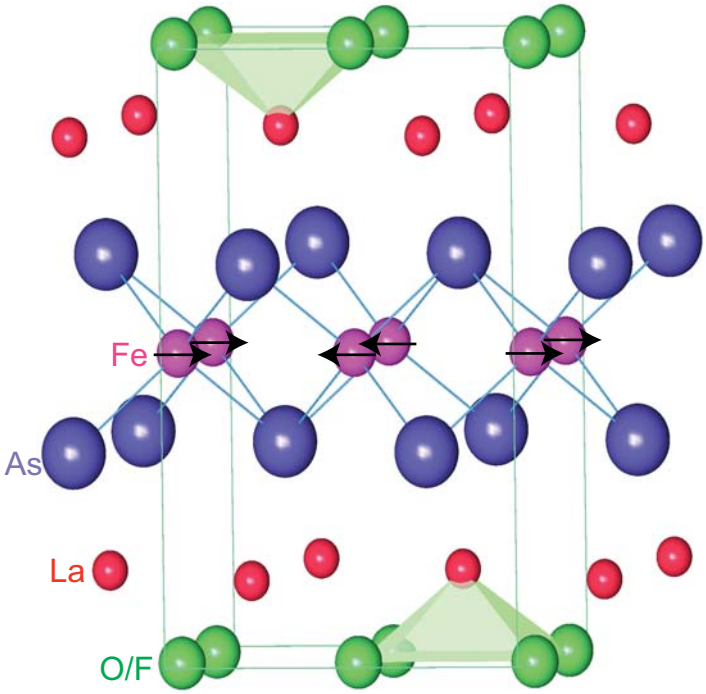

Figure 1.3: Magnetic and lattice structure of LaFeAsO/F.

distortion below 155 K, changing the symmetry from tetragonal (space group P4/nmm) to orthorhombic (space group Cmma) at low temperatures. In addition, the system develops long-range antiferromagnetic order with a colinear magnetic structure below 137 K as shown in Fig. 1.3 [12].

Although Fe pnictides and cuprates share a lot of common features, they do have some differences which are also important for testing theories for high T_c superconductivity. As depicted in Fig. 1.3, Fe is surrounded by a tetrahedron of As sites, which is in contrast to octahedral environment in cuptates. Different crystal field symmetries lead to very different diagram on 3d orbitals of transition metal ions (Cu^{2+} and Fe^{2+}). In the case of cuprate parent compound, Cu^{2+} only has one unpaired electron in $d_{x^2-y^2}$ resulting a static moment around 0.61 μ_B. For Fe^{2+} in Fe pnictides, there has to be at least two unpaired electrons which leads to a moment much larger than Cu^{2+} in cuprates. However, in LaFeAsO, the

measured moment is only about 0.36 μ_B which is much smaller than calculated value 2 μ_B in a simple local moment picture. Band structure calculations suggest that all five 3d orbitals contribute to the density of states near Femi surface in Fe pnictides, resulting a much more complicated band structure than cuprate which is a single band material. In addition, the electron correlations in the parent compounds of Fe pnictides are weaker than strongly correlated cuprates. As a consequence, the parent compound of Fe pnictide has a semimetal ground state instead of insulating one in cuprates. The striking small moment together with the metallic nature of the parent compound suggests the itinerant antiferromagnetism may be important to magnetic properties of Fe pnictides.

1.4 Introduction to neutron scattering

Neutron scattering is a powerful tool to study the nuclear and magnetic structure of condensed matter systems as well as lattice dynamics and spin excitations because neutrons have some unique advantages. A neutron has zero charge and no coulomb interaction with atoms in the solid, allowing the neutron to penetrate deeply into the materials for bulk properties study. Also, a neutron has 1/2 spin with a magnetic dipole moment 1.913 μ_n making it an ideal probe to detect magnetic moment, which X-ray can not do. Furthermore, the wavelength of the thermal neutrons is comparable to the interatomic distance. Thus interference effects occur, which provides information on structure of the scattering system. The energy of thermal neutrons is at the same order of the element excitations in the condensed matter systems, which means the inelastic neutron scattering measurements are very sensitive to the element excitations in the scattering system. The basic properties of neutrons are listed in Table 1 [16].

Table 1: basic properties of neutrons

Mass	M_n=1.675×$10^{-27}kg$
Magnetic moment	1.913 μ_n
Charge	0
Energy	
Cold neutron	0.1-10 meV
Thermal neutron	5-100 meV
Hot neutron	100-500 meV

In neutron scattering experiment, the sample will be put into the neutron beam and the scattered neutron intensity as a function of scattering angle and neutron energy will be detected. The geometry of the scattering experiment is shown in Fig. 1.4. The sample is usually a collection of atoms. The effective scattering area of each atom to an incident neutron can be expressed as cross-section. The partial differential cross section can be expressed as [15–17]

$d^2\sigma/d\Omega_f dE_f$ = (neutrons scattered sec^{-1} into $d\Omega$ in direction θ,ϕ with final energy between E and E+dE)/(Φ $d\Omega$)

here Φ is the flux of incident neutrons $area^{-1}time^{-1}$, E is the scattered neutron energy. The scattering process is ruled by the laws of momentum and energy conservation:

$$\vec{Q} = \vec{k}_f - \vec{k}_i \tag{1.2}$$

$$|\vec{Q}| = {k_f}^2 + {k_i}^2 - 2k_i k_f \cos\theta_s \tag{1.3}$$

$$\hbar\omega = E_i - E_f = \frac{\hbar^2}{2m_n}(k_f^2 - k_i^2) \tag{1.4}$$

In these equations, the wave vector magnitude $k = 2\pi/\lambda$, where λ is the neutron wavelength of the neutron beam, m_n is the mass of neutron, and the momentum transferred to the crystal is $\hbar\vec{Q}$. The subscripts i and f refer to the beam incident on the sample and diffracted beam. In the scattering process, a neutron acts as a very weak perturbation of the scattering system, so that the differential scattering cross section can be obtained from Fermi's Golden Rule [15–17].

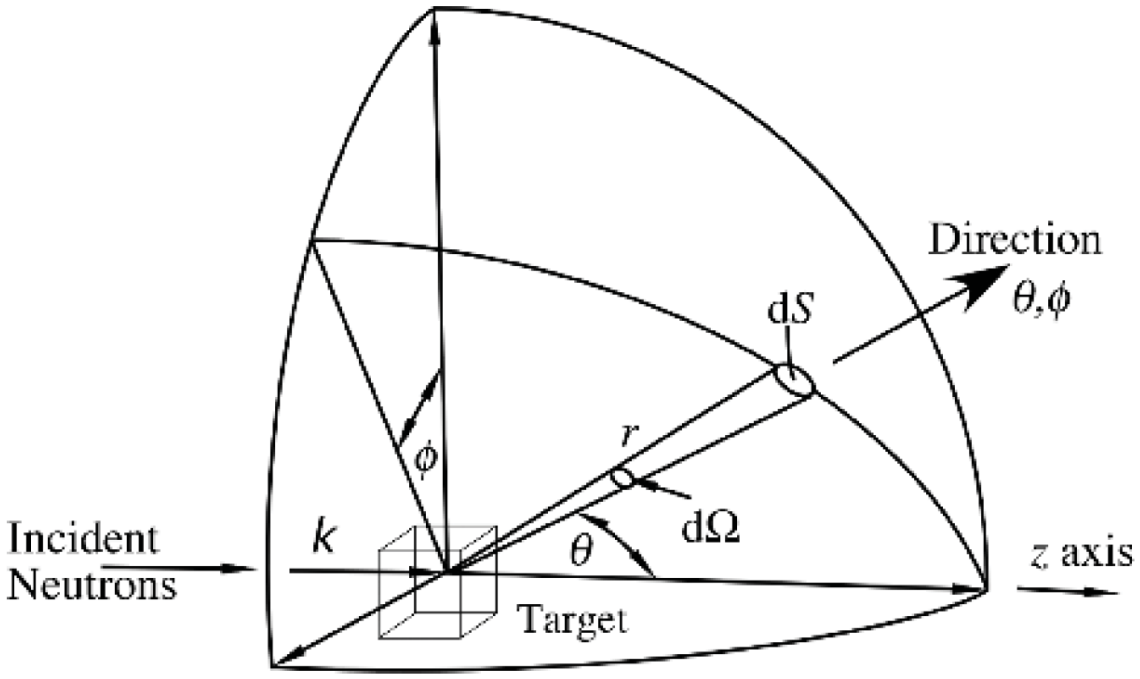

Figure 1.4: Geometry of neutron scattering experiment [16].

$$\frac{d^2\sigma}{d\Omega_f dE_f} = \frac{k_f}{k_i}(\frac{m_n}{2\pi\hbar^2})^2|\langle\vec{k}_f\lambda_f|V|\vec{k}_i\lambda_i\rangle|^2\delta(\hbar\omega + E_i - E_f) \tag{1.5}$$

where the λ_i and λ_f are quantum numbers for initial state and final state of the sample, respectively; V is the interaction operator for the neutron with sample. By using the Born approximation, we consider both the incident and outgoing neutrons as plane waves:

$$\langle\vec{k}_f\lambda_f|V|\vec{k}_i\lambda_i\rangle = V(\vec{Q})\langle\lambda_f|\sum_l e^{i\vec{Q}\cdot\vec{r}_i}|\lambda_i\rangle \tag{1.6}$$

where $\vec{r}_i$ are the coordinates of the scattering centers, and

$$V(\vec{Q}) = \int d\vec{r}V(\vec{r})e^{i\vec{Q}\cdot\vec{r}} \tag{1.7}$$

1.4.1 Nuclear cross section

For nuclear scattering, the neutron nuclear interaction force is short range ($\sim$ 1 fm), so the point particle approximation is valid and the nuclear potential is a delta function. Therefore the scattering can be considered as isotropic (s wave) which can be characterized by one parameter b (scattering length) [15–17], so

$$V(\vec{Q}) = \frac{m_n}{2\pi\hbar^2} b \tag{1.8}$$

Thus formula (1.5) can be written as

$$\frac{d^2\sigma}{d\Omega_f dE_f} = \frac{k_f}{k_i} \sum_{\lambda_i,\lambda_f} P(\lambda_i) |\langle \lambda_f | b \sum_l e^{i\vec{Q}\cdot\vec{r}} | \lambda_i \rangle|^2 \delta(\hbar\omega + E_i - E_f) \tag{1.9}$$

Where $P(\lambda_i)$ is the statistical weight factor for initial state $|\lambda_i\rangle$.

This can also be expressed as

$$\frac{d^2\sigma}{d\Omega_f dE_f} = N \frac{k_f}{k_i} S(\vec{Q}, \omega) \tag{1.10}$$

where the scattering function $S(\vec{Q}, \omega)$ is

$$S(\vec{Q}, \omega) = \frac{1}{2\pi\hbar N} \sum_{l,l'} \int_{-\infty}^{+\infty} dt < e^{-i\vec{Q}\cdot\vec{r_l'}(0)} e^{-i\vec{Q}\cdot\vec{r_l'}(t)} > e^{-i\omega t} \tag{1.11}$$

where N is the number of nuclei, t is time. The experiments of neutron scattering are essentially measuring $S(\vec{Q}, \omega)$. In the case of magnetic scattering, based on the fluctuation-dissipation theorem, the imaginary part of the dynamic susceptibility can be calculated as

$$\chi''(\vec{Q}, \omega) = S(\vec{Q}, \omega)(1 - e^{-\frac{\hbar\omega}{k_B T}}) \tag{1.12}$$

In the case of elastic nuclear scattering ($\hbar\omega = 0$),the coherent scattering cross section is

$$\frac{d\sigma}{d\Omega} = N \frac{(2\pi)^2}{v_0} \sum_{\vec{G}} \delta(\vec{Q} - \vec{G}) |F_N(\vec{G})|^2 \tag{1.13}$$

where the structure factor is

$$F_N(\vec{G}) = \sum_j \bar{b}_j e^{i\vec{G}\cdot\vec{r_j}} e^{-W_j} \tag{1.14}$$

where v_0 is the volume of the unit cell and e^{-W_j} is the Debye-Waller factor.

In the case of inelastic nuclear scattering, $S(\vec{Q},\omega)$ usually corresponds to the excitations of the phonon scattering [15–17]. The cross section for single phonon creation is

$$\frac{d^2\sigma}{d\Omega_f dE_f} = \frac{k_f}{k_i}\frac{(2\pi)^3}{2v_0}\sum_{G,q}\delta(\vec{Q}-\vec{q}-\vec{G})\sum_s \frac{1}{\omega_{qs}}[n_s(\omega)+1]\delta(\omega-\omega_{qs})|F(\vec{Q})|^2 \tag{1.15}$$

where the dynamic structure factor

$$F(\vec{Q}) = \sum_j \frac{\bar{b_j}}{\sqrt{m_j}}(\vec{Q}\cdot\vec{\xi_{js}})e^{i\vec{Q}\cdot\vec{d_j}}e^{-W_j} \tag{1.16}$$

for a phonon mode s, the polarization vector for the jth atom in the unit cell is $\vec{\xi_{js}}$. m_j is the mass of the jth atom, $n_s(\omega)$ is the Bose-Einstein distribution.

1.4.2 Magnetic cross section

The neutron has a dipole moment, which can interact with the magnetic moment in the atom via the dipole-dipole interaction. For an unpaired electron with magnetic moment, μ_e and momentum, p, the magnetic field felt by the neutron is [15–17]

$$B = \frac{\mu_0}{4\pi}[\nabla\times(\frac{\mu_e\times\hat{R}}{R^2} - \frac{2\mu_B}{\hbar}\frac{p\times\hat{R}}{R^2}] \tag{1.17}$$

The magnetic cross section depends on not only the wave vector transfer but also the initial spin states s_i and final spin states s_f of the neutron.If we only consider the magnetic interaction in Eq. 1.5 the cross section can be rewritten as

$$\frac{d^2\sigma}{d\Omega_f dE_f} = \frac{k_f}{k_i}(\frac{m_n}{2\pi\hbar^2})^2|\langle\alpha_f\lambda_f|V_m|\alpha_i\lambda_i\rangle|^2\delta(\hbar\omega+E_i-E_f) \tag{1.18}$$

where $\vec{V_m} = -\vec{\mu_n} \cdot \vec{B}$ is the potential of the magnetic field, and α_i,λ_i and α_f,λ_f refer the initial and final states of the neutron (α) and electron (β), respectively. For simplicity, if we only consider the atomic moment is due purely to spin. we have

$$\frac{d^2\sigma}{d\Omega_f dE_f} = \frac{k_f}{k_i} \sum_{i,f} P(\lambda_i) |\langle \lambda_f | \sum_l e^{i\vec{Q}\cdot\vec{r_l}} U_l^{S_i S_f} |\lambda_i\rangle|^2 \delta(\hbar\omega + E_i - E_f) \tag{1.19}$$

$U_l^{S_i S_f}$ is the atomic scattering amplitude from the spin state s_i to s_f

If the system only contains a single species of magnetic atom, the cross section can be written

$$\frac{d^2\sigma}{d\Omega_f dE_f} = \frac{\gamma r_0 N}{4\pi\hbar} \frac{k_f}{k_i} g f(\vec{Q})^2 e^{-2W} \sum_{\alpha,\beta} (\delta_{\alpha,\beta} - \hat{Q}_\alpha \hat{Q}_\beta) \int_{-\infty}^{+\infty} dt e^{-i\omega t} \sum_l e^{i\vec{Q}\cdot\vec{r_l}} \langle S_0^\alpha(0) S_l^\beta(t) \rangle \tag{1.20}$$

where α, β represent x,y,z. the term $\delta_{\alpha,\beta} - \hat{Q}_\alpha \hat{Q}_\beta$ means only the moment perpendicular $\vec{Q}$ contributes to the magnetic cross section. $f(\vec{Q})$ is the magnetic form factor which is the Fourier transform of the unpaired electron density. In the case of elastic scattering

$$\frac{d\sigma}{d\Omega_f} = \frac{\gamma r_0 N}{4\pi\hbar} \frac{k_f}{k_i} g f(\vec{Q})^2 e^{-2W} \sum_{\alpha,\beta} (\delta_{\alpha,\beta} - \hat{Q}_\alpha \hat{Q}_\beta) \sum_l e^{i\vec{Q}\cdot\vec{r_l}} \langle S^\alpha(0) S^\beta(l) \rangle \tag{1.21}$$

1.5 Neutron scattering instruments

Neutron scattering experiments can be done on a lot of instruments such as the triple axis spectrometer, powder diffractometer, time of flight backscattering or chopper spectrometer, among which the triple axis and time of flight chopper spectrometers are intensively used in my thesis work. The triple axis is a very powerful instrument for the elastic and inelastic neutron scattering measurements. The schematic of the triple axis is shown in Fig. 1.5.

The triple axis spectrometers are located at the reactor based neutron source in which neutrons arise from the spontaneous fission of U^{235}, and the neutrons are produced continuously in time. The three axis correspond to the monochromator axis, the sample axis and the analyzer axis. The monochromator is a single crystal which defines the incident neutron energy and momentum basing on the Bragg's law. The monochromator can be crystals of graphite, silicon and copper, or in the case of polarized neutrons, a Heusler alloy.

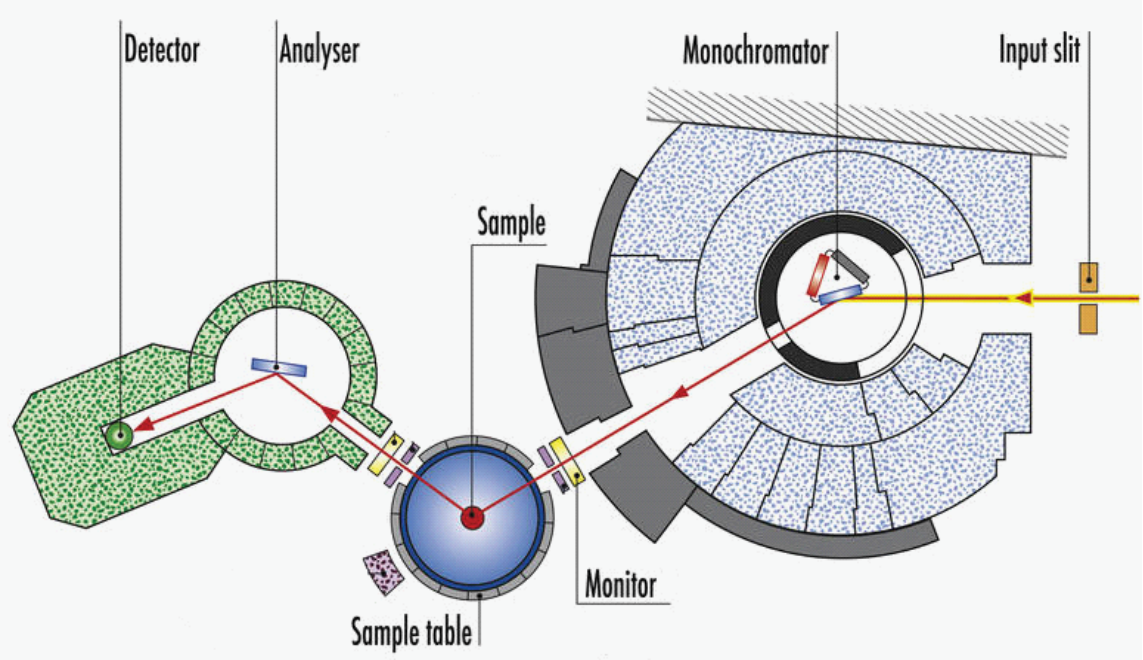

Figure 1.5: Schematic of IN22 triple axis spectrometer. Triple axis corresponds to the monochrometer, sample and analyzer axis, respectively. Bragg's reflections from the monochrometer and analyzer single crystals define the incident and final energies for the experiment.

The analyzer crystal defines the scattered neutron energy and momentum. In an elastic scattering process, a neutron is deflected but loses or gains no energy. In an inelastic event, a neutron loses or gains energy during the interaction. Based on the momentum conservation and energy conservation laws, we can measure the dispersion of the excitations in the sample [16].

Another popular neutron scattering instrument is time of flight chopper spectrometer. In this instrument neutrons are produced by a spallation neutron source, where neutrons are produced by bombarding a heavy metal target with high energy protons [15, 16]. In this source the neutrons come as pulses white beam. The setup of MAPS Time of Flight Chopper Spectrometer is shown in Fig. 1.6. A single incoming energy can be selected by measuring the times taken by neutron to travel from the source to the Fermi chopper. The neutrons arrive at the sample in monochromatic pulses of known energy. After scattering from the sample they are detected in fixed arrays of detectors as a function of their total time of flight. With the knowledge of the sample detector distances and the incident beam

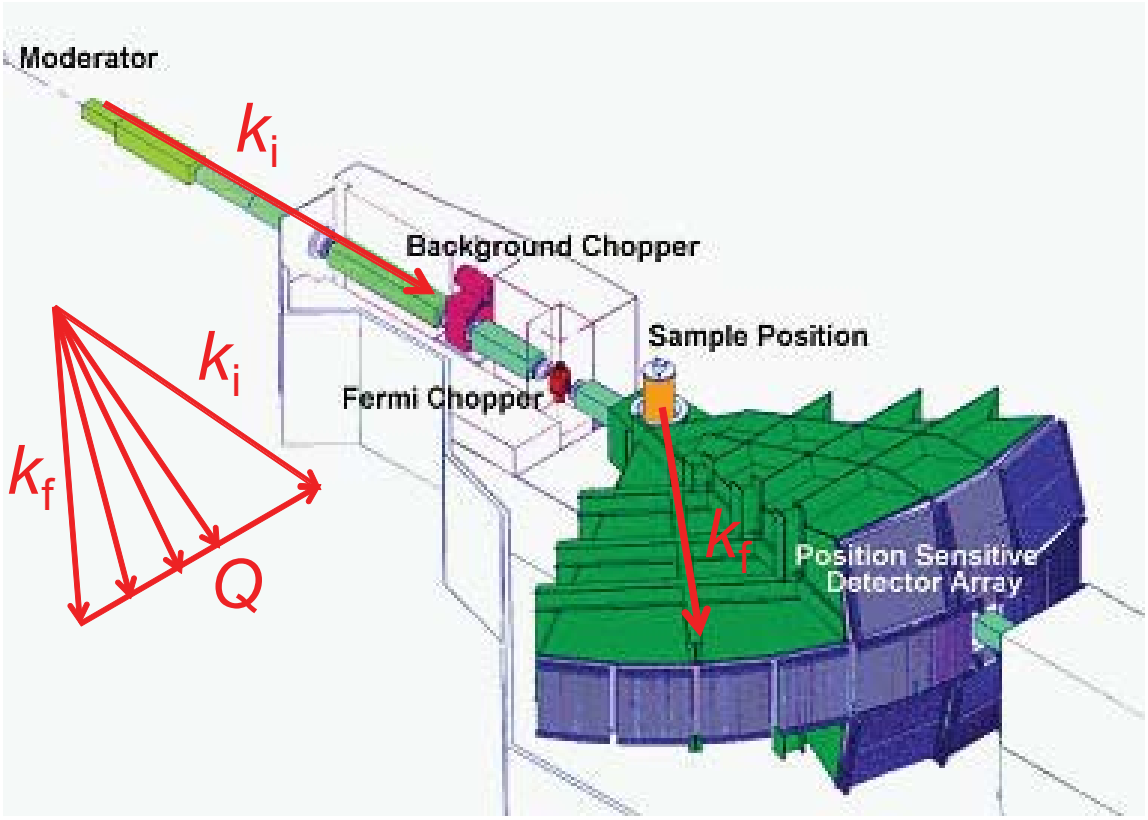

Figure 1.6: Schematic of MAPS time of flight chopper spectrometer. The inset shows the picture of the scattering triangle law. Fermi-chopper selects a incident beam energy based on the known distance and pulse time of the neutron source. The position-sensitive detectors can probe multiple momentum and energies simultaneously.

energy, the final energy can be calculated. For all energies the final wave vector will lie along the same direction, however the magnitude will decrease with the velocity of the incident energy neutrons. The scattering triangle is thus altered in time as shown in Fig. 1.6.

1.6 Neutron scattering measurements in high T_c superconductors

As we mentioned in Chapter 1.2, high T_c superconductivity always arises in the proximity of antiferromagnetism. Since its discovery, the neutron scattering has contribute tremendously in understanding the magnetic properties of the high T_c superconductors. Shortly

after the initial discovery of superconductivity in $La_{2-x}Ba_xCuO_4$, Vaknin et al. discovered that the parent compound La_2CuO_4 was antiferromagnet using neutron scattering powder diffraction technique [13]. The magnetic moment of Cu^{2+} is about 0.5 μ_B which is much smaller than the calculated value 1 μ_B for a $S = 1/2$ system. There are several effects can be taken in to account to explain this inconsistency: (i)variations due to excess oxygen in the system [18]; (ii) covalency effects due to hybridisation of the copper and oxygen atoms in the planes [19,20]; (iii)strong quantum fluctuations in a quasi-2D antiferromagnet. The undoped parent compound the of cuprate is quasi-2D antiferromagnets, the magnetic excitations of which can be described by a two-dimensional quantum Heisenberg antiferromagnet. The Heisenberg Hamiltonian in the CuO_2 plane of the system can be written as

$$H = J_{nn} \sum_{i,j} S_i \cdot S_j + J_{nnn} \sum_{i,k} S_i \cdot S_k \tag{1.22}$$

The nearest neighbor exchange coupling is antiferromagnetic ($\sim 100meV$) for La_2CuO_4 [22], the next nearest neighbor exchange coupling is ($\sim -18meV$), which is ferromagnetic coupled. The exchange couplings are usually determined by bonding angles and bonding distances in Heisenberg model. So the c axis coupling J_c is several order smaller than the J_{nn}. Large in plane exchange coupling in the parent compound indicate high energy scale of the spin dynamics of Cu^{2+}, which is the prerequisite if the antiferromagneitism is the driving force for the high T_c superconductivity. Neutron scattering experiment performed by Hayden et al [21,22] shows that the spin excitation spectrum extends up to around 300 meV and the spectral weight is almost independent of energy below 200 meV, which is consistent with a quasi 2D Heisenberg antiferromagnet (Fig. 1.7).

The magnetic excitations were also studied intensively as the system is tuned into superconducting regime in cuprates for the past twenty years. As we mentioned earlier, although the static magnetic order is suppressed with doping, the magnetic fluctuations persist in the superconducting sample. In the case of YBCO, inelastic neutron scattering experiment showed that spin excitation spectral weight has been brought down to much lower energy in contrast with the parent compound where most of the spectral weight piles up near the zone boundary at $\sim$ 300 meV. As the system is tuned toward optimal doping, the magnetic response is dominated by a resonance peak, which is a strong

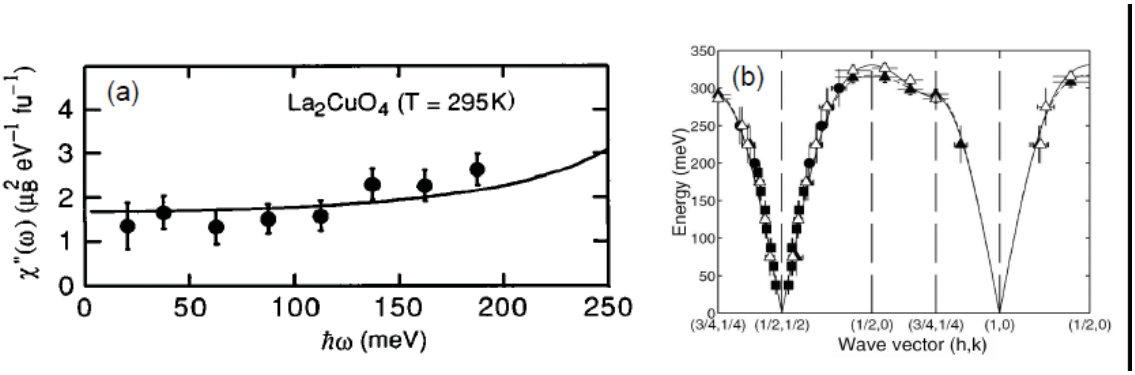

Figure 1.7: a) Energy dependence of local sucestibiltiy in La_2CuO_4 [21] b) Spin wave dispersions in La_2CuO_4 [22].

and sharp commensurate feature in the superconducting state near the antiferromagnetic zone center at energies $E_{res} = 5.8k_BT_c$, where k_B and T_c are Boltzman constant and superconducting transition temperature, respectively. The resonance peak is rapidly suppressed as warming and displays an superconducting order parameter like temperature dependence, which makes the resonance peak weak or even invisible in normal state. The resonance mode was first discovered in YBCO by Rossat-Mignod et al [23]. Subsequent research revealed that resonance is actually a general feature as they were also observed in other hole doped cuprates $Bi_2Sr_2CaCu_2O_{8-\delta}$ and $Tl_2Ba_2CuO_6$ [24–26], as well as electron doped cuprate $Pr_{0.88}LaCe_{0.12}CuO_4$ [27]. The incommensurate magnetic response intensity enhancement below T_c was also observed in $La_{2-x}Sr_xCuO_4$, which is termed as "incommensurate resonance" or "coherence peak". The resonance modes were also discovered in several Fe based superconductors such as $Ba_{1-x}K_xFe_2As_2$, $BaFe_{2-x}A_xAs_2$ (A=Co,Ni)and $FeSe_{1-x}Te_x$ shortly after the discovery of this new class of high T_c superconductors. The magnetic excitations are suppressed in the superconducting state at energies below the resonance mode, suggesting the opening of a superconducting spin gap. Detailed analysis of the magnetic response spectral weight reveal that spectral weight (or part of) loose in the spin gap is compensated by the intensity gain of the resonance mode in the superconducting state. The universality of resonance mode and its relationship with T_c strongly indicate it is critical to the mechanism of high T_c superconductivity.

Although the energy dependence of the magnetic response shares common features (resonance and spin gap) within different classes of high T_c superconductors, the momen-

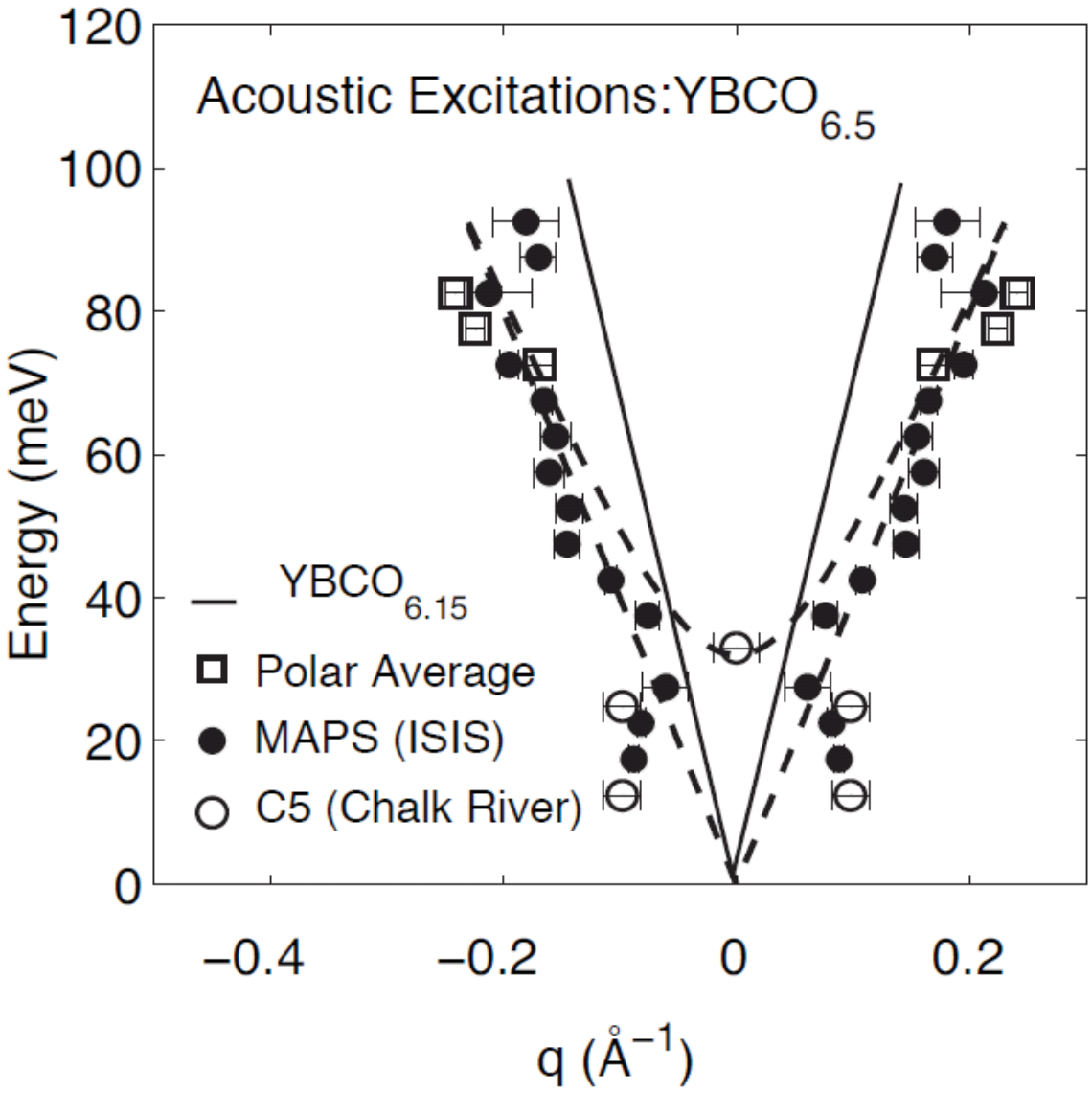

Figure 1.8: Momentum dependence of spin excitations in $YBCO_{6.5}$ shows an hour glass like dispersion. The saddle point is at around 38 meV. The magnetic excitations are incommensurate below and above the saddle point (resonance) [28, 29]

.

tum dependence of the magnetic response is somehow distinct from one to another. In hole doped cuprates YBCO, the magnetic excitations displays hourglass like dispersion (Fig. 1.8) [28, 29]. The commensurate resonance mode, which carries most of the magnetic response spectral weight, is located right at the saddle point. the magnetic response is incommensurate below and above the resonance energy. Although the hour glass like dispersion is also observed in another hole doped cuprate $La_{2-x}Sr_xCuO_4$, the saddle point ($\sim$ 50 meV) exhibits little temperature dependence across T_c. In stead, an incommensurate resonance like excitation is observed at lower energy, which has similar temperature dependence as resonance mode as in the other cuprates. In the case of electron doped cuprates, the magnetic excitations are all commensurate below and above the resonance mode.

The spin excitations in hole doped cuprates were studied very intensively by neutron scattering for the past twenty years. However the experimental effort studying the magnetism in the hole-doped cuprates has no parallel in the electron-doped systems and the newly discovered Fe based superconductors. Electron doped cuprates differs with hole doped cuprates in many different aspects, such as the much lower up critical field, lack of pseudo gap state and commensurate spin excitations. Even more is unknown in the magnetism in Fe based superconductors. Comparing the antiferromagnetism in electron doped cuprates and Fe based superconductors together with the hole doped cuprates will definitely shed some light on understanding the interplay between the antiferromagnetism and high T_c superconductivity.

Chapter 2

Low Energy Spin Excitations in Optimally Electron-Doped Superconductor $Nd_{1.85}Ce_{0.15}CuO_{4-\delta}$

2.1 Introduction and motivation

In conventional Bardeen-Cooper-Schrieffer (BCS) superconductors, the superconducting phase forms when electrons are bound into pairs with long-range phase coherence through interactions mediated by lattice vibrations (phonons) [3]. Since high-transition-temperature (high-T_c) superconductivity arises in copper oxides when sufficient holes or electrons are doped into the CuO_2 planes of their insulating antiferromagnetic (AFM) parent compounds [30], it is important to determine if spin fluctuations play a fundamental role in the mechanism of high-T_c superconductivity [31]. For hole-doped superconductors, it is now well documented that the spin fluctuations spectrum forms an 'hourglass' dispersion with the most prominent feature, a collective excitation known as the resonance mode, centered at the AFM ordering wavevector $\mathbf{Q} = (1/2, 1/2)$ [23, 24, 29, 32–39]. Although the energy of the mode tracks T_c and its intensity behaves like an order parameter below T_c for materials such as $YBa_2Cu_3O_{6+x}$ (YBCO) [23, 29, 32–34], the intensity of the saddle point where the

low energy incommensurate spin fluctuations merge into the commensurate $\mathbf{Q} = (1/2, 1/2)$ point in $La_{2-x}(Sr,Ba)_xCuO_4$ (LSCO) displays negligible changes across T_c [38–40]. Instead, the effect of superconductivity in optimally hole-doped LSCO is to open a spin gap [35] and pile density of states along incommensurate wavevectors at energies above the spin gap [36, 38, 39], and thus appears to be different from YBCO.

If the resonance is fundamental to the mechanism of superconductivity, it should be ubiquitous to all high-T_c superconductors. Although the superconductivity-induced enhancement at incommensurate wavevectors in LSCO has been argued to be comparable to the commensurate resonance in YBCO [40], the intensity gain of the resonance below T_c may not always be compensated by opening of a spin gap and spectral weight loss at lower energies. For example, the resonance intensity gain in the electron-doped $Pr_{0.88}LaCe_{0.12}CuO_4$ (PLCCO, $T_c = 24$ K) below T_c is not compensated by spectral weight loss at lower energies [27]. On the other hand, while neutron scattering measurements found a low-temperature spin gap (about 4 meV) in the electron-doped superconductor $Nd_{1.85}Ce_{0.15}CuO_4$ (NCCO) [41, 42], there have been no report of the resonance or spectral weight gain at energies above the spin gap below T_c. Therefore, the relationship between the superconducting spin gap and the resonance is still an open question. In this chapter, we studied the temperature dependence of the spin fluctuations in an optimally electron-doped NCCO ($T_c = 25$ K). We confirm the presence of a low-temperature spin (pseudo) gap [42] and show that the effect of superconductivity also induces a resonance at energies similar to electron-doped PLCCO [27]. Our results thus demonstrate that the resonance is an ubiquitous feature of optimally electron-doped superconductors. Its intensity gain below T_c in NCCO is due in part to the opening of a spin pseudo gap and spectral weight loss at low energies. This is remarkably similar to the optimally hole-doped LSCO [38, 39], and thus suggesting that the enhancement at incommensurate wavevectors below T_c in LSCO has the same microscopic origin as the commensurate resonance in other high-T_c superconductors.

2.2 Experimental details

We grew a high quality (mosaicity $< 1^\circ$, 3.5 grams) NCCO single crystal using a mirror image furnace [43]. Fig. 2.1a plots the magnetic susceptibility measurements showing an onset T_c of 25 K with a transition width of 3 K. Our neutron scattering experiments were performed on the IN-8 thermal triple-axis spectrometer at the Institute Laue Langevin, Grenoble, France. We define the wave vector $\mathbf{Q}$ at (q_x, q_y, q_z) as $(h, k, l) = (q_x a/2\pi, q_y a/2\pi, q_z c/2\pi)$ reciprocal lattice units (r.l.u) in the tetragonal unit cell of NCCO (space group $I4/mmm$, $a = 3.95$, and $c = 12.07$ Å). For the experiment, the NCCO sample is mounted in the $[h, k, 0]$ zone inside a cryostat. We chose a focusing Si(111) as monochromator and PG(002) as analyzer without collimation. The final neutron energy was fixed at $E_f = 14.7$ meV with a pyrolytic graphite (PG) filter in front of the analyzer. This setup resulted an energy resolution of about 1 meV in full-width-half-maximum (FWHM) at $\mathbf{Q} = (-0.5, 0.5, 0)$.

2.3 Low energy spin gap and resonance mode

To understand the effect of superconductivity on the Cu^{2+} spin fluctuations, we must first determine the temperature dependence of the magnetic excitations from Nd^{3+} crystal electric field (CEF) levels in NCCO. For Nd ions in the tetragonal NCCO crystal structure, the three lowest energy CEF magnetic excitations are at $\hbar\omega = 12.2 \pm 0.3$ meV, 20.3 ± 0.1 meV, and 26.5 ± 0.3 meV [68]. Our energy scans at $\mathbf{Q} = (-0.5, 1.5, 0)$ confirm these results and show that the intensities of these CEF levels have small temperature dependence between 2 K and 30 K (Fig. 2.1c).

Fig. 2.2 summarizes the transverse and longitudinal $\mathbf{Q}$-scans around $(-0.5, 0.5, 0)$ at different energy transfers and temperatures. Consistent with earlier results on NCCO [42] and PLCCO [27,45], the scattering is commensurate and centered at $\mathbf{Q} = (-0.5, 0.5, 0)$ for all energies probed. Fig. 2.2a-d show the raw data (with scan directions marked) below and above T_c at $\hbar\omega = 2.5$, 8 meV. At $T = 30$ K ($T_c + 5$ K), the magnetic scattering above the linear backgrounds decreases slightly with increasing energy from 2.5 meV to 8 meV (Figs. 2.2e and 2.2f). On cooling to below T_c, the peak intensity is drastically

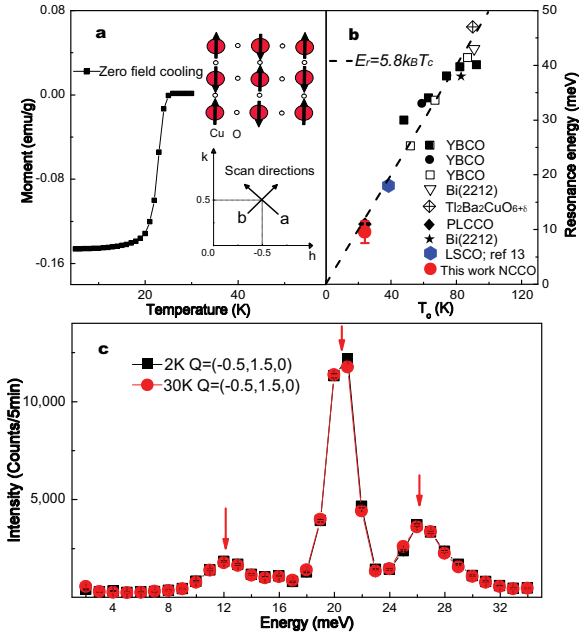

Figure 2.1: a) Schematic diagrams of real and reciprocal space of the CuO_2 with the transverse and longitudinal scans marked as **a** and **b**, respectively. Magnetic susceptibility measurements of T_c. b) Summary of the resonance energy as a function of T_c for various hole- and electron-doped superconductors from [27] with NCCO (this work) and LSCO [38] added. c) Energy scans at $\mathbf{Q} = (-0.5, 1.5, 0)$ at 2 K and 30 K. The three CEF levels are marked by arrows [68].

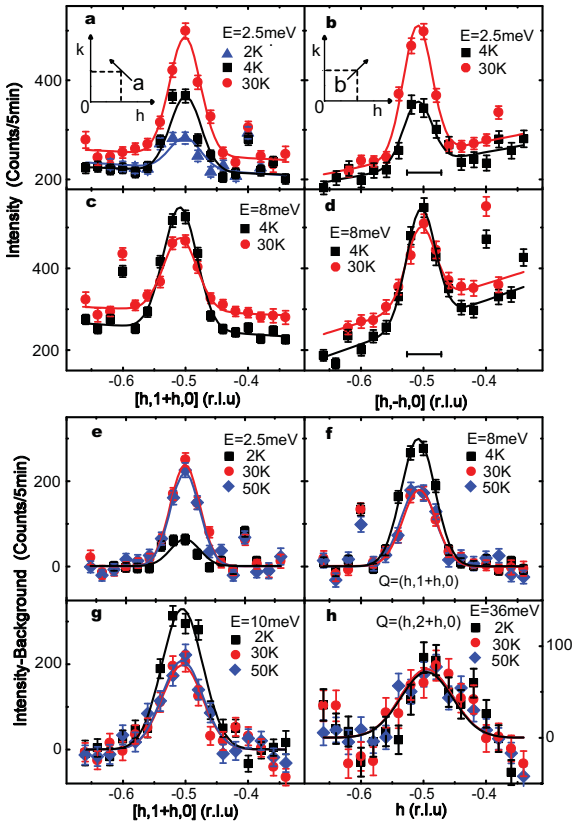

Figure 2.2: Transverse and radial scans through $\mathbf{Q} = (-0.5, 0.5, 0)$ for a,b) $\hbar\omega = 2.5$ meV, and c,d) 8 meV at various temperatures. Radial scans in b,d) are instrumental resolution limited (horizontal bars) that gives a minimum dynamic spin correlation length $\xi \approx 46$ Å at 2.5 meV. Transverse scans around $\mathbf{Q} = (-0.5, 0.5, 0)$ with linear background subtracted for e) $\hbar\omega = 2.5$ meV, f) 8 meV, and g) 10 meV at temperature above and below T_c. h) The transverse scan around $\mathbf{Q} = (-0.5, 1.5, 0)$ at $\hbar\omega = 36$ meV has negligible temperature dependence across T_c.

suppressed for $\hbar\omega = 2.5$ meV (Figs. 2.2a and 2.2b), and it increases for $\hbar\omega = 8$ meV (Figs. 2.2c and 2.2d). Figs. 2.2e-g show background subtracted transverse scans at various energies. It is immediately clear that cooling below T_c suppresses the $\mathbf{Q} = (-0.5, 0.5, 0)$ peak at $\hbar\omega = 2.5$ meV but enhances scattering at $\hbar\omega = 8$ and 10 meV. On the other hand, magnetic scattering at $\hbar\omega = 36$ meV changes negligibly from 2 K to 50 K (Fig. 2.2h). Figs. 2.3a and 2.3b show energy scans at the signal [$\mathbf{Q} = (-0.5, 0.5, 0)$] and background [$\mathbf{Q} = (-0.34, 0.66, 0)$] positions above and below T_c. Although the large Nd^{3+} CEF level dominated the magnetic scattering at $\hbar\omega = 12$ meV [68], one can still see clear Cu^{2+} spin fluctuations centered at $(-0.5, 0.5, 0)$ for energies between 2 and 10 meV. In the normal state, the magnetic scattering decreases with increasing energy, consistent with $\mathbf{Q}$-scans at $\hbar\omega = 2.5$, 8, and 10 meV (Figs. 2.2e-g). In the superconducting state, the low-energy spin fluctuations at $\mathbf{Q} = (-0.5, 0.5, 0)$ are suppressed for $\hbar\omega \leq 4$ meV and there is a clear scattering intensity gain for $6 \leq \hbar\omega \leq 10$ meV. The contrast between the normal and superconducting states becomes more obvious when changes in background scattering are taken into account (Fig. 2.3b). The large Nd^{3+} CEF scattering between $10 < \hbar\omega < 33$ meV (Fig. 2.1c) overwhelmed Cu^{2+} magnetism. The background corrected difference plot between the superconducting and normal states shows a resonance at $\hbar\omega = 9.5 \pm 2$ meV, similar to that for PLCCO [27].

To determine if the low temperature spin fluctuations' suppression below 4 meV and enhancement between 6 to 10 meV are indeed associated with the opening of a superconducting gap below T_c as in the tunneling experiments [46], we carefully measured the temperature dependent scattering at the peak [$\mathbf{Q} = (-0.5, 0.5, 0)$] and background [$\mathbf{Q} = (-0.6, 0.4, 0)$] positions for $\hbar\omega = 2.5$ and 8 meV. From previous low-energy inelastic neutron scattering work on NCCO [42], we know that the spin gap in NCCO opens gradually with decreasing temperature until it reaches to about 4 meV at 2 K. While peak intensity in the $\mathbf{Q}$-scans at $\hbar\omega = 2.5$ meV show a clear low temperature suppression, there is still a peak present at $\mathbf{Q} = (-0.5, 0.5, 0)$ even at 2 K. Therefore, optimally electron-doped NCCO does not have a clean spin gap as in the case of the optimally hole-doped LSCO [35]. The temperature dependence of the scattering at the peak and background positions (Figs. 2.4a and 2.4b) reveals that the intensity suppression at $\hbar\omega = 2.5$ meV does not happen at T_c but at 9 K ($T_c - 16$ K). While this result confirms the earlier report [42],

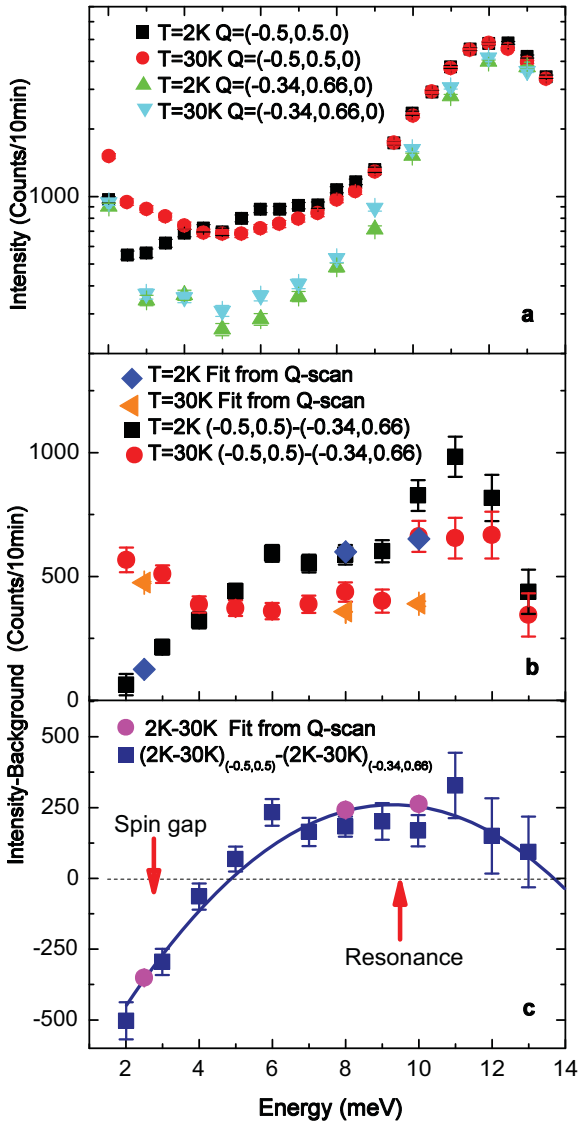

Figure 2.3: a) The temperature dependence of the scattering at the peak [$\mathbf{Q} = (-0.5, 0.5, 0)$] and background [$\mathbf{Q} = (-0.34, 0.66, 0)$] positions below and above T_c. Note the intensity is plotted in log-scale to display the large intensity difference between the Nd^{3+} CEF level at $\hbar\omega = 12$ meV and Cu^{2+} spin fluctuations centered at $\mathbf{Q} = (-0.5, 0.5, 0)$ for energies between 2 and 10 meV. b) Background subtracted magnetic scattering at $\mathbf{Q} = (-0.5, 0.5, 0)$ below and above T_c. The data are cross checked by constant-energy scans in Fig. 2.2. c) The temperature difference plot showing the resonance at $E_r = 9.5 \pm 2$ meV. The large error is due to the uncertainty in obtaining Cu^{2+} magnetic signal above 10 meV.

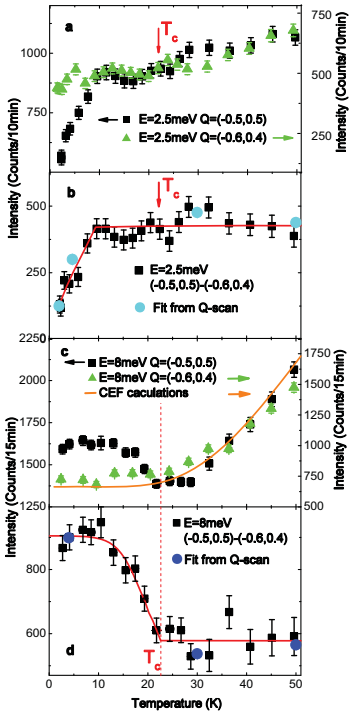

Figure 2.4: Temperature dependence of the scattering at $\hbar\omega = 2.5$, and 8 meV. a) The raw data at the signal [$\mathbf{Q} = (-0.5, 0.5, 0)$] and background [$\mathbf{Q} = (-0.6, 0.4, 0)$] positions. b) The background subtracted magnetic scattering at $\hbar\omega = 2.5$ meV shows no anomaly cross T_c but drops dramatically below 9 K. The data from the fitted $\mathbf{Q}$-scans are shown as circles. c) Temperature dependent data for $\hbar\omega = 8$ meV, a resonance coupled to T_c like an order parameter is clearly seen in the background subtracted data in d). The estimated temperature dependence of the Nd^{3+} CEF level at 8 meV (from 12 meV to 20 meV) is shown as solid line in c) [68].

it also suggests that the gradual opening of the (pseudo) spin gap is not directly related the temperature dependence of the superconducting gap which is BCS-like [46] and becomes essentially fully opened with $2\Delta \approx 7$ meV below 12 K (50% of T_c).

On the other hand, the temperature dependence of the scattering at $\hbar\omega = 8$ meV is clearly coupled to the occurrence of superconductivity. With increasing temperature, the scattering at $\mathbf{Q} = (-0.5, 0.5, 0)$ first decreases like an order parameter, showing a kink at T_c, and then increases again above 30 K. It turns out that the large intensity rise above 30 K at $\hbar\omega = 8$ meV is due to the CEF transition from 12 meV to 20 meV as the 12 meV state is being populated with increasing temperature (Fig. 2.4c) [68]. As the CEF levels are weakly $\mathbf{Q}$-dependent, the large intensity increase above 30 K is also seen in the background (Fig. 2.4c). The difference between signal and background

shows a clear order-parameter-like temperature dependence of the resonance, remarkably similar to the temperature dependence of the resonance in PLCCO [27] and hole-doped superconductors [23, 24, 29, 32–34].

2.4 Discussion and conclusions

The discovery of the resonance in another class of electron-doped superconductors suggests that the mode is a general phenomenon of electron-doped superconductors independent of their differences in rare-earth substitutions [41]. For hole-doped LSCO [35–39], the intensity enhancement in spin susceptibility above the spin-gap energy has been characterized as the magnetic coherence effect [36, 40]. The observation of the susceptibility enhancement at energies ($6 \leq \hbar\omega \leq 13$ meV) just above the spin pseudo gap energy of 4 meV in NCCO is consistent with this picture, although the temperature dependence of the spin pseudo gap in NCCO behaves rather differently from those in LSCO [35, 42]. In our search for the excitations responsible for electron pairing and high-T_c superconductivity, one of the arguments against the relevance of the resonance has been the inability to observe superconductivity-induced commensurate resonance in LSCO [35, 36, 38, 39]. If the resonance is a phenomenon associated with the opening of a superconducting gap and the subsequent local susceptibility enhancement, it is natural to regard the susceptibility gain in both NCCO and LSCO as the resonance. Adding these two points to the universal $E_r = 5.8k_BT_c$ plot in Fig. 2.1b suggests that while the resonance energy itself is intimately related to T_c, other details such as the spin gap, commensurability, and hourglass dispersion found in different materials may not be fundamental to the superconductivity.

For hole-doped superconductors, the hourglass dispersion has been interpreted either as the signature of "stripes" where doped holes are phase separated from the Mott-like AF background [47–49], or as a bound state (spin exciton) within the gap formed in the non-interacting particle-hole continuum of a Fermi-liquid [50, 51]. Although the resonance in PLCCO has been interpreted as an over damped spin exciton [52], it remains a challenge to understand how the resonance can arise both from NCCO which has a spin pseudo gap and from the gapless PLCCO [53].

Chapter 3

Polarized and Unpolarized Neutron Scattering Measurements of Spin Fluctuations of Optimally Doped $\mathbf{Pr_{0.88}LaCe_{0.12}CuO_{4-\delta}}(T_c = 24\ \mathbf{K})$

3.1 Introduction and motivation

In Chapter 2, we demonstrated the resonance is also a universal feature for electron doped cuprates, thus must be relevant to the high T_c superconductivity in cuprates. However, to identify if the resonance is the driving force, or only the consequence of the high T_c superconductivity, it is important to study the electron (charge) resonance(spin excitations) couplings and their consequence to high T_c superconductivity. In conventional superconductors, the electron-phonon interaction responsible for electron pairing and superconductivity was unequivocally established by tunneling and neutron scattering experiments, where peaks in the second derivative of the tunneling current d^2I/dV^2 corresponds to phonon modes observed by inelastic neutron scattering [55–57]. To obtain the equiva-

lent information in high-transition-temperature (high-T_c) copper oxide superconductors, it is important to identify the electron-boson coupling [58] (or the lack of [59]) and their connections to superconductivity. For bosonic "pairing glue" mediated superconductors, the "glue" may arise from the usual electron-phonon interaction [3] or the exchange of particle-hole spin fluctuations characterized by the imaginary part of the dynamic susceptibility, $\chi''(Q,\omega)$, seen in inelastic magnetic neutron scattering [60]. While tunneling experiments using scanning tunneling microscopy (STM) on hole-doped $Bi_2Sr_2CaCu_2O_{8-\delta}$ (BSCCO) have identified an oxygen lattice vibrational (bosonic) mode whose energy is anticorrelated with the superconducting gap energy scale and thus suggesting a strong electron-phonon coupling [61], similar experiments on electron-doped $Pr_{0.88}LaCe_{0.12}CuO_4$ (PLCCO, $T_c = 24$ K) have revealed a bosonic excitation (10.5 meV) at an energy consistent with spin-excitations rather than oxygen phonons [62]. However, previous measurements only covered small energy range and there is still some lack of knowledge about the overall dynamic susceptibility spectral weight redistribution across T_c. To extend the approach in conventional superconductors to high T_c superconductors in the frame work of Eliashberg function [55–57], accurate inelastic neutron scattering measurements of the bosonic spectra of spin excitations over a wide energy range and temperatures followed by high resolution tunneling spectroscopy on the same material is required.

If spin excitations in PLCCO are indeed responsible for the electron pairing and the bosonic mode seen by STM [62] in a manner similar to the role played by phonons in conventional superconductors, the energy spectrum of dynamic susceptibility $\chi''(Q,\omega)$ [39] should have the highest density of states at the mode energy (10.5 ± 2.5 meV). Although previous neutron scattering experiments on PLCCO have shown a clear magnetic intensity gain at ~ 10.5 meV below T_c, consistent with the collective spin excitation centers at the antiferromagnetic ordering wavevector $Q = (0.5, 0.5)$ termed "resonance" [27], the energy dependence of the $\chi''(Q,\omega)$ over a wide energy range at different temperatures was not established because the difficulty in separating the magnetic scattering from the nonmagnetic background using unpolarized neutrons. In this chapter, we studied the spin excitation spectra over a wide energy range ($0.5 < \hbar\omega < 30$ meV) at both normal state and superconducting state in electron doped cuprate $Pr_{0.88}LaCe_{0.12}CuO_{4-\delta}$ ($T_c = 24$ K) using both polarized and unpolarized inelastic neutron scattering. The polarized neutron

scattering can isolate the magnetic scattering from the phonon scattering and provide accurate spin dynamic susceptibility. We find in addition to the dominant dispersionless 10.5 meV "resonance" peak, the dynamic susceptibility $\chi''(Q,\omega)$ displays a second dispersive mode at around ~ 2 meV at both normal state and superconducting state, suggesting the low energy spin excitations are more structured than we expect [65]. More importantly, the overall spin excitations spectrum agree with the electron tunneling spectrum observed by the new tunneling experiment in the same sample [54], indicating the bosonic modes revealed by tunneling measurement may originate from the spin excitations, suggesting the strong electron spin excitation coupling in the system. Comparing with the electron phonon coupling in conventional superconductors, we conclude that the spin excitations is the most possible candidate for the pairing "glue" of the high-T_c superconductivity. Furthermore, the magnetic correlation function $S(Q,\omega)$ (< 1 meV) show that part of spin excitations are suppressed below T_c and are prominently in analog to those of $p-$type underdoped $La_{1.895}Sr_{0.105}CuO_4$ and $YBa_2Cu_3O_{6+\delta}$ [63, 66], suggesting a superconducting spin pseudo gap opens up.

3.2 Unpolarized and polarized neutron scattering experimental setup

We grew high quality $Pr_{0.88}LaCe_{0.12}CuO_4$ single crystals with mosaicity$< 1^\circ$ using the Traveling Solvent Floating Zone (TSFZ) method. The as-grown crystals are non-superconducting. After annealing in vacuum at around $800^\circ C$ for about four days, we got the optimally doped superconducting samples with onset superconducting transition temperature 24 K. This sample is phase pure superconductor without the anitiferromagnetic order different from another electron doped cuprate $Nd_{1.85}Ce_{0.15}CuO_{4-\delta}$, in which the static antiferromagnetic order coexists with the superconductivity. The neutron scattering experiments were carried out on the same sample as the tunneling experiment [54], thus avoiding uncertainties associated with different samples. We labeled the positions in reciprocal space at wave vector $\mathbf{Q} = (q_x, q_y, q_z)\mathring{A}^{-1}$ using $(H,K,L,)(r.l.u.)$ notation, where $(H,K,L) = (q_x a/2\pi, q_y b/2\pi, q_z c/2\pi)$. PLCCO has the body centered tetragonal unit cell with space group I_4/mmm and $a = b = 3.98\mathring{A}$, $c = 12.27\mathring{A}$. we coaligned three crystals (3g

per piece) with $(H, K, 0)$ as the scattering plane in the cryostat sample environment. We use polarized and unpolarized neutron scattering to detect the spin excitations near the antiferromagnetic zone center $\mathbf{Q} = (0.5, 0.5, 0)$ and $\mathbf{Q} = (1.5, -0.5, 0)$ with energy transfer from 0.5 to 30 meV. The unpolarized experiments are performed on cold neutron Spin-Polarized Inelastic Neutron-Scattering Spectrometer (SPINS) at NIST Center for Neutron Research. For the data collected from SPINS, the fixed final energy $E_f = 5$ meV and collimation $guid - open - 80' - open$ were used. Cooled Beryllium filter was put behind the sample to eliminate higher-order contamination of the scattered beam.

The polarized neutron scattering experiment was carried out on the thermal neutron three-axis spectrometer with polarization analysis IN20 at Institut Laue Langevin and the fixed final energy $E_f = 14.7$ meV was used. The polarization directions $P(100), (010), (001)$ are denoted as x, y, z direction, respectively (Fig. 3.1a). Momentum transfer $\mathbf{Q}$ is parallel to the x direction and xy plane is parallel to the scattering plane of the crystals. We labeled different neutron spin states as spin up $(+)$ and spin down $(-)$. Then spin-flip(SF) process and non-spin-flip (NSF) process can be denoted as $(\mp\pm)$ and $(\pm\pm)$, respectively. All measurements were performed with the incident polarization $P \parallel Q$ (Fig. 3.1a), for which magnetic scattering occurs entirely in the spin-flip (SF) channel and the nonmagnetic scattering occurs in the non spin-flip (NSF) channel.

3.3 Unpolarized neutron scattering experiment results

Figs. 3.1b-1g summarize the low energy constant-E scans along $[H, 1 - H, 0]$ at different temperatures on SPINS. The magnetic excitations are commensurate and centered at $(0.5, 0.5, 0)$ for all energies probed. Fig. 3.1b shows the spin excitation intensity is suppressed at 1 meV on cooling from normal state (24 K) to superconducting state (2 K), suggesting the system opens up a spin pseduogap. The spin excitations have little temperature dependence between 2 K and 24 K above 1.5 meV. With increasing temperature, the spin excitations disappear at about 150 K for all the energies probed. The Constant-Q scans at peak center $(0.5, 0.5, 0)$ and background $(0.56, 0.44, 0)$ meV again confirm the presence of superconducting spin pseduogap (Fig. 3.2a). In Fig. 3.2c, we obtain dynamic susceptibility $\chi''(Q, \omega)$ by correcting the magnetic correlation function $S(Q, \omega)$ for the ther-

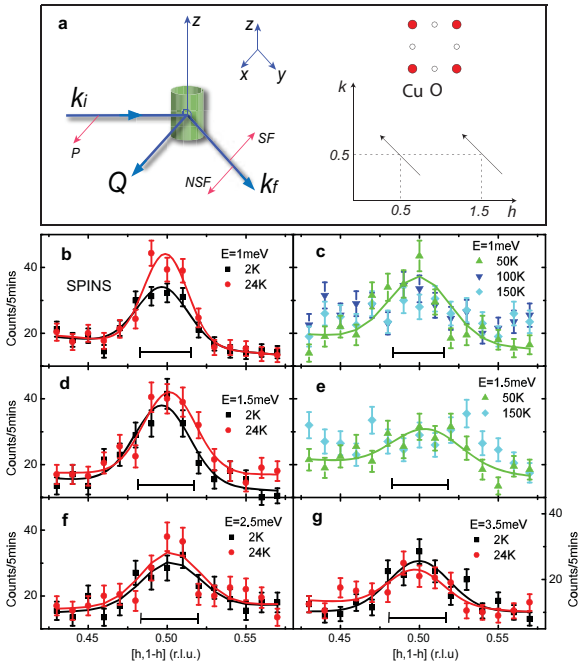

Figure 3.1: (a)Polarization directions of neutron in recipical space and schematic diagrams of real and reciprocal space of the CuO_2 plane, all neutron scattering experiments are performed near the antiferromagnetic zone center [$\mathbf{Q} = (0.5, 0.5, 0)$] or [$\mathbf{Q} = (1.5, 0.5, 0)$]; Transverse Qscans through [$\mathbf{Q} = (0.5, 0.5, 0)$] for (b),(c) $\hbar\omega = 1$ meV (d),(e) $\hbar\omega = 1.5$ meV (f) $\hbar\omega = 2.5$ meV (g) $\hbar\omega$ =3.5 meV at different temperatures; the horizontal bars are the instrument resolutions; the solid lines are Gaussian fits.

mal population factor. The energy dependence of dynamic susceptibility $\chi''(Q,\omega)$ displays a peak feature at ~ 2 meV (Fig. 3.2c). The mode is dispersive and shifts from 1.5 meV to 3 meV as the temperature increases from 2 K to 50 K. The peak is present in the normal state and diminishes at above 100 K, indicating the excitation is purely magnetic in origin. The spin fluctuations can be fitted with a simple Lorentzian $\chi''(\omega) \propto \Gamma\omega/(\Gamma^2+\omega^2)$ (Fig. 3.2c), as the spin fluctuation relaxation rate Γ increases as warming (Fig. 3.2d). The ~ 2 meV spin response at below the resonance mode seems conflicted with the "spin exciton" scenario, because in such a model the resonance mode is interpreted as an overdamped spin exciton located near the particle-hole continuum, below which the spin excitations should be gapped because of the opening of the superconducting gap. More importantly, we notice that this "double peak" structure is strikingly similar to the bosonic modes observed in the same sample by the tunneling experiment [54]. The detailed agreement between the tunneling spectrum and the neutron data on dynamic susceptibility is strong evidence that the charge carriers in PLCCO are coupled through a spin excitation mechanism. In the normal states above 50 K, we observe linear energy dependence of spin response as $E \to 0$ and the signals are suppressed as warming, which can be understood in an AFM Fermi liquid framework [69].

Fig. 3.3 shows the temperature dependence of the spin fluctuations below the spin pseudo gap (1 meV) and above the spin gap (3.5 meV). The peak intensity at 1 meV displays a "kink" structure at T_c, very much like that of underdoped $La_{1.895}Sr_{0.105}CuO_4$ and $YBa_2Cu_3O_{6+\delta}$ [63,66], suggesting the suppression of the spin excitations at low energy is due to the opening of superconducting gap below T_c. The spin gap is incomplete as there is still some intensity observed even at 2 K suggesting there is no clean spin gap, which could be due to the central mode like magnetic excitations as observed in underdoped YBCO and LSCO [63, 64, 66]. The temperature dependence at 3.5 meV is much weaker and exhibits negligible changes across T_c.

3.4 Polarized neutron scattering experiment results

In our previous measurement in PLCCO, we observed spin excitation enhancement at 10.5 meV upon entering superconducting state on unpolarized neutron triple axis spectrometer

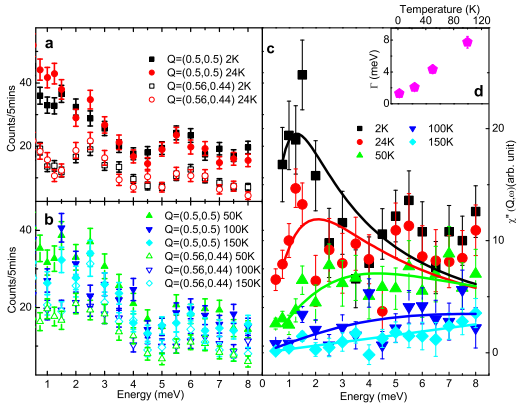

Figure 3.2: (a), (b) The energy scans at the antiferromagnetic zone center [$\mathbf{Q} = (0.5, 0.5, 0)$] and background away from the zone center [$\mathbf{Q} = (0.56, 0.44, 0)$] positions at various temperatures, showing a spin pseudo gap opens up below T_c; the corresponding $\chi''(\omega)$ are plotted in (c), displaying dispersive modes from 4 meV to 1.5 meV; the solid lines in (c) are fits to $\chi''(\omega) \propto \Gamma\omega/(\Gamma^2 + \omega^2)$ The inset (d) shows the temperature dependence of the relaxation rate Γ at different temperatures.

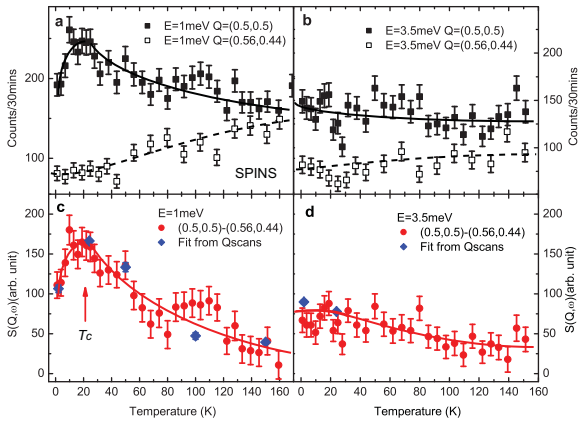

Figure 3.3: (a), (b) the temperature dependence of the scattering at antiferromagnetic zone center [$\mathbf{Q} = (0.5, 0.5, 0)$] and background away from the zone center [$\mathbf{Q} = (0.56, 0.44, 0)$] positions at $\hbar\omega = 1$ meV and $\hbar\omega = 3.5$ meV, respectively. (c) The background subtracted magnetic scattering at $\hbar\omega = 1$ meV, showing a kink structure at T_c. (d) The background subtracted magnetic scattering at $\hbar\omega = 3.5$ meV showing no anomaly across T_c; the solid lines are guided to the eye.

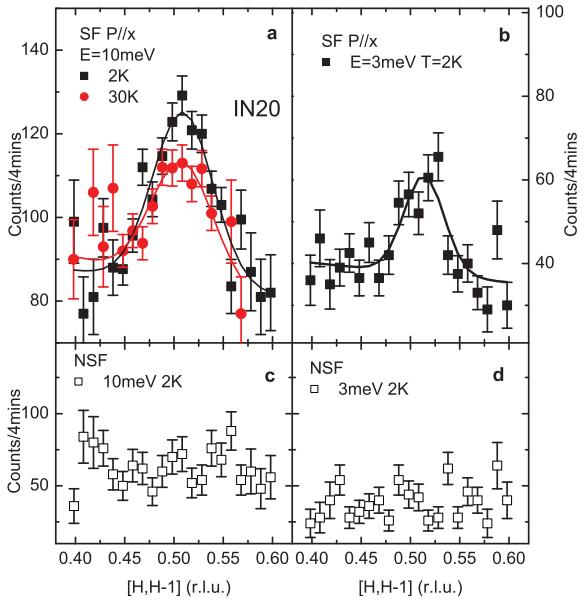

Figure 3.4: (a) IN20 measurements of **Q**-scans through [$\mathbf{Q} = (1.5, -0.5, 0)$] at $\hbar\omega = 10$ meV in spin-flip (SF) channel at 2 K and 30 K, showing a clear intensity enhancement on cooling from 30 K to 2 K consistent with the unpolarized neutron scattering data [27]. (b) **Q**-scans through [$\mathbf{Q} = (1.5, -0.5, 0)$] at $\hbar\omega = 3meV$ in spin-flip (SF) channel at 2K. (c), (d) **Q**-scans through [$\mathbf{Q} = (1.5, -0.5, 0)$] at $\hbar\omega = 10$ meV and $\hbar\omega = 3$ meV in non spin-flip (NSF) channel at 2 K; the solid lines are Gaussian fits.

[27]. The most unambiguous method to discriminate between magnetic neutron scattering and nuclear excitation is polarized neutron scattering. We performed polarized neutron scattering measurements on PLCCO at IN-20 triple axis spectrometer at a wider energy range, in order to separate the magnetic signal from the phonon scattering and other spurious contributions. Fig. 3.4 plots the Q-scans of both spin-flip (SF) channel and non spin-flip (NSF) channel at 2 K and 30 K with energy transfer 10 meV and 3 meV, respectively. At the SF channel (Fig. 3.4a), there is a signal enhancement on cooling from 30 K to 2 K at 10 meV. Fig. 3.4c and Fig. 3.4d show that they are featureless at the NSF channels therefore demonstrates that the resonance in PLCCO is magnetic excitations and has nothing to do with the phonon scattering or spurious effects.

In order to establish the over all feature of the energy dependence of the dynamic susceptibility, we measured the E-scans at the peak center $(1.5, -0.5, 0)$ and background $(1.64, -0.36, 0)$ at temperatures of 2 K and 30 K in both SF channel and NSF channel (Fig. 3.5). Fig. 3.5b shows the dynamic susceptibility $\chi''(Q, \omega)$ is dominated by a resonance

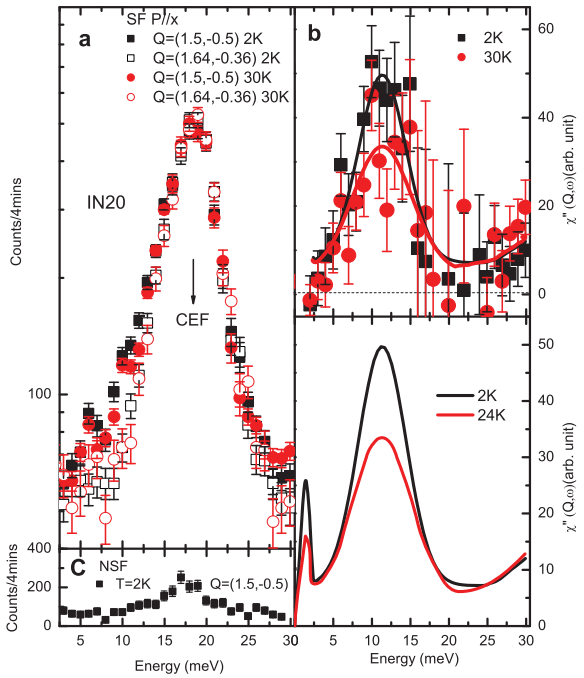

Figure 3.5: (a) IN20 measurements of the energy scans at the antiferromagnetic zone center [$\mathbf{Q} = (1.5, -0.5, 0)$] and background [$\mathbf{Q} = (1.64, -0.36, 0)$] positions at 2 K and 30 K in spin-flip (SF) channel, the Q independent 18 meV peak originates from a crystalline electric field (CEF) excitation [68]; the corresponding $\chi''(Q, \omega)$ are plotted in (b). (c) Energy scans at [$\mathbf{Q} = (1.5, -0.5, 0)$] in non spin-flip (NSF) channel. (d) Schematic plots of the $\chi''(Q, \omega)$ of the combined data with energy transfer from 0meV to 30meV in normal state and superconducting state.

mode at 10.5 meV. The mode is present at normal state and is strongly enhanced in superconducting state. This mode is consistent with the 10.5 meV mode in tunneling measurement [62]. Fig. 3.5c plots the over all features of the dynamic susceptibility by combining the SPINS data and IN20 data. The two peaks structure in the energy dependence of dynamic susceptibility is surprisingly similar to the bosonic modes revealed by the tunneling measurements [54].

3.5 Conclusions

If the magnetic excitation is the driving force of the superconductivity, there has to be sufficient spectral weight already present in the normal state. Detailed study of the redistribution of the spectral weight above and below T_c thus is important to develop theoretical

models. In hole doped cuprate YBCO, theorical calculations show that the change in the magnetic exchange energy between the normal and superconducting states is enough to account for the cuprate superconducting condensation energy [34, 67]. However, in the hole doped cuprates, the presence of the normal state pseudo gap and stripe phase which are the precursor or competing states of the superconducting phase makes these kind of theoretical calculations much more complicated and questionable. The electron doped PLCCO free of pseudo gap and stripe phase thus is a much "cleaner" system suitable for theoretical calculations. We note that in PLCCO the spin excitation "two peak" structure is still prominent in the normal state suggesting that the normal state spin excitation may carry enough spectrum as the driving force of high T_c superconductivity. Our results show that the imaginary part of the dynamic susceptibility $\chi''(Q,\omega)$ in PLCCO plays the similar role as the phonons of conventional BCS superconductors. In both cases, tunneling experiments observe the corresponding electron bosonic modes at the exactly same energies. In the BCS superconductors, the similarity between phonon density states spectrum and the tunneling electron bosonic spectrum has been considered as the direct evidence that phonon is the "paring glue" of conventional superconductivity. Hence, the spin excitation spectrum in PLCCO strongly suggest the spin excitations is the mediator ("pairing glue") of high T_c superconductivity.

Chapter 4

Structural and Magnetic Phase Diagram of $CeFeAsO_{1-x}F_x$

4.1 Introduction

A determination of the structural and magnetic phase transitions in doped transition metal oxides is essential for understanding their electronic properties. For high-transition-temperature (high-T_c) copper oxides, the parent compounds are antiferromagnetic (AFM) Mott insulators [70]. When mobile 'electrons' or 'holes' are doped into the parent compounds, the static long-range AFM order is rapidly suppressed and optimal superconductivity emerges after a complete suppression of the static AFM order [28, 71–73]. Much like copper oxide superconductors, high-T_c superconductivity in the recently discovered rare-earth Fe-based oxide systems RFeAsO (R, rare-earth metal) and $(Ba_{1-x}K_x)Fe_2As_2$ are also derived from either electron [7–11] or hole [74,75] doping of their semimetal parent compounds. Although the parent compound LaFeAsO also exhibits long range static AFM order that is suppressed upon electron doping to induce superconductivity [12], there has been no systematic measurement to establish the doping evolution of the AFM order and its relationship to superconductivity. A determination of the structural, magnetic, and superconductivity phase diagram in one of the RFeAsO systems will allow a direct comparison with the phase diagram of high-T_c copper oxides. Such a comparison is important because it might reveal whether the physics of high-T_c superconductivity in the Fe-based

materials is fundamentally related to that of the high-T_c copper oxides [76–81].

In this chapter, we show systematic neutron scattering studies of structural and magnetic phase transitions in the Fe pnictides $CeFeAsO_{1-x}F_x$ as the system is tuned from a semimetal to a high-T_c superconductor through F doping x. We find that CeFeAsO undergoes a structural lattice distortion from tetragonal to orthorhombic structure near 155 K followed by a commensurate AFM ordering on the Fe sublattice below 140 K as shown in Figs. 4.1 and 4.2, similar to that of LaFeAsO (ref. [12]). While the structural phase transition temperature decreases gradually with increasing F doping and disappears around $x = 0.1$ when superconductivity is already well developed (Fig. 4.3), the AFM ordering temperature and static Fe ordered moment reduce rapidly and essentially vanish before the emergence of superconductivity for $x > 0.6$, resulting an electron phase diagram shown in Fig. 4.1d similar to that of the electron-doped high-T_c copper oxides [72, 73]. Therefore, while superconductivity in $CeFeAsO_{1-x}F_x$ can survive in either the low-temperature tetragonal or orthorhombic crystal structure, it competes directly with static AFM order.

Our detailed analysis of the low temperature $CeFeAsO_{1-x}F_x$ structures reveals that F doping does not change the Fe-As distance but reduces the Ce-As distance and Fe-As-Fe angles (Fig. 4.4). These results suggest that the main effect of F doping is to transfer electrons from the Ce-O/F layers to the As-Fe-As block (Fig. 4.4a), thereby decreasing the distance between them due to increased Columb attraction with electron-doping. Comparison of the structural evolution of $CeFeAsO_{1-x}F_x$ with other rare-earth Fe pnictides [11, 12, 82, 83] and $(Ba_{1-x}K_x)Fe_2As_2$ [75, 84] suggests that the Fe-As-Fe bond angle decreases systematically for materials with increasing T_c (Fig. 4.5). The results suggest that the structural perfection of the Fe-As tetrahedral is crucial for the high-T_c superconductivity in these Fe pnictides.

4.2 Sample characterizations and elastic neutron scattering instruments

We use neutron diffraction to study the structural and magnetic phase transitions in polycrystalline nonsuperconducting $CeFeAsO_{1-x}F_x$ with x = 0, 0.02, 0.04, 0.06 (as confirmed by measurements using a commercial SQUID) and superconducting $CeFeAsO_{1-x}F_x$ with

x = 0.08, 0.10, and 0.16 (T_cs for x = 0.08 and 0.10 are shown in the insets of Fig. 4.4, and T_c for x = 0.16 is 35 K, all determined by the susceptibility measurement using a SQUID) using the method described in Ref. [9]. Our experiments are carried out on the BT-1 high resolution powder diffractometer and BT-7 thermal triple-axis spectrometer at the NIST Center for Neutron Research, Gaithersburg, Maryland. Some measurements were also performed on the HB-3 thermal triple-axis spectrometer at the High Flux Isotope Reactor, Oak Ridge National Laboratory.

4.3 Magnetic and lattice phase diagrams in $CeFeAsO_{1-x}F_x$

In previous work, it was found that LaFeAsO undergoes a structural distortion below 155 K, changing the symmetry from tetragonal (space group P4/nmm) to monoclinic (space group P112/n) [12] or orthorhombic (space group Cmma) [85], and followed by a long range commensurate AFM order with a collinear spin structure below 137 K [12]. For convenience in comparing the low temperature nuclear and magnetic structures, we use orthorhombic Cmma space group to describe the low temperature structural data in this chapter. Since $CeFeAsO_{1-x}F_x$ has rare earth Ce which carries a local magnetic moment [9] and therefore different from the nonmagnetic La in $LaFeAsO_{1-x}F_x$ (ref. [12]), we first need to determine whether this material has the same lattice distortion and magnetic structure as those of $LaFeAsO_{1-x}F_x$. Our high-resolution neutron powder diffraction measurements on BT-1 confirm that the lattice symmetry of CeFeAsO also displays the tetragonal to orthorhombic transition below 158 K (Figs. 4.1d and 4.2a), where the $(2,2,0)_T$ peak in the tetragonal phase is split into $(0,4,0)_O$ and $(4,0,0)_O$ peaks in the orthorhombic phase (inset in Fig. 4.2a).

To see if the Fe spins in CeFeAsO exhibit the same magnetic order as that of LaFeAsO (ref. [12]), we carried out measurements on BT-7. The Ce moments order magnetically below 4 K (ref. [9] and Fig. 4.2e), we took data at 40 K to avoid any possible induced-moment influence of Ce on the intensities of the Fe magnetic peaks (Fig. 4.1c). Comparison of Fig. 4.1c with the same scan at 160 K and with Fig. 4.3c in ref. [12] for LaFeAsO immediately reveals that the Fe magnetic unit cell in CeFeAsO can be indexed as $\sqrt{2}a_N \times \sqrt{2}b_N \times c_N$, where a_N, b_N, and c_N are nuclear lattice parameters of the unit cell (see Table 2a).

This indicates that CeFeAsO has the same collinear in-plane Fe AFM structure as that of LaFeAsO, but the c-axis nearest-neighbor spins are parallel in CeFeAsO rather than anti-parallel as in LaFeAsO. Hence there is no need to double unit cell along the c-axis (Fig. 4.1a), and an excellent fit to the data is achieved using the magnetic and nuclear unit cells in Figs. 4.1a and 1b as shown by the solid red line of Fig. 4.1c. The ordered iron moment is 0.8(1) μ_B at 40 K, where numbers in parentheses indicate uncertainty in the last decimal place and μ_B denotes Bohr magneton. The magnitude of the Fe moment in CeFeAsO is about twice that of the Fe ordered moment in LaFeAsO (ref. [12]). We also determined the Ce magnetic structure using data collected at 1.7 K and found a strong coupling between the Fe and Ce moment below 20 K (Figs. 4.2e-4.2g). The Ce and Fe ordered moments at 1.7 K are 0.83(2) μ_B/Ce and 0.94(3) μ_B/Fe, respectively. Our determined Ce and Fe magnetic structures are shown in Figs. 1a and 1b. The lack of the c-axis unit cell doubling in the Fe magnetic structure of CeFeAsO is different from that of LaFeAsO, but identical to the Fe spin structure in PrFeAsO which has an Fe ordered moment of 0.48(9)μ_B/Fe (refs. [86, 87]. On the other hand, Fe magnetic ordering in NdFeAsO has the same spin structure as LaFeAsO but with a moment of only 0.27(7) μ_B/Fe (ref. [88]). Assuming that the observed AFM order in different rare-earth oxypnictides indeed arises from spin-density-wave (SDW) instability in a nested Fermi surface [79–81, 89] it is unclear how the different observed Fe AFM structures/moments for different rare-earth oxypnictides can be explained by their differences in band structures, as most of the calculations are carried out for LaFeAsO.

Having shown that the lattice distortion and Fe magnetic unit cells are rather similar between CeFeAsO and LaFeAsO, it is important to determine the evolution of the lattice and magnetic structures with increasing F doping as superconductivity is induced. If the collinear AFM order in CeFeAsO and LaFeAsO is a SDW instability arising from a nested Fermi surface [79–81, 89] similar to that of the pure metallic Cr (ref. [90, 91]), electron doping will change the electron and hole pocket sizes, but may induce incommensurate SDW order33. For Cr (refs. [90, 91]), where the SDW order has a long wavelength incommensurate magnetic structure, electron/hole doping quickly locks the SDW to commensurate antiferromagnetism with an ordered moment that is doping independent [90]. Fig. 4.2 summarizes the structural and magnetic phase transition temperatures for $CeFeAsO_{1-x}F_x$

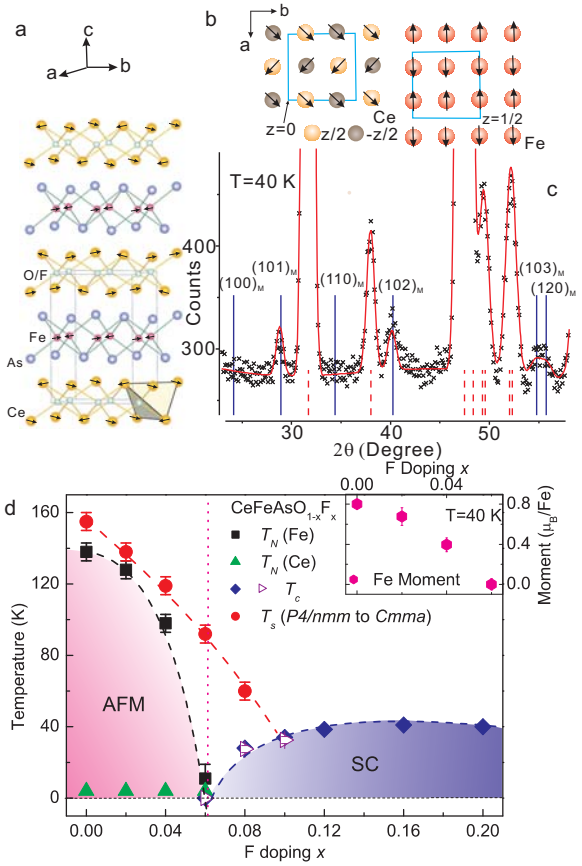

Figure 4.1: Low temperature magnetic structures for Ce and Fe in CeFeAsO and the structural and magnetic phase diagram of $CeFeAsO_{1-x}F_x$. The data in panel c) were collected using BT-7 with an incident beam wavelength $\lambda = 2.36$ Åwith pyrolytic graphite (PG) (0,0,2) as monochromator and PG filter. a) The three dimensional antiferromagnetic structures of Ce and Fe as determined from our neutron diffraction data. b) The magnetic unit cells of Ce and Fe. The Fe moments lie in the a-b plane and form an antiferromagnetic collinear structure similar to that of LaFeAsO (ref. [12]), while nearest-neighbor spins along the c-axis are parallel and so there is no need to double the magnetic cell along the c-axis. c) Observed (crosses) and calculated (solid line) neutron powder diffraction intensities of CeFeAsO at 40 K using space group Cmma for nuclear structure and a,b) for magnetic structure. The dashed vertical lines indicate the expected nuclear Bragg peak positions while the solid vertical lines represent magnetic Bragg peak positions for the spin structure of the right panel of b). d) The structural and magnetic phase diagram determined from our neutron measurements on $CeFeAsO_{1-x}F_x$ with $x = 0, 0.02, 0.04, 0.06, 0.08, 0.10, 0.16$. The red circles indicate the onset temperature of P4/nmm to Cmma phase transition. The black squares and green triangles designate the Neel temperatures of Fe T_N(Fe) and Ce T_N(Ce), respectively, as determined from neutron measurements in Figs. 4.2e-4.2h. The superconducting transition temperatures for $x = 0.08, 0.012, 0.016, 0.20$ (blue diamond) are from the onset T_c of the resistivity measurements adapted from ref. [9]. The open triangles are T_c determined from susceptibility measurements in Fig. 4.3. The inset in d) shows the F doping dependence of the Fe moment as determined from the intensity of the $(1, 0, 2)_M$ magnetic peak at 40 K, where the influence of the Ce moment on the Fe magnetic Bragg peak intensity can be safely ignored.

with $x = 0, 0.02, 0.04, 0.06$. Inspection of Figs. 2a-2d and their insets immediately reveals that the onset lattice distortion temperature (seen as the initial drop in $(2,2,0)_T$ peak intensity) and the magnitude of the lattice distortion (the low temperature splitting of the $(0,4,0)_o$ and $(4,0,0)_o$ peaks) both decrease gradually with increasing x (Fig. 4.1d). On the other hand, the wavevector positions and coherence-length limits of the $(1,0,2)_M$ magnetic peaks $Q = 1.838(1)$, 1.833(1), 1.837(1), and 1.831(3) $\text{Å}^{-1}; and \xi =$ 140(6), 137(8), 134(11), and 140(30) Åfor $x = 0$, 0.02, 0.04, 0.06, respectively (see inset of Fig. 4.2g)] are doping independent, and indicate no observable commensurate to incommensurate phase transition. The integrated intensity of the $(1,0,2)_M$ magnetic peak decreases rapidly with increasing x and essentially vanishes near $x = 0.06$ (inset in Fig. 4.1d). The corresponding Nel temperatures for T_N(Fe) and T_N(Ce) are determined by measuring the temperature dependence of the $(1,0,2)_M$ magnetic reflection (Figs. 4.2e-4.2h).

To see if the tetragonal to orthorhombic structural phase transition in $CeFeAsO_{1-x}F_x$ can survive superconductivity which appears for samples with $x > 0.06$ (ref. [9], we carried out additional measurements on $x = 0.08$, 0.10 samples at BT-1 and BT-7. Susceptibility measurements in the insets of Figs. 4.3a and 4.3b show the onset superconductivity of 27 K and 33 K for x = 0.08, and 0.10 samples, respectively. Although the $(2,2,0)_T$ peak does not reveal a clear splitting at 1.5 K indicative of an orthorhombic distortion for the $x = 0.08$ sample, its width at low temperature is clearly broader than that at 175 K (Fig. 4.3a). Detailed analysis of the BT-1 spectra confirms that the Cmma space group describes the low-temperature data better than the P4/nmm space group, thus indicating that superconductivity can survive either the tetragonal or orthorhombic crystal structure. To determine the tetragonal to orthorhombic phase transition temperature, we carefully measured the temperature dependent profile of the $(2,2,0)_T$ peak. Figure 3c shows the full-width-at-half-maximum (FWHM) of the peak as a function of temperature and it is clear that the tetragonal to orthorhombic phase transition occurs near 60 K. For comparison, we also carried our similar measurements for the $x = 0.10$ sample (Fig. 4.3b). Although analysis of the low temperature BT-1 spectrum again suggests that the Cmma space group fits the data better than the P4/nmm space group, the diminishing differences between the tetragonal and orthorhombic crystal structures means we were unable to determine a structural phase transition temperature. Thermal triple-axis measurements on the $x =$

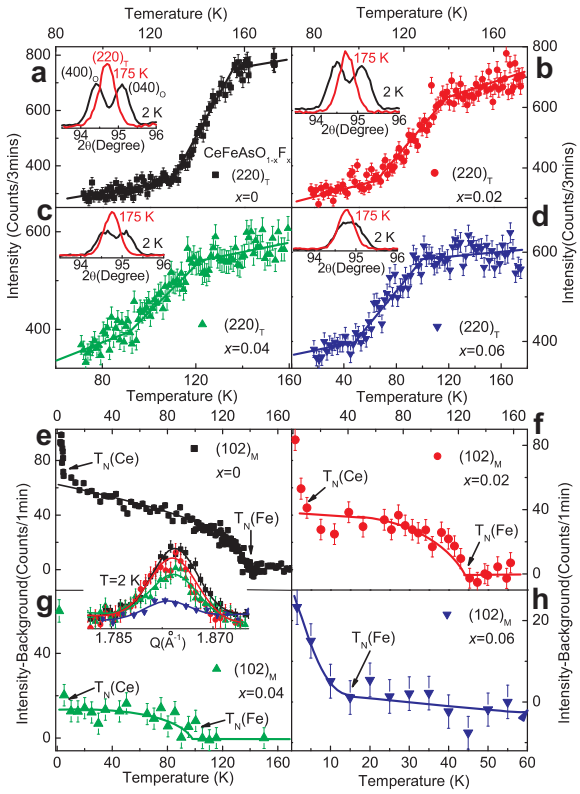

Figure 4.2: Structural and magnetic phase transition temperatures as a function of increasing F doping in $CeFeAsO_{1-x}F_x$. The data in a-d) and e-g) were collected on BT-1 and BT-7, respectively. The Q-scan for $x = 0.06$ (inset in e) and h) were carried out on HB-3 using similar setup as BT-7. The BT-1 diffractometer has a Ge(3,1,1) monochromator and an incident beam wavelength of $\lambda = 2.0785$ Å. a-d) Temperature dependence of the (2,2,0)T (T denotes tetragonal) nuclear reflection indicative of a structural phase transition [12] for various x. The insets show the (2,2,0)T reflection above and below the transition temperatures [12]. e-h) Temperature dependence of the order parameter at the magnetic Bragg peak position $(1, 0, 2)_M$ as a function of F doping. The large increase in intensity below 4 K is due to Ce ordering, as confirmed by temperature dependence of the Ce-only magnetic Bragg peak $(0, 0, 1)_M$. The inset shows the doping dependence of the $(1, 0, 2)_M$ Bragg peak normalized to the nuclear Bragg peak intensity. The peak positions and widths are essentially doping independent, suggesting that the AFM order is commensurate at all doping levels.

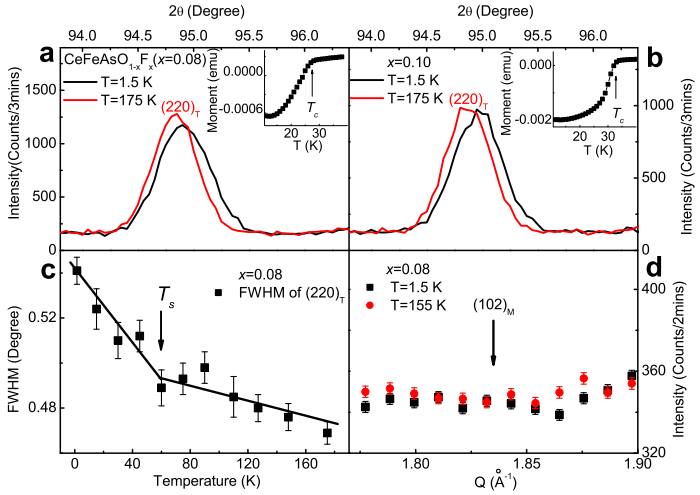

Figure 4.3: Low temperature lattice structure and tetragonal to orthorhombic structural phase transition temperature for superconducting $CeFeAsO_{1-x}F_x$ with $x = 0.08, 0.10$. The data were collected on BT-1 and BT-7 using identical experimental setup as that of Fig. 4.2. a-b) Temperature dependence of the $(2,2,0)_T$ (T denotes tetragonal) nuclear reflection at 175 K and 1.5 K. In both cases, the width at 1.5 K is broader than that at 175 K. However, the width is larger in the case of $x = 0.08$ at 1.5 K. The insets show the superconductivity transition temperature of the neutron samples measured by a SQUID. c) Temperature dependence of the $(2,2,0)_T$ Bragg peak width for the $x = 0.08$ sample, which shows a clear kink around 60 K indicating a tetragonal to orthorhombic phase transition. d) Temperature dependence of the scattering near the $(1,0,2)_M$ position (as marked by the arrow) for the $x = 0.08$ sample. They are featureless indicating no static AFM order.

0.08 sample reveals no evidence of static long range AFM Fe ordering (Fig. 4.3d), thus suggesting that static AFM order competes directly with superconductivity. To summarize the systematic work of Figs. 4.2 and 4.3, we plot in Fig. 4.1d the structural and magnetic phase diagram of $CeFeAsO_{1-x}F_x$ together with superconducting transition temperatures determined from susceptibility measurements on neutron samples and earlier work [9].

Fig. 4.4 summarizes the impact of F-doping on the crystal structure of $CeFeAsO_{1-x}F_x$ obtained from our detailed refinement analysis of the BT-1 data. The undoped CeFeAsO has an orthorhombic low-temperature structure with $c > a > b$ (Fig. 4.4a). Doping fluorine gradually suppresses both the a (the long Fe-Fe nearest-neighbor distance) and c-axes lattice constants while leaving the b-axis (the short Fe-Fe nearest-neighbor distance) essentially unchanged (Fig. 4b). The system almost becomes tetragonal at $x = 0.10$ with

a = b, and the c-axis lattice constant continues to decreasing with increasing doping for $x > 0.10$. The reduction in the c-axis lattice constant is achieved via a large reduction of the Ce-As distance, while the Ce-O/F and As-Fe-As block distances actually increase with increasing F-doping (Figs. 4.4c and 4.4e). This suggests that the effect of F-doping is to bring the Ce-O/F charge transfer layer closer to the superconducting As-Fe-As block, and thereby facilitating electron charge transfer (Fig. 4.4a) as confirmed by recent X-ray absorption spectroscopy measurements [92]. Since the Fe-As distance (2.405 Å) is essentially doping independent (Fig. 4.3e), the strong hybridization between the Fe 3d and the As 4p orbitals is not affected by electron-doping. On the other hand, if we assume that the Fe-Fe nearest-neighbor (J_1) and next-nearest-neighbor effective exchange couplings (J_2) are mediated through the electron Fe-As-Fe hopping and controlled by the Fe-As-Fe angles, Fig. 4.4d suggests that J_2 and one of the nearest-neighbor exchange constants (J_1) decrease with increasing F-doping while the other J_1 remains unchanged.

4.4 Evolution of Fe-As-Fe bond angles

In a previous work on the phase diagram of oxygen deficient $RFeAsO_{1-\delta}$(ref. [10]), it was found that systematically replacing R from La, to Ce, Pr, Nd, and Sm in $RFeAsO_{1-\delta}$ resulted a gradual decrease in the a-axis lattice parameters and increase in T_c. If T_c for different Fe-based superconductors is indeed correlated to their structural properties, one would expect to find a systematic trend between T_c and the Fe-As-Fe bond angles, since the exchange couplings (J_1 and J_2) are directly related to the Fe-As-Fe bond angles [76,94] (Fig. 4.5a). Figs. 5b and 5c plot the Fe-As(P)-Fe angles and Fe-Fe/Fe-As(P) distances versus maximum T_c for different Fe-based rare-earth oxypnictides [12, 82–85, 95, 96] and $Ba_{1-x}K_xFe_2As_2$ (ref. [75]) superconductors. While the Fe-Fe/Fe-As(P) distances may not have a clear trend amongst different Fe-based superconductors, it is remarkable that the maximum T_c appears to be directly related to the Fe-As(P)-Fe angles for a variety of materials (Fig. 4.5c) and the highest T_c is obtained when the Fe-As(P)-Fe angle reaches the ideal value of 109.47° for the perfect FeAs tetrahedron with the least lattice distortion This suggests that the most effective way to increase T_c in Fe-based superconductors is to decrease the deviation of the Fe-As(P)-Fe bond angle from the ideal FeAs tetrahedron, as

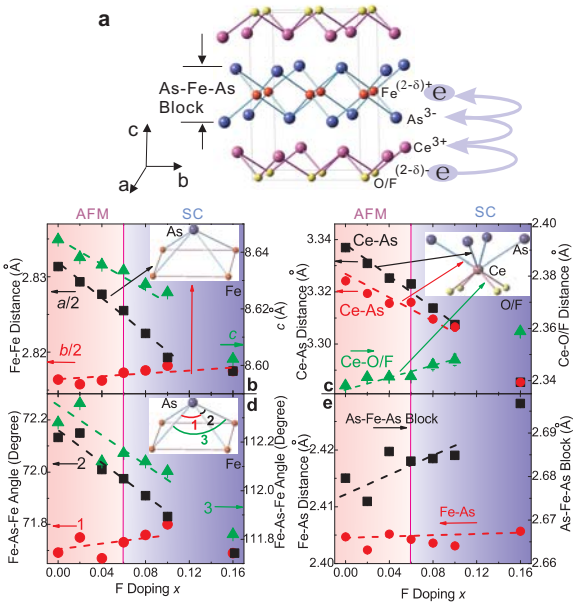

Figure 4.4: Low temperature structural evolution of $CeFeAsO_{1-x}F_x$ as a function of F doping obtained from analysis of the BT-1 data. The atomic positions of $CeFeAsO_{1-x}F_x$ are shown in Table 2b and the effect of F doping is to expand the Fe-As-Fe block and to move the Ce-O/F block closer to Fe-As-Fe block, thereby facilitating electron doping to the superconducting Fe-As-Fe layer. a) schematic diagram defining the Fe-As-Fe block and illustrating the process of electron doping. b) a, b, c lattice constants of the orthorhombic unit cell and the two Fe-Fe nearest-neighbor distances as a function of F doping. There is no observable anomaly across the antiferromagnetic to superconductivity phase boundary around x = 0.06. c) Ce-O/F and Ce-As distances as a function of F doping. The slight increase in the Ce-O/F block size is compensated by much larger reduction in the Ce-As distance, resulting an overall c-axis lattice contraction as shown in b). d) Fe-As-Fe bond angles as defined in the inset versus F doping. While angle 1 hardly changes with doping, angles 2 and 3 decrease substantially with increasing F doping. e) The Fe-As bond distance and As-Fe-As block size versus F doping. The Fe-As distance is independent of F doping.

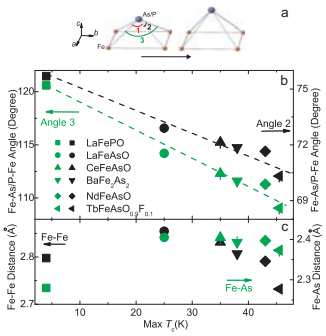

Figure 4.5: Fe-As(P)-Fe bond angles, Fe-Fe, and Fe-As(P) distances for different Fe-based superconductors. There is a systematic decrease in the Fe-As(P)-Fe bond angle for Fe-based superconductors with higher T_c, suggesting that the lattice effects are important. a) Schematic illustration of what happens to the Fe-As-Fe tetrahedron for Fe-based superconductors as a function of increasing T_c. b,c) Dependence of the maximum-T_c on Fe-As(P)-Fe angle and Fe-Fe/Fe-As(P) distance. The Fe-As(P)-Fe angles and Fe-Fe/Fe-As(P) distances are computed using atomic positions given in Refs. [83, 95] for LaFePO; Ref. [12] for LaFeAsO; present chapter for CeFeAsO; Ref. [84] for $BaFe_2As_2$; Ref. [96] for NdFeAsO; and Ref. [11] for $TbFeAsO_{0.9}F_{0.1}$. The maximum T_c is obtained when Fe-As(P)-Fe bond angle reaches the ideal value of 109.47° for the perfect FeAs tetrahedron. Note here we used the maximum-T_c obtained from susceptibility measurement, which is lower than that of the resistivity measurement on the same system.

the geometry of the FeAs tetrahedron might be correlated with the density of states near the Fermi energy.

Table 2a. Refined structure parameters of $CeFeAsO_{1-x}F_x$ with $x = 0$ at 175 K and $x = 0.16$ at 60 K. Space group: P4/nmm. CeFeAsO, $a = 3.99591(5)$, $c = 8.6522(1)$ Å; $CeFeAsO_{0.84}F_{0.16}$, a = 3.98470(3), c = 8.6032(1)Å.

Atom	site	x	y	z($x=0$)	BÅ^2($x=0$)	z($x=0.16$)	BÅ^2($x=0$)
Ce	2c	$\frac{1}{4}$	$\frac{1}{4}$	0.1413(3)	0.34(4)	0.1480(4)	0.58(5)
Fe	2b	$\frac{3}{4}$	$\frac{1}{4}$	$\frac{1}{2}$	0.25(4)	$\frac{1}{2}$	0.09(3)
As	2c	$\frac{1}{4}$	$\frac{1}{4}$	0.6546(2)	0.28(3)	0.6520(3)	0.27(4)
O	2a	$\frac{3}{4}$	$\frac{1}{4}$	0	0.30(5)	0	0.50(4)

x = 0, Rp =5.02%, wRp = 6.43%, $\chi^2 = 0.336$; x = 0.16, Rp =5.94%, wRp = 8.24%, $\chi^2 = 2.525$

Table 2b. Refined structure parameters of $CeFeAsO_{1-x}F_x$ with $x = 0, 0.02, 0.04, 0.06, 0.08, 0.10$ at 1.4 K. Space group: Cmma. Atomic positions: Ce: 4g (0, 1/4, z); Fe: 4b (1/4, 0, 1/2), As: 4g (0, 1/4, z), and O/F: 4a (1/4, 0, 0).

Atom	a	x=0	x=0.02	x=0.04	x=0.06	x=0.08	x=0.10
	a(Å)	5.66263(4)	5.65865(9)	5.6553(1)	5.6511(1)	5.6450(2)	5.6386(7)
	b(Å)	5.63273(4)	5.63155(9)	5.6325(1)	5.6346(1)	5.6352(2)	5.6364(7)
	c(Å)	8.64446(7)	8.6382(1)	8.6355(2)	8.6335(1)	8.6287(1)	8.6258(2)
Ce	z	0.1402(2)	0.1417(4)	0.1419(4)	0.1420(3)	0.1432(4)	0.1439(5)
	B(Å^2)	0.36(2)	0.37(6)	0.31(6)	0.46(5)	0.18(6)	0.51(6)
Fe	B(Å^2)	0.34(2)	0.38(4)	0.30(3)	0.34(3)	0.06(3)	0.14(4)
As	z	0.6553(1)	0.6548(3)	0.6555(3)	0.6554(2)	0.6555(3)	0.6556(3)
	B(Å^2)	0.45(2)	0.50(6)	0.36(5)	0.24(4)	0.17(5)	0.18(5)
O/F	B(Å^2)	0.54(2)	0.53(6)	0.64(6)	0.63(5)	0.24(5)	0.44(6)
	Rp(%)	4.31	5.44	4.90	4.71	4.66	5.01
	wRp(%)	5.60	6.72	6.31	6.16	5.92	6.34
	χ^2	2.192	1.258	0.966	0.9622	1.067	1.023

4.5 Conclusions

In summary, we have mapped out the structural and magnetic phase transitions of $CeFeAsO_{1-x}F_x$ and found that the Fe static AFM order essentially vanishes before the appearance of superconductivity [97]. The phase diagram of $CeFeAsO_{1-x}F_x$ is therefore remarkably similar to that of the electron-doped high-T_c copper oxides. In a recent μSR and 57Fe Mossbauer spectroscopy work on the phase diagram of $LaFeAsO_{1-x}F_x$, Luetkens et al. [98] argue that antiferromagnetism to superconductivity transition is first order and orthorhombic structure does not coexist with superconductivity. In contrast, X-ray scattering [99] and

μSR experiments [100] on $SmFeAsO_{1-x}F_x$ suggest that a coexistence of static antiferromagnetism and orthorhombic structure with superconductivity in the underdoped regime. While our neutron diffraction experiments confirm no static AFM order for $LaFeAsO_{1-x}F_x$ at x = 0.05 consistent with the μSR work [98], we find clear evidence for the orthorhombic lattice distortion [101]. These results suggest that the orthorhombic structure can survive superconductivity in $LaFeAsO_{1-x}F_x$, much like $CeFeAsO_{1-x}F_x$ discussed here and $SmFeAsO_{1-x}F_x$ (ref. [100]). Since superconductivity in $LaFeAsO_{1-x}F_x$ (refs. [95, 98], $CeFeAsO_{1-x}F_x$ (ref. [9]), and $SmFeAsO_{1-x}F_x$ (refs. [99, 100, 102]) systems first appear for $x = 0.05$, 0.08, and 0.10 respectively. It is possible that the first order like phase transition between antiferromagnetism to superconductivity in $LaFeAsO_{1-x}F_x$ (ref. [98]) gradually evolves into Fig. 4.1d for $CeFeAsO_{1-x}F_x$ before becoming that for $SmFeAsO_{1-x}F_x$ (refs. [99, 100, 102]).

In addition to suppressing the static antiferromagnetism and inducing superconductivity, F doping also reduces the long-axis of the orthorhombic structure in the undoped CeFeAsO and decreases the Fe-As-Fe bond angles. Comparison of structural parameters of various Fe-based superconductors reveals that the Fe-As(P)-Fe bond angle decreases systematically for superconductors with increasing T_cs and reaches its maximum value for the ideal FeAs tetrahedral angle. This means that the structural distortion from the ideal FeAs tetrahedron is critical to the superconducting transition temperature and must be taken into account as we consider a mechanism for high-T_c superconductivity in these Fe-based materials.

Chapter 5

Magnetic and Lattice Structures of PrFeAsO, $PrFeAsO_{0.85}F_{0.15}$ and $PrFeAsO_{0.85}$

5.1 Introduction and motivation

The parent compounds (RFeAsO, R=La,Ce,Nd; AFe_2As_2, A=Ba, Sr,) of the iron-based superconductors investigated so far display a similar antiferromagnetic phase transition accompanying a tetragonal to orthorhombic structural distortion on cooling from 250 K to 100 K [12, 88, 89, 105–109, 111, 120]. As shown in Chapter 4, upon doping with fluorine (F), the long range antiferromagnetic order is gradually suppressed before superconductivity appears, indicating a remarkably similar electron phase diagram as the copper oxide superconductors [106]. Although the lattice structure and magnetic properties of $RFeAsO_{1-x}F_x$ (R=La,Ce,Nd) are similar, the maximum superconducting temperature T_c of doped $RFeAsO_{1-x}F_x$ is dramatically different, increasing from 26 K to 50 K when R changes from the non-magnetic element La to magnetic elements Ce, Nd and Pr. The sensitivity of the superconductivity to rare earth substitution is really surprising, and completely different from copper oxide superconductors in which the superconductivity is only sensitive to the element substitution within the CuO_2 plane (except for the case of $PrBa_2Cu_3O_{6+x}$ and $CeBa_2Cu_3O_{6+x}$). In order to understand how the rare earth substi-

tution controls the T_c, it is important to study how the rare earth substitution affects the lattice and magnetic structure and the resulting electron band structures.

Here we present neutron scattering studies of the parent compound PrFeAsO and its superconducting counterpart $RFeAsO_{1-x}F_x$, which possesses the highest T_c in the FeAs-based superconductor series [112]. Furthermore, since superconductivity in PrFeAsO can also be induced by forming oxygen vacancies, comparing the structure and magnetic properties of the F-doped and oxygen deficient samples should provide some clues to understanding the role of doping in the FeAs-based class of superconductors. Here we investigate the structure and magnetic properties of the parent compound PrFeAsO and its superconducting counterparts $PrFeAsO_{0.85}F_{0.15}$ (T_c = 52 K) and $PrFeAsO_{0.85}$ (T_c = 52 K) by elastic neutron scattering. We find that PrFeAsO undergoes a structural distortion from tetragonal to orthorhombic symmetry near 153 K, accompanied by a magnetic transition to commensurate antiferromagnetic order of the Fe spins at 127 K. These results, taken together with the observations of magnetic order in all the other systems which have been investigated to date [12,88,105–109,111,120], demonstrate that the antiferromagnetic order is universal for the parent compounds of the FeAs-based superconductors. Upon 15% F doping, both the structural distortion and magnetic order are suppressed, identical to the other FeAs-based superconductors. We also find that the structural distortion and magnetic order are suppressed in the oxygen-deficient superconducting $PrFeAsO_{0.85}$ sample. Thus, removing oxygen from PrFeAsO has the same impact on the structural and magnetic properties as doping F in the system.

5.2 Experimental details

We have employed neutron diffraction to study the structural and magnetic order in polycrystalline samples of PrFeAsO, $PrFeAsO_{0.85}F_{0.15}$ (T_c = 52 K) and $PrFeAsO_{0.85}$ (T_c = 52 K). The samples were synthesized by a high pressure method as described in ref [112]. Our neutron scattering experiments were carried out on the BT-1 powder diffractometer at the NIST Center for Neutron Research (NCNR), using the Ge(3,1,1) monochromator with an incident beam wavelength of λ = 2.0785 Å. The collimations before and after the monochromator and after the sample were 15', 20', and 7' full-width-at-half-maximum

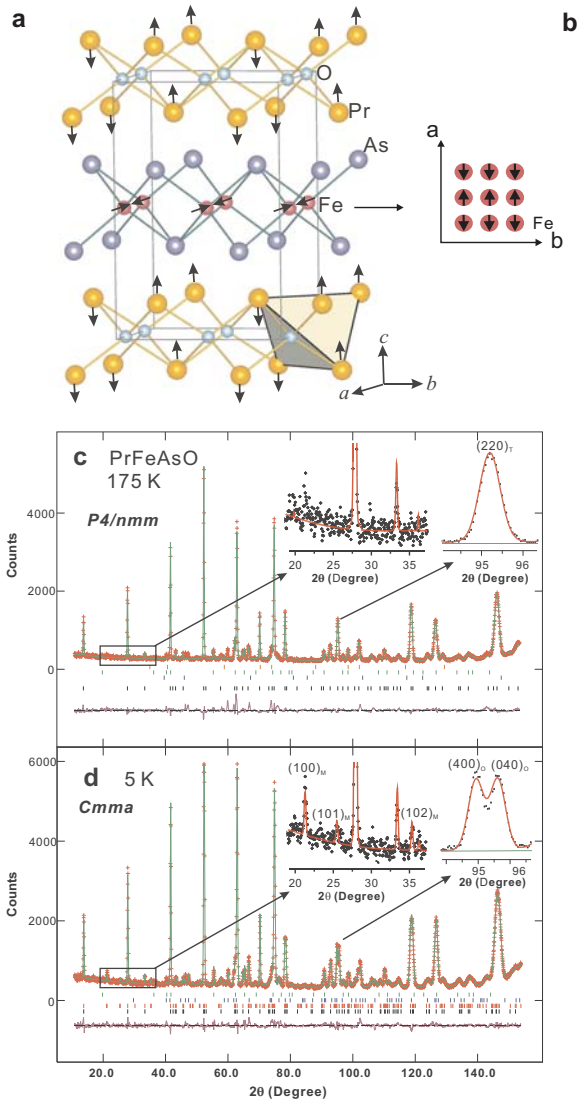

Figure 5.1: Lattice and magnetic structures for Fe and Pr in undoped PrFeAsO. a) The three dimensional antiferromagnetic structures of Fe and Pr as determined from the refinements of our neutron diffraction data. b) The magnetic structure of Fe in the FeAs plane. c) Observed (crosses) and calculated (solid line) neutron diffraction intensities of PrFeAsO at 175 K, in the tetragonal structure with space group P4/nmm. The inset shows the detailed data for $18^\circ < 2\theta < 38^\circ$ where most of the observable magnetic peaks are located. 2θ the diffraction angle, and the short vertical lines show the Bragg peak positions. No magnetic peaks are observed at 175 K. The (purple) trace indicates the intensity difference between the observed and calculated structures. d) Diffraction data at 5 K, fit with the orthorhombic structure of space group Cmma. The inset plots the detailed data in $18^\circ < 2\theta < 38^\circ$ showing three indexed magnetic peaks at 5 K, along with the observed splitting of the structural peak. The magnetic peaks are accounted for by the combined contributions of Fe and Pr. The (1,0,0) peak vanishes completely above the Pr Neel temperature of 14 K, while the (1,0,1) and (1,0,2) peaks persist above 14 K and vanish at 127 K as shown in Fig. 5.2b.

(FWHM), respectively. Magnetic order parameters were taken on the HB-3 thermal triple-axis spectrometer at High Flux Isotope Reactor, Oak Ridge National Laboratory, with an incident beam wavelength $\lambda = 2.36$ Åwith pyrolytic graphite (PG) (0,0,2) as monochromator and PG filters. Collimations in these configurations were coarse (typically $40' - 50'$), for intensity reasons.

Our high-resolution measurements on BT-1 show that the high temperature structure (175 K) in PrFeAsO can be well described by the expected tetragonal structure of space group P4/nmm (Fig. 5.1c). The refined structural parameters are listed in Table 1a. Fig. 5.1d shows the low temperature (5 K) diffraction pattern and refinement profiles for PrFeAsO, which can be described with the orthorhombic structure of space group Cmma. The orthorhombic distortion splits the $(220)_T$ of the tetragonal structure into two peaks, $(400)_O$ and $(040)_O$ in the orthorhombic structure, as shown in the inset of Fig. 5.2a. The insets in Fig. 5.1c and 1d show the details of the diffraction pattern for 2θ between 20 to 37 degrees, where most of the observable magnetic peaks are located. We can clearly see several magnetic peaks at 5 K, which can be simply indexed with the expected commensurate magnetic structure. These peaks are absent in the 175 K diffraction pattern, indicating that we are in the paramagnetic state at this temperature. Refinements using the GSAS program give excellent fits for the low temperature diffraction pattern, where the magnetic peaks are well accounted for by the combined Pr and Fe antiferromagnetic order as shown in Fig. 5.1a and 5.1b. The Fe magnetic unit cell can be indexed as $\sqrt{2}a_N \times \sqrt{2}b_N \times c_N$, which is exactly the same as for CeFeAsO [106]. The Fe spins order antiferromagnetically along the orthorhombic a axis and ferromagnetically along the b and c axis, with the moment direction along the a axis. The measured static ordered Fe moment is 0.48(9) μ_B at 5 K, where numbers in parentheses indicate one standard deviation statistical uncertainty in the last decimal place and μ_B denotes the Bohr magneton. The Pr spins order antiferromagnetically as shown in Fig. 5.1a. The static ordered Pr moment is 0.84(4) μ_B at 5 K.

Fig. 5.2 plots the order parameter data for the structural and magnetic phase transitions. The onset of the structural transition is indicated by the initial drop in the $(220)_T$ peak intensity with temperature, which is observed to be around 153 K (Fig. 5.2a). Fig. 5.2b reveals that the Pr Neel temperature is about 14 K while the Fe Neel temperature is

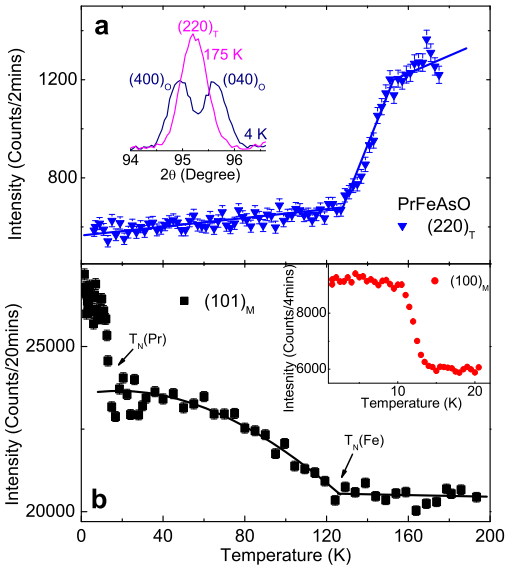

Figure 5.2: Temperature dependence of $(2,2,0)_T$ nuclear Bragg peak and magnetic $(1,0,0)_M$ and $(1,0,1)_M$ peaks. The data in a) and b) are collected on BT-1 and HB-3, respectively. a) Temperature dependence of the $(2,2,0)_T$ (T denotes tetragonal) nuclear Bragg peak showing the onset of the structure phase transition is about 153 K. The inset shows the $(2,2,0)_T$ reflection above and below the transition temperature. b) Temperature dependence of the order parameter for the $(1,0,1)_M$ (M denotes Magnetic) magnetic Bragg peak. The large increase of the intensity below 14 K is due to Pr ordering, as confirmed by the temperature dependence of the $(0,0,1)_M$ magnetic Bragg peak, which has only an intensity contribution from Pr. The intensity of the $(1,0,1)_M$ peak vanishes at the Neel temperature 127 K for the iron spin ordering.

about 127 K. Compared to the undoped PrFeAsO system, there is no observable orthorhombic structure distortion in the $PrFeAsO_{0.85}F_{0.15}$ down to 5 K (Fig. 5.3a). The tetragonal P4/nmm structure can describe the diffraction pattern very well, as is the case for all the other highly doped FeAs-based superconductors. The oxygen-deficient $PrFeAsO_{0.85}$ sample (Fig. 5.3b) also has no orthorhombic structural distortion down to 5 K, and the refined structural parameters are essentially the same as for the F doped sample (Table 1b, 1c). In addition, neither $PrFeAsO_{0.85}F_{0.15}$ nor $PrFeAsO_{0.85}$ has any observable magnetic order at 5 K, suggesting that antiferromagnetic order is directly competing with superconductivity.

Refined structural parameters of $PrFeAsO_{1-x}F_x$ with $x = 0$ at 175 K, $x = 0.15$ at 5 K and $PrFeAsO_{0.85}$ at 5 K. Space group: P4/nmm. PrFeAsO, a = 3.97716(5), c=8.6057(2)Å;

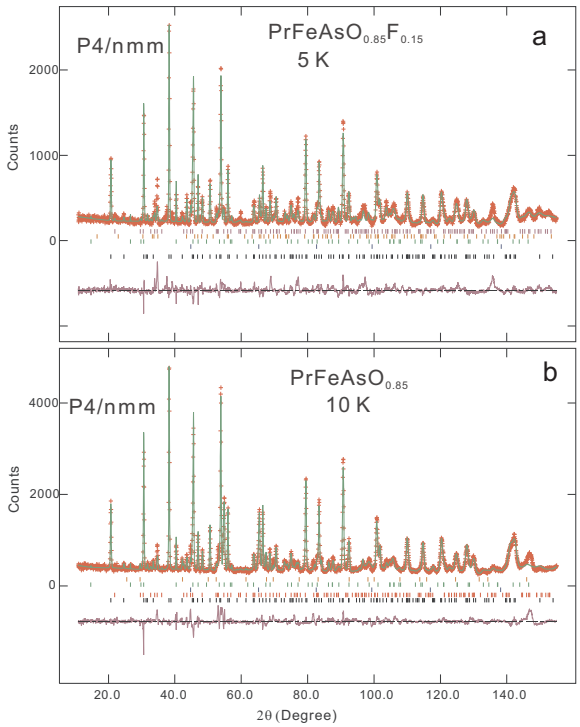

Figure 5.3: Structural diffraction data for the $PrFeAsO_{0.85}F_{0.15}$ and $PrFeAsO_{0.85}$ superconducting samples. The data were collected on the BT-1 diffractometer. a) Observed (crosses) and calculated (solid line) neutron diffraction intensities of $PrFeAsO_{0.85}F_{0.15}$ at 5 K for the tetragonal structure (space group P4/nmm). The short vertical lines show the Bragg peak positions. The (purple/grey) trace indicates the intensity difference between the observed and calculated structures. b) Observed (crosses) and calculated (solid line) neutron diffraction intensities of $PrFeAsO_{0.85}$ at 5 K, refined with the tetragonal space group P4/nmm.

$PrFeAsO_{0.85}F_{0.15}$, a = 3.9700(1), c = 8.5331(4) Å; $PrFeAsO_{0.85}$, a = 3.9686(1), c =8.5365(3)Å

Atom	site	x	y	z(PrFeAsO)	z($PrFeAsO_{0.85}F_{0.15}$)	z($PrFeAsO_{0.85}$)
Pr	2*c*	$\frac{1}{4}$	$\frac{1}{4}$	0.1397(6)	0.1504(1)	0.1450(7)
Fe	2*b*	$\frac{3}{4}$	$\frac{1}{4}$	$\frac{1}{2}$	$\frac{1}{2}$	$\frac{1}{2}$
As	2*c*	$\frac{1}{4}$	$\frac{1}{4}$	0.6559(4)	0.6548(5)	0.6546(5)
O	2*a*	$\frac{3}{4}$	$\frac{1}{4}$	0	0	0

PrFeAsO, Rp =4.55%, wRp = 5.8%, $\chi^2 = 0.387$; $PrFeAsO_{0.85}F_{0.15}$, Rp =8.24%, wRp = 10.62%, $\chi^2 = 3.635$. $PrFeAsO_{0.85}$, Rp =6.99%, wRp = 9.23%, $\chi^2 = 4.652$

5.3 Conclusions

To summarize, we have carried out detailed neutron scattering studies of the magnetic and nuclear structures of the FeAs-based superconductors $PrFeAsO_{0.85}F_{0.15}$ (T_c = 52 K), and $PrFeAsO_{0.85}$ (T_c = 52 K), along with their parent compound PrFeAsO. Very similar to the other parent compounds of FeAs-based superconductors, PrFeAsO has a simple stripe-type antiferromagnetic structure of the iron spins, with a Neel temperature of 127 K and an ordered moment of 0.48(9) μ_B. The magnetic moments on the Pr sites are also antiferromagnetically ordered below 14 K, similar to the parent compounds of the other rare earth FeAs-based superconductors such as CeFeAsO [106] and NdFeAsO [88]. The iron magnetic order occurs below the transition from the high temperature tetragonal phase to the low temperature orthorhombic phase of the parent compound that occurs around 153 K. The structural distortion and iron antiferromagnetic order are suppressed completely in the optimally doped superconducting samples, regardless of whether the superconducting state is achieved by F doping or oxygen vacancies, and the two types of doping yield very similar crystallographic structures.

Chapter 6

Magnetic and Lattice Structures of $SrFe_2As_2$

6.1 Introduction and motivation

Understanding the structural, electronic, and magnetic properties of parent compounds of high-transition temperature (high-T_c) superconductors is an essential step in developing a microscopic theory for superconductivity. In the case of the newly discovered Fe-As based high-T_c superconductors [8–10, 74, 75, 95, 104], Although the Fe ions in parent compounds LaFeAsO (ref. [12, 107]), CeFeAsO (ref. [106]), $BaFe_2As_2$ (refs. [108, 113]) and PrFeAsO (Chapter 5 ref. [87] are found to exhibit commensurate static AFM long range order, all these neutron scattering experiments on these FeAs-based materials were carried out on polycrystalline samples [11, 12, 107, 108, 113] where it was not possible to determine the spin direction, or in most cases the AFM ordering wave vector.

We studied the structural and magnetic phase transitions for $SrFe_2As_2$, the parent compound of the (Sr,K)Fe_2As_2 superconductors [104,118]. Previous transport, 57Fe Mossbauer, and X-ray diffraction experiments [82, 115, 116] have shown that $SrFe_2As_2$ exhibits structural and magnetic phase transitions at 203 K, where the crystal structure changes abruptly from tetragonal (I4/mmm) to orthorhombic (Fmmm). Our neutron scattering experiments confirm the findings of the x-ray measurements for the structural transition, while we are able to determine conclusively that the Fe spins in $SrFe_2As_2$ order antiferro-

magnetically along the orthorhombic a-axis and ferromagnetically along the b-axis, with the moment direction along the a-axis (Figs. 6.1a and 1b). These measurements, together with the recent discovery of static long-range AFM order of the Fe sublattice in NdFeAsO (ref. [88]), suggest that the collinear AFM order shown in Fig. 6.1b is ubiquitous for the parent compounds of the FeAs-based superconductors.

6.2 Magnetic and lattice structures of $SrFe_2As_2$

The $SrFe_2As_2$ crystals grown using the method described in Ref. [117]. Our neutron scattering experiments were carried out on the conventional triple-axis spectrometer BT-9 at the NIST Center for Neutron Research, Gaithersburg, Maryland. The neutron wavelength employed was = 2.359 Åusing a pyrolytic graphite (PG) monochromator, and PG filter to suppress higher-order reflections to achieve a monochromatic incident beam. The collimations were 40 -47 -S-40 -80 . We denote positions in momentum space using Q = (H, K, L) in reciprocal lattice units (r.l.u.) in which Q (in $Å^{-1}$) = (H$2\pi/a$, $K2\pi/b$, $L2\pi/c$), where a = 5.5695(9), b = 5.512(1), c = 12.298(1) Åare lattice parameters in the orthorhombic state at 150 K. The sample ($5 \times 5 \times 0.5$ mm^3, mosaic $\sim 0.3^\circ$ was mounted on an aluminum plate and aligned in the [H, 0, L] zone inside a sealed aluminum container with helium exchange gas and mounted on the cold finger of a closed cycle helium refrigerator.

Figs. 6.1a and 6.1b summarize our experiments, which show the Fe spin arrangements with respect to the orthorhombic low temperature crystal structure. To obtain integrated magnetic intensities necessary for comparison with magnetic structure factor calculations, we carried out radial ($\theta : 2\theta$) as well as rocking (θ) scans for a series of magnetic (1, 0, L) and (3, 0, L) peaks, where L = 1, 3, 5,...Figs. 6.1c and 1d show scans for the (1,0,1) and (1,0,3) peaks below and above the AFM ordering temperature. Sharp, resolution-limited magnetic peaks are observed at 10 K, and completely disappear at 250 K, consistent with establishment of long-range AFM order. A detailed investigation of the low-temperature magnetic Bragg peaks in the (H, 0, L) zone revealed an ordered magnetic structure of Fe ions consistent with previous results on LaFeAsO (ref. [12]), CeFeAsO (ref. [106]), NdFeAsO (ref. [88]) and $BaFe_2As_2$ (ref. [108]). In previous X-ray and neutron diffraction work on $BaFe_2As_2$ and $SrFe_2As_2$, it was found that structural distortion occurs almost

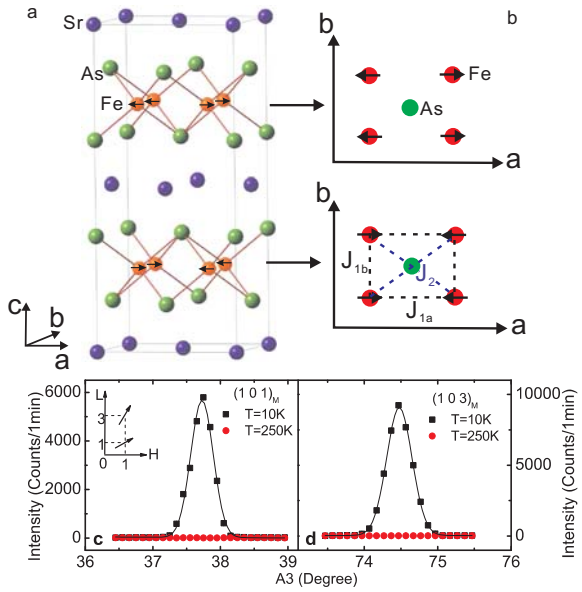

Figure 6.1: Crystal and magnetic structures of $SrFe_2As_2$. a) The three dimensional antiferromagnetic structures of Fe in $SrFe_2As_2$ as determined from our neutron diffraction data. b) The in-plane magnetic structure of Fe in the orthorhombic unit cell of $SrFe_2As_2$. The Fe moments are along the a-axis and form an AFM collinear structure along the a-axis direction and ferromagnetic along the b-axis direction, while nearest-neighbor Fe spins along the c-axis are anti-parallel, identical to that of LaFeAsO (ref. [12]),. J_{1a}, J_{1b}, and J_2 indicate the effective exchange couplings. c,d) Radial scans through the magnetic (1, 0, 1) and (1, 0, 3) magnetic Bragg peaks below and above the Neel temperature, showing clear resolution-limited magnetic peaks.

simultaneously with AFM order [82, 108, 113, 115, 116, 118]. To confirm this in our single crystal of $SrFe_2As_2$, we carried out neutron diffraction measurements focusing on the $(2, 2, 0)_T$ nuclear Bragg peak, where T denotes the high temperature tetragonal phase. As a function of decreasing temperature, the $(2, 2, 0)_T$ peak abruptly splits into the $(4, 0, 0)_O$ and $(0, 4, 0)_O$ Bragg peaks below 220 ± 1 K as shown in Fig. 6.2. Here the subscript O denotes orthorhombic symmetry and the observation of both $(4, 0, 0)_O$ and $(0, 4, 0)_O$ peaks indicates that our single crystal has equally populated twin domains in the orthorhombic phase. Fig. 6.2b compares the structural phase transition and magnetic order parameter in detail as a function of temperature. It is evident that the structural transition occurs more abruptly compared to the magnetic phase transition. By normalizing magnetic peaks with nuclear structural peaks using the magnetic structure shown in Figs. 6.1a and 1b, we estimate that the ground state ordered iron moment is approximately 0.94(4) μ_B at 10 K, where numbers in parentheses indicate one standard deviation statistical uncertainty in the last decimal place and μ_B denotes Bohr magneton.

In previous neutron diffraction work on powder samples of LaFeAsO (ref. [12]), CeFeAsO (ref. [106]), NdFeAsO (ref. [88]) and $BaFe_2As_2$ (ref. [108]), it was found that the Fe spins order antiferromagnetically along one axis of the low-temperature orthorhombic structure and ferromagnetically along the other axis. However, the actual AFM and ferromagnetic ordering directions, as well as the Fe moment direction, were not determined. To determine the direction of the AFM ordering in $SrFe_2As_2$, we carefully probed the (3, 0, 3) magnetic Bragg reflection. Fig. 6.3a shows a radial scan for the magnetic scattering, where we only observed a single (magnetic) peak. Removing the PG filter allows both (6, 0, 6) and (0, 6, 6) orthorhombic nuclear Bragg peaks to be observed via $\lambda/2$ in the incident beam. We see that the magnetic peak corresponds to the smaller diffraction angle, which establishes that the AFM ordering is along the a-axis. A further check is provided in Fig. 6.3b, where the diffraction angle was set to the higher angle reflection and rocking curves were performed, with and without the PG filter. The only peak observed is the (0, 6, 6) nuclear reflection, when the filter was removed. This demonstrates that the only magnetic reflection is the (3, 0, 3) peak. Therefore, our experiments conclusively identify the AFM ordering direction as along the long a-axis direction of the orthorhombic $SrFe_2As_2$ unit cell.

To determine the Fe moment direction, we carried out integrated intensity measure-

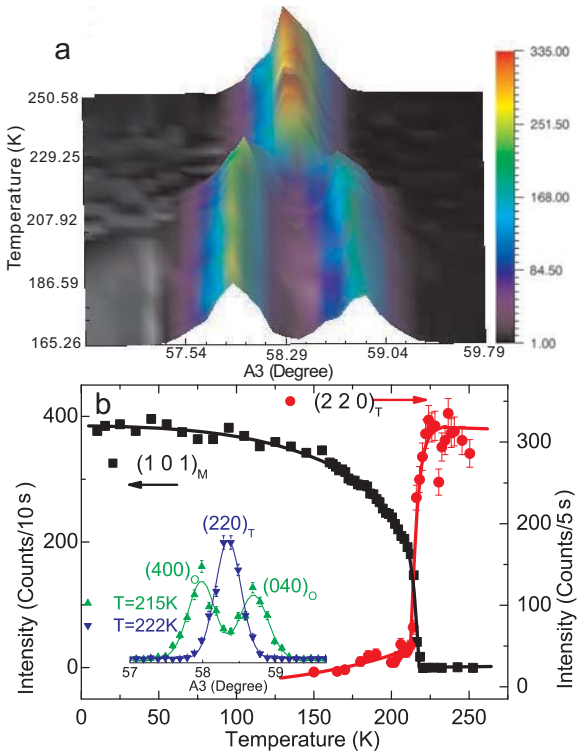

Figure 6.2: Structural and magnetic phase transition as a function of temperature in single crystal $SrFe_2As_2$. a) Temperature dependence of the $(2, 2, 0)_T$ structural peak, showing that it abruptly splits below 220 ± 1 K . The data were collected using 10 -10.7 -S-10 -80 collimation. b) Comparison of structural distortion and magnetic order parameter, both occurring at essentially the same temperature. The structural transition is first order, while the magnetic transition appears to be continuous.

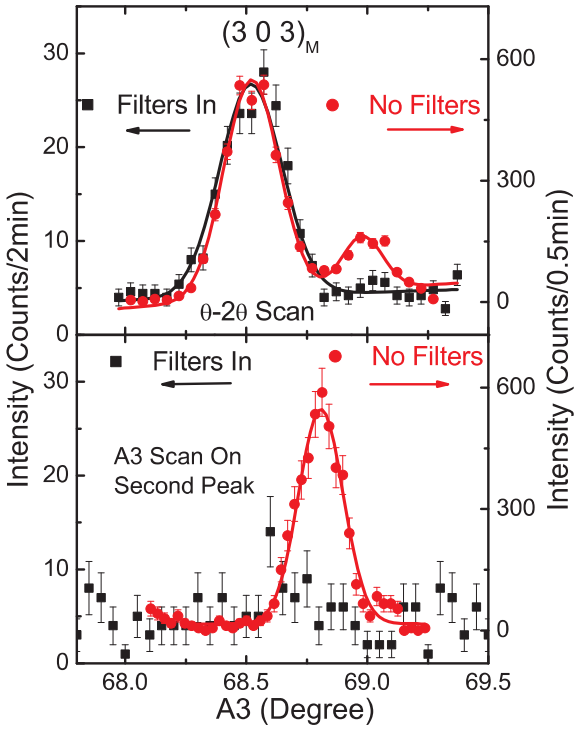

Figure 6.3: Rocking curves of the (3, 0, 3) magnetic Bragg peak and its comparison with structural Bragg peaks obtained from $\lambda/2$ of the nuclear (6, 0, 6) and (0, 6, 6) reflections. b) Identical rocking curve for (0, 3, 3) magnetic peak position showing no magnetic scattering. This provides definitive evidence that the AFM order occurs along the a-axis direction.

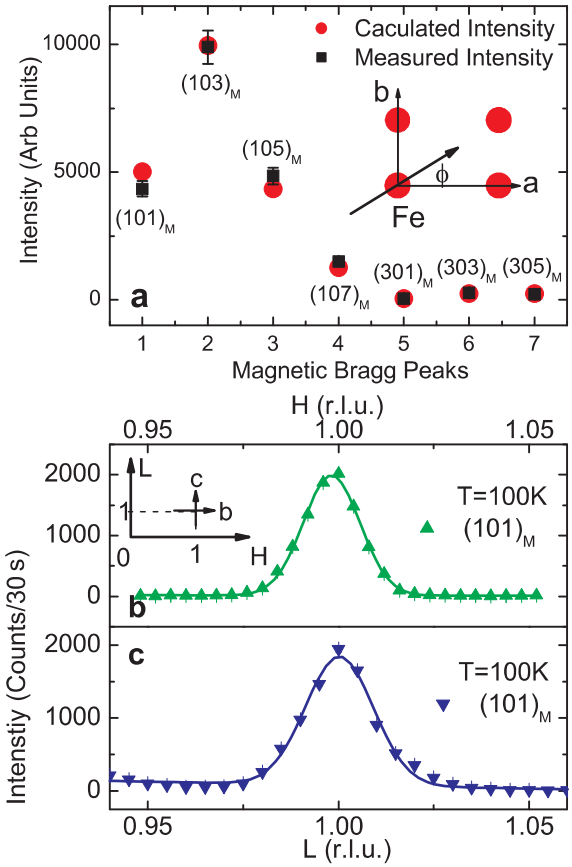

Figure 6.4: Calculated and observed integrated magnetic Bragg peak intensities for Fe spin direction along the a-axis. The agreement is excellent, demonstrating that the moment direction is along a. ϕ is the angle between Fe spin direction and a-axis, which was found to be close to zero for the best fit of the experimental data. b,c) resolution-limited [H, 0, 1] and [1, 0, L] scans through the (1, 0, 1) magnetic Bragg peak, indicating that the order in long range in nature with a minimum correlation length of 330 Å.

ments for a serious of magnetic Bragg reflections. Group symmetry analysis performed in the low temperature Fmmm phase restricts the moments to be either along the a-axis, b-axis, or c-axis, assuming that the magnetic transition is second order; if it is first order then there are no restrictions on the spin direction. However, if the dominant interactions are determined by Fe-As-Fe exchange, then the orthorhombic structure dictates that the diagonal exchange J_2 in Fig. 6.1b should be the same for both diagonal directions since the bond angles and distances are identical. Therefore we expect the Fe spins in $SrFe_2As_2$ to point either along the a-axis or along the b-axis, and this is indeed the case. Assuming the Fe spin direction is ϕ away from the a-axis (inset in Fig. 6.4a), the least square fit of our magnetic structure factor calculations indicates excellent agreement with a $\chi^2 = 3.8$ for moment along the a-axis ($\phi = 4 \pm 3^\circ$). Therefore, it is clear that the moment direction is along a, and the spin structure is as shown in Figs. 6.1a and 6.1b. The collinear antiferromagnetic structure can be described in an effective $J_1 - J_2 - J_z$ Heisenberg model [77,78,94], where J_1 and J_2 are the antiferromagnetic exchange couplings between the nearest neighbor and second nearest neighbor Fe atoms, respectively, and J_z is the exchange coupling between FeAs layers (Fig. 6.1b). When $J_1 < 2J_2$, the model has a collinear antiferromagnetic ground state and also an Ising nematic order state at high temperature which can couple to the structure transition in the general Ginzburg-Landau approach. When J_z/J_2 is larger than 0.005, the collinear magnetic and Ising nematic transition temperatures are very close [77]. In this model, by including the coupling between the Ising order and the lattice, the structure transition is expected to happen at the same transition temperature as that of the collinear magnetic transition, which is a good description of the current case in $SrFe_2As_2$, where the inter-layer coupling is much larger than that in RFeAsO compounds.

6.3 Exchange couplings in $SrFe_2As_2$

The observed configuration of orthorhombic lattice distortion and the corresponding spin arrangement reveals that the nearest neighbor AFM exchange coupling J_1 is not a simple result of a superexchange interaction arising from electron hopping through the As ion, since this requires $J_{1a} > J_1 > J_{1b}$ after the lattice distortion in order to save total energy [94]. The fact that the ferromagnetic exchange is along the short (b) axis of the orthorhombic

structure suggests the presence of a significant direct ferromagnetic exchange coupling. That is, $J_1 = {J_1}^s - {J_1}^d$ where ${J_1}^s$ is the superexchange AFM contribution and ${J_1}^d$ is the ferromagnetic part from direct Fe-Fe exchange. The small lattice distortion has little effect on the local onsite energy, but can directly change the electron hopping amplitude. Assume that the high-temperature in-plane tetragonal lattice constant a_T is split into orthorhombic $a = a_T + \delta$ and $b = a_T - \delta$. Then the change of the distance between Fe and the nearest neighbor As is given by the leading order $\delta^2/4$(Fig. 6.1b). Therefore, the change in the hopping amplitude t' after lattice distortion is $\Delta t' \propto \delta^2$. Since the superexchange ${J_1}^s \propto t'^4$, its changes after the lattice distortion should be $\Delta {J_1}^s \propto -\delta^2$. This means that the reduction in ${J_1}^s$ is a second order effect of the lattice distortion. On the other hand, since the direct ferromagnetic exchange ${J_1}^d$ is proportional to the hopping amplitude t, the leading order changes of ${J_1}^d$ along the a- and b-axes after the lattice distortion should be ${J_{1a}}^d \propto -\delta$ and ${J_{1b}}^d \propto \delta$ respectively. Therefore, J_1 increases along the a-axis and decreases along the b-axis after the lattice distortion. In FeAs-based materials, the AFM order is rapidly suppressed upon doping. This immediately suggests a decrease of J_{1a} with increasing doping. Since the decrease of J_{1a} mostly arises from the increase of the direct exchange ${J_{1a}}^d$, the long (a) axis of the orthorhombic structure is expected to be suppressed with increasing electron or hole doping. This phenomenon has indeed been observed in electron-doped CeFeAsO, where the long (a) axis of the orthorhombic structure is reduced upon doping F while the short (b) axis is unaffected (see Fig. 6.3 of ref. [106]). Therefore, to obtain a comprehensive understanding of the mechanism of superconductivity in these FeAs-based superconductors, one must consider both the direct- and super-exchange interactions and their relationship to lattice distortion effects.

6.4 Conclusions

In summary, we have determined the AFM ordering wave vector and spin direction in $SrFe_2As_2$, the parent compound of the (Sr,K)Fe_2As_2 superconductors. Since recent neutron scattering and μSR experiments also independently confirmed that the Fe spins in NdFeAsO orders antiferromagnetically with the same spin structure as LaFeAsO (ref. [12]), CeFeAsO (ref. [106]), and $BaFe_2As_2$ (ref. [108]), it is safe to assume that the collinear static

antiferromagnetic structure shown in Fig. 6.1b is ubiquitous for the parent compound of these FeAs-based high-T_c superconductors.

Chapter 7

Spin Waves and Magnetic Interactions in $SrFe_2As_2$

7.1 Introduction and motivation

The parent compounds of the high-transition temperature (high-T_c) copper oxides are simple antiferromagnetic (AF) Mott insulators [70] chatracterized by a very strong nearest neighbor AF exchange coupling J (> 100 meV) in the CuO_2 planes [22]. In the case of Fe based superconductors, the undoped parent compounds are also long-range ordered antiferromagnets with a collinear spin structure as discussed in Chapters 4-6 (Fig. 7.1a) [12, 88, 106–109, 120], much is unknown about the magnetic exchange coupling responsible for such a spin structure. For example, early theoretical studies suggest that LaFeAso has a spin-density-wave (SDW) instability [79, 89]. As a consequence, the AF spin structure in these materials are due to quasiparticle excitations cross electron-hole pockets in a nested Fermi surface [121], much like SDW antiferromagnetism in metallic chromium (Cr) [122]. Alternatively, a Heisenberg magnetic exchange model [77, 94, 123] is suggested to explain the AF structure. Here, the collinear spin phase is stable when the nearest neighbor exchange J_1 and the next nearest neighbor exchange J_2 satisfy $J_1 < 2J_2$ (Fig. 7.1a). First-principle calculations estimate $J_1 \sim J_2$ [123]. In contrast, some band structure calculations [80] suggest that the J_1 along the a-axis and b-axis of the low temperature orthorhombic structure ($c > a > b$) can have different signs with J_{1a} and J_{1b} being AF and ferromagnetic

respectively and that $J_{1a} > 2J_2$. Therefore, there is no theoretical consensus on the relative strengths of J_{1a}, J_{1b}, and J_2 or the microscopic origin of the observed AF spin structure. If magnetism is important for superconductivity of these materials, it is essential to establish the "effective Hamiltonian" that can determine the magnetic exchange coupling.

Here we use inelastic neutron scattering to study the spin wave excitations in single crystals of $SrFe_2As_2$ ($T_N = 220$ K) [109], the parent compound of $Sr_{1-x}K_xFe_2As_2$ superconductors. At low temperature, we find that spin waves have an anisotropy gap below $\Delta = 6.5$ meV and disperse rapidly along both the $[H, 0, 0]$ and $[0, 0, L]$ directions. On warming to 160 K, the magnitude of the spin gap decreases to 3.5 meV and intensity of the spin wave excitations follow bose statistics as expected. However, there is no evidence of critical scattering and magnetic correlations in the paramagnetic state at 240 K, in sharp contrast to the SDW excitations in Cr [122] and spin waves in cuprates [22, 71]. We estimated the effective magnetic exchange coupling using a Heisenberg model and found that $J_{1a} + 2J_2 = 100 \pm 20$ meV, $J_z = 5 \pm 1$ meV, and magnetic single ion anisotropy $J_s = 0.015 \pm 0.005$ meV. The weak critical scattering and paramagnetic spin-spin correlations is much different from SDW excitations in Cr and cuprates, and suggest that the AF phase transition is first order in nature.

7.2 Experimental details

Our experiments were carried out on HB-1 triple-axis spectrometer at the High Flux Isotope Reactor, Oak Ridge National Laboratory, BT-1 and SPINS triple-axis spectrometers at the NIST center for neutron research. For HB-1 and BT-7 measurements, we fixed final neutron energy at $E_f = 14.7$ meV and used PG(0,0,2) (pyrolytic graphite) as monochromators and analyzers. A PG filter was placed in the exit beam path to eliminate $\lambda/2$. For SPINS measurements, the final neutron energy was fixed at $E_f = 5$ meV and a cold Be filter was placed on the exit beam path. $SrFe_2As_2$ single crystals are grown from flux method [104] and were coaligned within 2 degrees to have a total mass of $\sim$0.7 g. From earlier diffraction work [109], we know that AF order occurs at close approximity to a lattice distortion, changing the crystal structural symmetry from tetragonal above T_N to orthorhombic below it (Fig. 7.1b). However, it is unclear whether the structural and magnetic phase

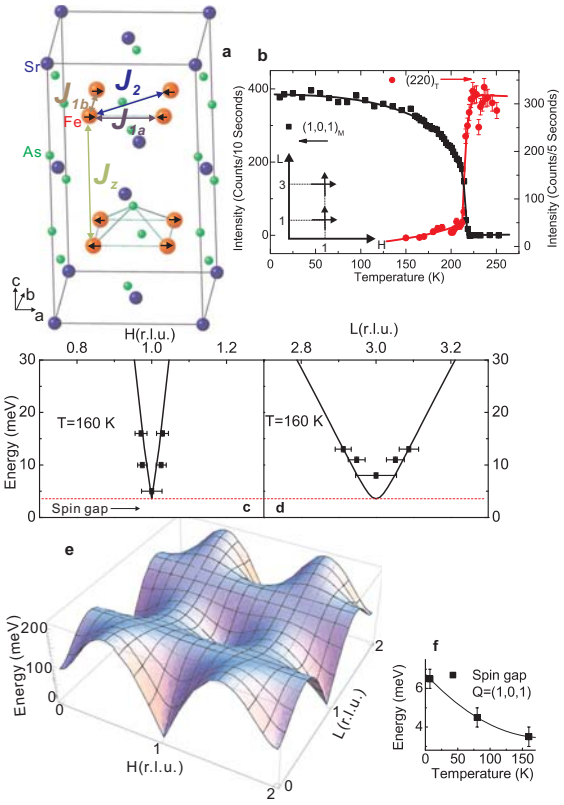

Figure 7.1: (a) The Fe spin ordering in the $SrFe_2As_2$ chemical unit cell and magnetic exchange couplings along different high-symmetry directions. (b) The AF Néel temperature and the temperature dependence of the structural $(2, 2, 0)$ Bragg peak of the $SrFe_2As_2$ crystals used in the experiment [109]. The inset shows positions in reciprocal space probed in the experiment. (c) Observed spin wave dispersion along the $[H, 0, 0]$ direction at 160 K. (d) Similar dispersion along the $[0, 0, L]$ direction. (e) Calculated three-dimensional spin wave dispersions with exchange coupling constants obtained from the best fits to the data. (f) Temperature dependence of the anisotropic spin gap $\Delta(T)$.

transitions are second [82] or first order [124]. For the observed spin structure (Fig. 7.1a), magnetic Bragg peaks are allowed at $[H, 0, L]$ ($H = 1, 3$ and $L = 1, 3, 5,$) reciprocal lattice units (r.l.u), where momentum transfer is $Q(\text{in } \text{Å}^{-1}) = (H2\pi/a, K2\pi/b, L2\pi/c)$ and $a = 5.5695(9)$, $b = 5.512(1)$, $c = 12.298(1)$ Å are lattice parameters in the orthorhombic state at 150 K. To probe spin wave excitations, we aligned our single crystals in the $[H, 0, L]$ zone, where we can probe excitations along the $[H, 0, 0]$ and $[0, 0, L]$ directions.

7.3 Spin wave dispersions and spin gaps

Figs. 7.2a and 2e show constant-energy scans for $\hbar\omega = 1$ and 5 meV around $[H, 0, 1]$ at 160 K obtained on SPINS. While the scattering at $\hbar\omega = 1$ meV is featureless (Fig. 7.2a), there is a clear peak centered at $H = 1$ in the 5 meV data (Fig. 7.2e). This immediately suggests that spin waves in $SrFe_2As_2$ have an anisotropy gap that is less than 5 meV. Moving on to higher energies, Figs. 7.2b-d and 7.2f-h summarize Q-scans along $[H, 0, 0]$ and $[0, 0, L]$ directions, respectively, at different energies. The Q-widths of the scattering clearly become broader with increasing energy. Figs. 7.1c and 1d show the observed dispersion curves for the limited energy range with observable spin wave excitations. Assuming an effective Heisenberg Hamiltonian [77,125] $H = J_{1a}\sum_{i,j}\mathbf{S}_i\cdot\mathbf{S}_j + J_{1b}\sum_{i,j}\mathbf{S}_i\cdot\mathbf{S}_j + J_2\sum_{i,j}\mathbf{S}_i\cdot\mathbf{S}_j + J_z\mathbf{S}_i\cdot\mathbf{S}_j - J_s(S_i^z)^2$, where J_{1a}, J_{1b}, J_2, and J_z are exchange interactions shown in Fig. 7.1a; J_s is the single ion anisotropy; and S is the magnitude of iron spin, spin wave dispersions along the $[H, 0, 0]$ and $[0, 0, L]$ directions near the $(1, 0, 1)$ Bragg peak are $E(k_x) = 2S[(J_{1a}+2J_2+J_s+J_z)^2-(J_z-(J_{1a}+2J_2)\cos k_x)^2]^{1/2}$ and $E(k_z) = 2S[(2J_{1a}+4J_2+J_s+J_z-J_z\cos k_z)(J_s+J_z+J_z\cos kz)]^{1/2}$, respectively. In addition, the size of the spin gap due to the single ion anisotropy is $\Delta(1, 0, 1) = 2S[J_s(2J_{1a} + 4J_2 + J_s + 2J_z)]^{1/2}$. The solid lines in Figs. 7.1c and 1d are the best fits with these equations, where $J_{1a} + 2J_2 = 100 \pm 20$ meV, $J_z = 5 \pm 1$ meV, and $J_s = 0.015 \pm 0.005$ meV. The three-dimensional plot in Fig. 7.1e shows the expected spin wave dispersion at higher energies. To see temperature dependence of the spin gap, we carried out energy scans at the signal and background positions for spin waves at different temperatures. At 7 K, energy scan at the signal position $Q = (1, 0, 1)$ shows an abrupt increase above 6.5 meV, while background scattering at $Q = (1.2, 0, 1)$ is featureless (Fig. 7.3a). Energy scans at equivalent positions $Q = (1, 0, 3)$ and $(0.8, 0, 3)$ in Fig. 7.3b show similar results and therefore revealing a low temperature spin gap with $\Delta = 6.5$ meV. On warming to 80 K, identical scans at $Q = (1, 0, 1)$ and $Q = (1.2, 0, 1)$ shows that the spin gap is now at $\Delta = 4.5$ meV (Fig. 7.3c). Finally, Δ becomes 3.5 meV at 160 K, consistent with constant-energy scans in Figs. 7.2a and 2e. These results indicate that the spin anisotropy of the system reduces with increasing temperature.

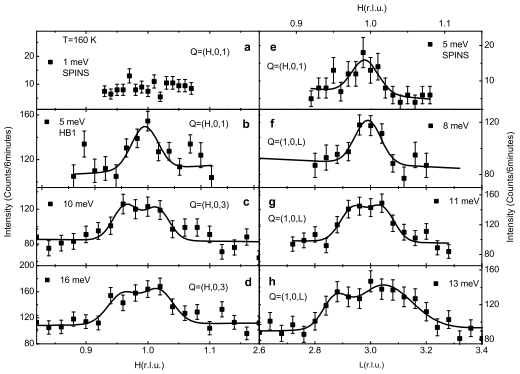

Figure 7.2: Wavevector dependence of the spin wave excitations at 160 K obtained on cold [(a) and (e)] and thermal [(b)-(d) and (f)-(h)] triple-axis spectrometers at different energies. (a) Q-scan along the $[H, 0, 1]$ direction at $\hbar\omega = 1$ meV using SPINS. The spectrum is featureless indicating the presence of a 1 meV spin gap. Identical scan at $\hbar\omega = 5$ meV in (e) shows clear evidence of spin wave excitations centered at $(1, 0, 1)$. (b-d) Q-scans along the $[H, 0, 1]$ or $[H, 0, 3]$ directions at different energies. The spectra clearly broadens with increasing energy. (f-h) Similar scans along the $[1, 0, L]$ direction, which probes the exchange coupling J_z.

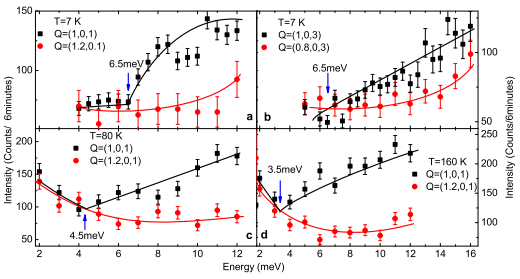

Figure 7.3: Temperature dependence of the spin-gap obtained from energy scans around the (1,0,1) and (1,0,3) Bragg peaks. (a) Low temperature ($T = 7$ K) constant-Q scans at the signal ($Q = (1, 0, 1)$) and background ($Q = (1.2, 0, 1)$) positions show a clear spin-gap at $\Delta = 6.5$ meV (b) Similar scans at $Q = (1, 0, 3)$ and $Q = (0.8, 0, 3)$ which again shows $\Delta = 6.5$ meV. (c),(d) Temperature dependence of the spin-gap, where $\Delta = 4.5$ meV at 80 K and $\Delta = 3.5$ meV at 160 K

7.4 Quasielastic scattering below and above T_N

Fig. 7.4 summarizes the temperature dependence of the spin waves and quasielastic scattering in the AF ordered and paramagnetic states obtained on SPINS and BT-7. Fig. 7.4a shows energy scans at $Q = (1, 0, 1)$ for $T = 130, 160, 200, 240,$ and 280 K plotted in log scale. When temperature is increased across T_N (= 220 K), there is a rapid decrease in the ordered moment but little evidence for quasielastic and critical scattering, which are signatures of a second order phase transition. To illustrate this point, we plot in Fig. 7.4b the temperature difference scattering using 280 K data as background. Besides the magnetic order peak below T_N at $\hbar\omega = 0$ meV, there is no evidence of quasielastic critical scattering typical of a second order phase transition. Figs. 7.4c shows constant-energy scans ($\hbar\omega = 1$ meV) measured on SPINS and the scattering is essentially featureless at all temperatures investigated, thus suggesting weak spin-spin correlations in the paramagnetic state. Thermal triple-axis measurements at $\hbar\omega = 10$ meV in the paramagnetic state reveal similar results. Assuming paramagnetic scattering is uncorrelated at 280 K, the differences in the scattering between 240 K and 280 K should reveal the magnetic intensity gain close to T_N. Consistent with temperature dependence of the energy scans in Figs. 7.4a and 7.4b, there are signs of possible uncorrelated paramagnetic scattering (since the subtracted data in Fig. 7.4e are overall positive) at 240 K but no evidence for critical scattering. For temperatures below T_N, we find that spin wave excitations at temperatures below 160 K simply follow the Bose statistics (Fig. 7.4f) and decrease on approaching T_N.

7.5 Discussion and conclusions

The discovery of the collinear AF order with small moment in LaFeAsO [12] has caused much debate about its microscopic origin. Since LaFeAsO is a semimetal, the observed AF order may arise from a SDW instability due to nested Fermi surface [79, 89, 121], where electron itinerancy is important much like incommensurate SDW order in pure metal Cr [122]. Alternatively, there are reasons to believe that LaFeAsO is in proximity to a Mott insulator [76], and the AF order is a signature of local physics and electron correlations [77, 78]. Another heavily debated issue is the first [124] or second [82] order

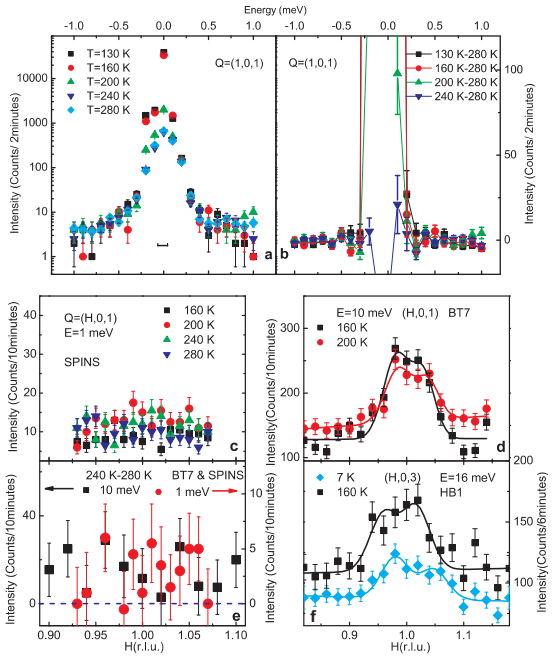

Figure 7.4: Temperature dependence of the quasi-elastic magnetic scattering and spin wave excitations below and above T_N. Data in (a)-(c) are obtained on SPINS. (a) Constant-Q scans at $Q = (1, 0, 1)$ Bragg peak position at different temperatures. Except for the dramatic increase below T_N, the quasi-elastic scattering above $\hbar\omega = 0.5$ meV is essentially temperature independent, revealing no evidence for the Lorentzian-like paramagnetic scattering above T_N observed in Cr [122]. (b) Temperature difference spectra using $T = 280$ K scattering as background, the data again show no evidence of critical scattering, suggesting a first order AF phase transition. (c) Q-scans at $\hbar\omega = 1$ meV at different temperatures. No spin-spin correlations are found at probed temperatures. We speculate that the slight increase in overall scattering at 240 K from 280 K shown in (e) is due to uncorrelated paramagnetic scattering. (d) $\hbar\omega = 10$ meV spin-wave excitations at 160 K and 200 K obtained on BT-7. (f) $\hbar\omega = 16$ meV spin-wave excitations at 7 K and 160 obtained on HB-1. The intensity increase is due to the Bose population factor.

nature of the simultaneous structural/magnetic phase transition in $SrFe_2As_2$.

If the observed AF order in $SrFe_2As_2$ originates from Fermi surface nesting similar to the SDW order in Cr, the velocity of the spin waves c should be $c = \sqrt{v_e v_h/3}$, where v_e and v_h are the electron and hole Fermi veloclities, respectively [122]. The dispersion relation is then $\hbar\omega = cq$ where q is the magnitude of the momentum transfer away from the Bragg position. For Cr, the spin-wave velocity is measured to be $c = 851 \pm 98$ meVÅ [122]. In addition, there are strong spin-spin correlations in the paramagnetic state where the dynamic structure factor $S(q, \hbar\omega)$ can be described by the product of a Gaussian centered at the SDW ordering wavevector and a Lorentzian in energy or $S(q, \hbar\omega) = S_0(T)e^{-\xi/2\sigma^2}(\hbar\omega/k_BT)/[((\hbar\omega)^2 + \Gamma)(1 - e^{-\hbar\omega/k_BT})]$, where σ and Γ are the Gaussian and Lorentzian width, respectively [122]. At temperatures as high as 500 K ($T = 1.6T_N$), one can observe a clear resolution-broadened Lorentzian centered at $\hbar\omega = 0$ meV with $\Gamma = 15.6$ meV [122]. For comparison, there is no evidence of a Lorentzian-like paramagnetic scattering in $SrFe_2As_2$ even at $T = 1.09T_N$. The lack of critical scattering both below and above T_N, together with the fact that there is also a strong structural distortion occuring at the same temperature [82,124], suggest that the AF phase transition is first order in nature.

To compare the observed exchange coupling in Fig. 7.1 and those expected from SDW excitations in a nested Fermi surface, we note that Fermi velocities estimated from the local density approximation calculations for $BaFe_2As_2$ [126] are $v_e = 2.2$ eVÅ and $v_h = 1.2$ eVÅ. Assuming $BaFe_2As_2$ and $SrFe_2As_2$ have similar Fermi velocities, the expected spin wave velocity is then $c \sim 0.94$ eVÅ. However, since Angle Resolved Photoemission spectroscopy (ARPES) experiments on $BaFe_2As_2$ [127] show that the band width is strongly renormalized, the larger Fermi velocities in electron and hole pockets are $v_e \approx v_h \sim 0.5$ eVÅ. These values would give $c \sim 0.29$ eVÅ. Using smaller Fermi velocities would yield half of the larger values or $c \sim 0.15$ eVÅ. Within the local moment effective $J_{1a} - J_{1b} - J_2$ model, the spin wave velocity is given by $c = 2.8(J_{1a} + J_2)$ eVÅ. From our measured $J_{1a} + 2J_2 = 100 \pm 20$ meV, $c \sim 0.28$ eVÅ which is fairly close to the ARPES results. Therefore, our present data do not allow an unambiguous distinction between localized and itinerant description of the AF order in $SrFe_2As_2$ in terms of the spin wave velocity.

In summary, we carried inelastic neutron scattering experiments to study low energy spin wave excitations in $SrFe_2As_2$. The low-temperature spectrum consists of a Bragg peak,

a spin gap, and sharp spin wave excitations at higher energies. Using a simple Heisenberg Hamiltonian, we find $J_{1a}+2J_2 = 100\pm20$ meV, $J_z = 5\pm1$ meV, and $J_s = 0.015\pm0.005$ meV. On warming cross T_N, there is no evidence of critical scattering and spin-spin correlations in the paramagnetic state, different from the paramagnetic SDW excitations in Cr. These results suggest that the AF phase transition in $SrFe_2As_2$ is first order in nature.

Chapter 8

Spin Waves and Magnetic Exchange Interactions in $CaFe_2As_2$

8.1 Introduction and motivation

In Chapter 7 we showed that the low energy spin wave excitations of $SrFe_2As_2$ can be fitted with an effective Heisenberg Hamiltonian. However, because only spin excitations below 30 meV were probed and therefore it is still unclear whether magnetism is derived from excitations of conduction electrons [89,128–131] or from localized moments [77,78,81, 133,134]. More importantly, in spite of intensive effort [135–139], there is no consensus as to the simplest "effective ground state Hamiltonian" in the parent compound of Fe based superconductors. A determination of the effective magnetic exchange coupling and ground state Hamiltonian in the parent compounds of these materials is important because such an understanding will provide the basis against which superconductivity-induced changes can be identified. Using inelastic neutron scattering, we have measured the dispersion of spin-wave excitations in $CaFe_2As_2$ (refs. [120, 140]), one of the parent compounds of the Fe based superconductors, and determined the effective magnetic exchange interactions. If the static long-range AF order depicted in Fig. 8.1a for the parent compounds of Fe based superconductors originates from a collective spin-density-wave order instability of itinerant electrons like in chromium, the velocity of spin wave excitations c should be $c = (v_e v_h/3)^{1/2}$, where v_e and v_h are the electron and hole Fermi velocity, respectively [122].

Furthermore, spin wave excitations should exhibit longitudinal and transverse polarization, and damp into single particle excitations (Stoner continuum) via transfer of an electron (spin) from the majority to the minority band at high energies as shown schematically in Fig. 8.1c (ref. [132]). On the other hand, if magnetic order in iron pnictides has a local moment origin as in the parent compounds of the copper oxides, one should observe well-defined (essentially instrumental resolution limited) spin waves throughout the Brillouin zone and magnetic coupling between local moments should be dominated by direct and super-exchange interactions (Fig. 8.1d) [77, 78, 81, 133, 134]. Although the presence of itinerant magnetic excitations and Stoner continuum have been suggested in $BaFe_2As_2$ (ref. [138]) and $CaFe_2As_2$ (ref. [139]), these measurements were carry out at energies well below the zone boundary spin wave energy (200 meV) and therefore were unable to conclusively determine the effective magnetic exchange interactions and life time of the spin waves.

8.2 Spin wave dispersions and local susceptibility

We used inelastic neutron scattering to study low-temperature (T = 10 K) spin waves of single crystals of $CaFe_2As_2$ which has a Neel temperature of $T_N \approx 170$ K (refs. [120, 140]). Figs. 8.1e-l shows two-dimensional constant-energy (-E) images of spin-wave excitations of $CaFe_2As_2$ around the AF zone center in the (H, K) scattering plane [135–139]. Previous low-energy measurements [137] revealed that spin waves in $CaFe_2As_2$ are three-dimensional and centered at AF wave vector Q = (1,0, L = 1, 3, 5,...) reciprocal lattice units (rlu). For energy transfers of $E = 48 \pm 6$ (Fig. 8.1e) and 65 ± 4 meV (Fig. 8.1f), spin waves are still peaked at Q = (1,0,) rlu in the center of the Brillouin zone (shown as dashed square boxes). As energy increases to E = 100 ± 10 (Fig. 8.1g), 115 ± 10 (Fig. 8.1h), 137.5 ± 15 (Fig. 8.1i), 135 ± 10 (Fig. 8.1j), and 145 ± 15 meV (Fig. 8.1k), counter-propagating spin-wave modes become apparent. The scattering changes to ellipses elongated along the K-direction for energies above 100 meV (Figs. 8.1h-1k). For an energy transfer of 175 ± 15 meV (Fig. 8.1l), spin waves show a broad square-like scattering already reaching the zone boundary in the K-direction. To quantitatively determine the spin-wave dispersion, we cut through the two-dimensional images similar to Fig. 8.1 for various incident beam energies (Ei) aligned

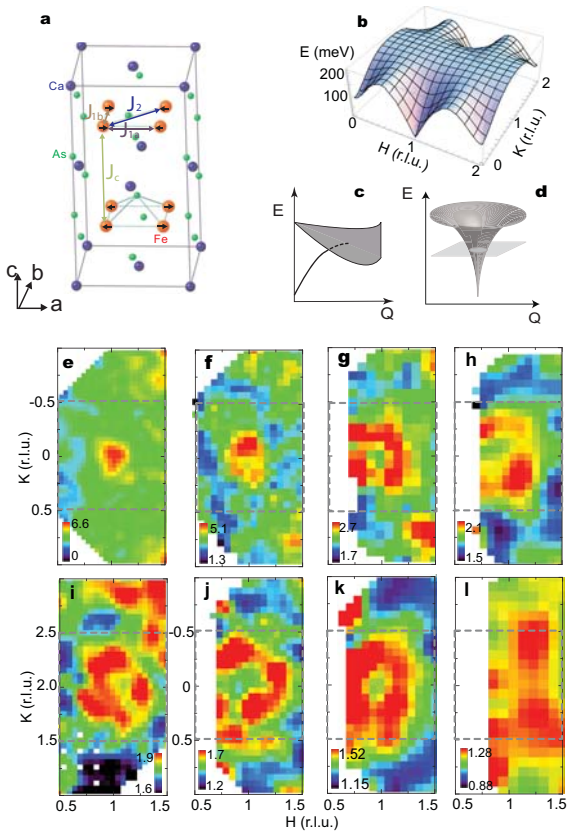

Figure 8.1: Magnetic structure, calculated spin-wave dispersion and wave vector dependence of spin-wave excitations at different energies for $CaFe_2As_2$. Our inelastic neutron scattering experiments were carried out on the MERLIN time-of-flight chopper spectrometer at the Rutherford-Appleton Laboratory, Didcot, UK. We co-aligned 6.4 grams of single crystals of $CaFe_2As_2$ grown by self flux method (with in-plane mosaic of 2 degrees and out-of-plane mosaic of 3 degrees). The incident beam energies were Ei = 50, 80 150, 200, 250, 450, 600 meV, and mostly with Ei parallel to the c axis. Spin wave intensities were normalized to absolute units using a vanadium standard (with 30% error). We define the wave vector Q at (q_x,q_y,q_z) as $(H,K,L) = (q_x 2\pi/a, q_y 2\pi/b, q_z 2\pi/c)$, where a = 5.506, b = 5.450, and c = 11.664 Åare the orthorhombic cell lattice parameters at 10 K (ref. [120]). a) Schematic diagram of the Fe spin ordering in $CaFe_2As_2$. b) Calculated three-dimensional spin-wave dispersions using $SJ_{1a} = 49.9$ $SJ_{1b} = -5.7$, $SJ_2 = 18.9$, $SJ_c = 5.3$ meV c) Schematic diagrams for how spin-wave dispersion enters into Stoner continuum. d) Dispersion of spin waves in a classical Heisenberg Hamiltonian. Wave vector dependence of the spin waves for energy transfers of e) 48 ± 6 meV [$E_i = 150$ meV and Q=(1,0,3)]; f)$E = 65 \pm 4$ meV [$Ei = 250$ meV and Q=(1,0,3)]; g) 100 ± 10 meV [$E_i = 450$ meV and Q=(1,0,3.5)]; h) 115 ± 10 meV [$E_i = 450$ meV and Q=(1,0,3.5)]; i) 137 ± 15 meV [$E_i = 600$ meV and Q=(1,2,4)]; j) 135 ± 10 meV [$E_i = 450$ meV and Q=(1,0,4.5)]; k) 144 ± 15 meV [$E_i = 450$ meV and Q=(1,0,5)]; l) 175 ± 15 meV [$E_i = 600$ meV and Q=(1,0,5.2)].

along the c-axis. Figs. 8.2a-g show the outcome for different spin-wave energies in the form of constant-E scans along the K-direction around the AF zone center. As the excitation energy increases from 25 meV (Fig. 8.2g) to 144.5 meV (Fig. 8.2a), well-defined counter-propagating spin waves approach the zone boundary. To illustrate the general feature of the high-energy spin waves, we have used the scattering near (2,0,0) rlu as a background and assumed the positive scattering at wave vectors below (2,0,0) rlu is entirely magnetic. Fig. 9.3a shows the outcome of the background subtracted scattering for the Ei = 450 meV data projected in the wave vector (Q = [1,K]) and energy space. In spite of the spin wave intensity modulation along the L-direction due to the exchange interaction J_c between the FeAs planes [137] (Fig. 8.1a), one can see three clear plumes of scattering arising from the in-plane AF zone centers Q = (1,-2), (1,0), and (1,2) rlu. The spin-wave scattering disperses for energies above 100 meV and extends up to about 200 meV. Since spin waves become less dispersive as the zone boundary is approached, we locate the spin wave excitations via energy scans at a fixed wave vector. Figs. 8.3c-h summarize a series of such scans at different wave vectors which reveal clear dispersions near the zone boundary and a maximum spin-wave bandwidth of about 200 meV. In addition to the results presented in Figs. 8.1-3, we have also collected similar data at other wave vectors throughout the Brillouin zone. The solid circles in Figs. 8.4a-c summarize our measured spin wave dispersions along the [H,0,1], [1,0,L], and [1,K,1] directions. To understand these data as well as the wave vector-energy (Q-E) dependence of the spin-wave intensities, we consider a Heisenberg Hamiltonian consisting of effective in-plane nearest-neighbors (Fig. 8.1a, J_{1a} and J_{1b}), next-nearest-neighbor (Fig. 8.1a, J_2), and out-of-plane (Fig. 8.1a, J_c) exchange interactions. The dispersion relations are given by [135–139]:

$$E(\vec{Q}) = \sqrt{A_{\vec{Q}}^2 - {B_{\vec{Q}}}^2}, \tag{8.1}$$

where

$$A_{\vec{Q}} = 2S[J_{1b}(cos(\pi K) - 1) + J_{1a} + J_c + 2J_2 + J_s] \tag{8.2}$$

$$B_{\vec{Q}} = 2S[J_{1a}cos(\pi H) + 2J_2cos(\pi H)cos(\pi K) + J_ccos(\pi L)] \tag{8.3}$$

J_s is the single ion anisotropy constant, and $\vec{Q}$ is wave vector. The neutron scattering cross section can be written as [136]:

$$\frac{\mathrm{d}^2\sigma}{\mathrm{d}\Omega \mathrm{d}E_\mathrm{f}} = \frac{\vec{k_\mathrm{f}}}{\vec{k_\mathrm{i}}} \left(\frac{\gamma r_0}{2}\right)^2 g^2 f^2(\vec{Q}) \exp(-2W) \times \sum_{\alpha\beta} (\delta_{\alpha\beta} - \hat{Q}_\alpha \hat{Q}_\beta) S^{\alpha\beta}(\vec{Q}, E), \tag{8.4}$$

where $(\gamma r_0/2)^2 = 72.65\,\mathrm{mb}$, g is the g-factor (≈ 2) , $f(\vec{Q})$ the magnetic form factor of iron, $\exp(-2W)$ is the Debye–Waller factor(≈ 1 at 10 K), $\hat{Q}_\alpha$ is the α component of a unit vector in the direction of $\vec{Q}$, $S^{\alpha\beta}(\vec{Q}, E)$ is the response function that describes the $\alpha\beta$ spin-spin correlations, and $\vec{k_i}$ and $\vec{k_f}$ are incident and final wave vectors, respectively. Assuming that only the transverse correlations contribute to the spin-wave cross section and finite excitation lifetimes can be described by a damped simple harmonic oscillator with inverse lifetime Γ (refs. [141, 142]), we have

$$S^{yy}(\vec{Q}, E) = S^{zz}(\vec{Q}, E) = S_{eff} \frac{A_{\vec{Q}} - B_{\vec{Q}}}{E_0(1 - e^{k_B T})} \frac{4}{\pi} \frac{\Gamma E E_0}{(E^2 - {E_{\vec{Q}}}^2 + 4(\Gamma E)^2} \tag{8.5}$$

where k_B is the Boltzmann constant, E_0 is the spin-wave energy, and S_{eff} is the effective spin. We analyzed our data by keeping S and distinct following the practice of Ref. [136]. We fitted the measured absolute intensity of spin wave excitations and their dispersions in Figs. 8.1-4 by convoluting the above discussed neutron scattering spin-wave cross section with the instrument resolution using Tobyfit program [141, 142]. Since $CaFe_2As_2$ exhibits tetragonal to orthorhombic lattice distortion below the T_N (refs. [120]), care was taken to include the (H,K)/(K,H) twin domains in the computed scattering cross section. We find that the Heisenberg Hamiltonian with only the nearest-neighbors effective exchange couplings (J_{1a} and J_{1b} are finite, and $J_2 = 0$) cannot explain the data. Theoretically, it has been argued that the observed collinear spin structure in Fig. 8.1a is consistent with either $SJ_{1a} \approx SJ_{1b} \approx 1/2SJ_2$ or $SJ_{1a} \approx 2SJ_2 \gg SJ_{1b}$. Distinguishing these two models require spin-wave data near the zone boundary [131]. Although previous neutron scattering experiments on $CaFe_2As_2$ suggest $SJ_{1a} \approx SJ_{1b} \approx 25 \pm 8$,$SJ_2 = 36 \pm 2$, and $SJ_c = 7 \pm 1$

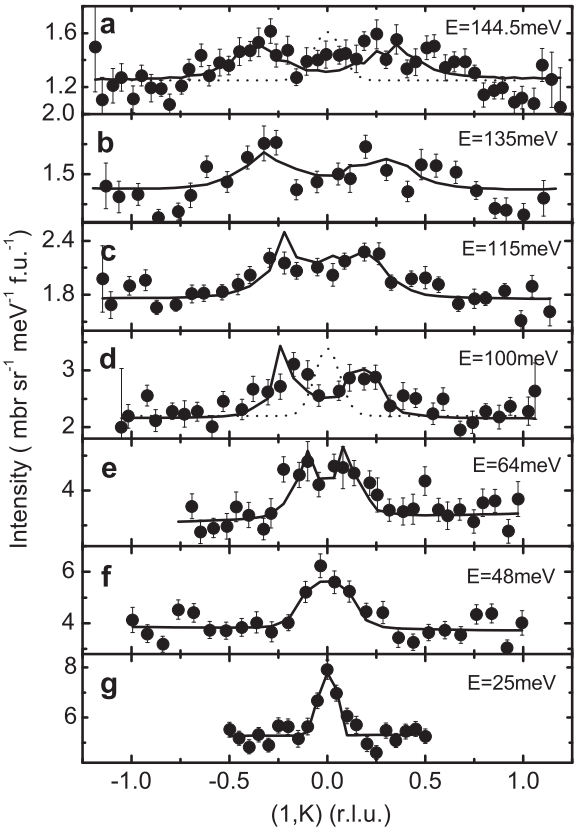

Figure 8.2: Constant energy cuts of the spin-wave dispersion as a function of increasing energy and our model fit using the Heisenberg Hamiltonian. A series of constant-energy cuts through the AF spin-wave zone center as a function of decreasing energy a)$E = 144 \pm 20$; b)$E = 135 \pm 10$; c)$E = 115 \pm 15$; d)$E = 100 \pm 10$; e)$E = 65 \pm 10$; f)$E = 48 \pm 6$; g)$E = 25 \pm 5$ meV. The solid lines are model fits to the data after convoluting the cross section to the instrumental resolution. Typical instrumental resolutions are shown as dotted lines in (a) and (d).

meV (refs. [137, 139]), these results are obtained by fitting spin-wave data well below the 200 meV zone boundary energy (Fig. 8.3) and therefore are inconclusive.

The red dashed lines in Figs. 8.3f-h show the expected zone boundary spin waves assuming $SJ_{1a} = 27$,$SJ_{1b} = 25$,$SJ_2 = 36$and $SJ_c = 5.3$ meV. It is obvious that such a model failed to describe the zone boundary data. Our best fits to both the low-energy and zone boundary spin waves by independently varying the effective exchange parameters are shown as solid black lines in Figs. 8.2 and 3 with $SJ_{1a} = 49.9 \pm 9.9$, $SJ_{1b} = -5.7 \pm 4.5$, $SJ_2 = 18.9 \pm 3.4$, $SJ_c = 5.3 \pm 1.3$ meV. The broadening of the spin waves with increasing energy is accounted for via $\Gamma \propto 0.15E$ and shown as dotted lines in Fig. 8.4. From our

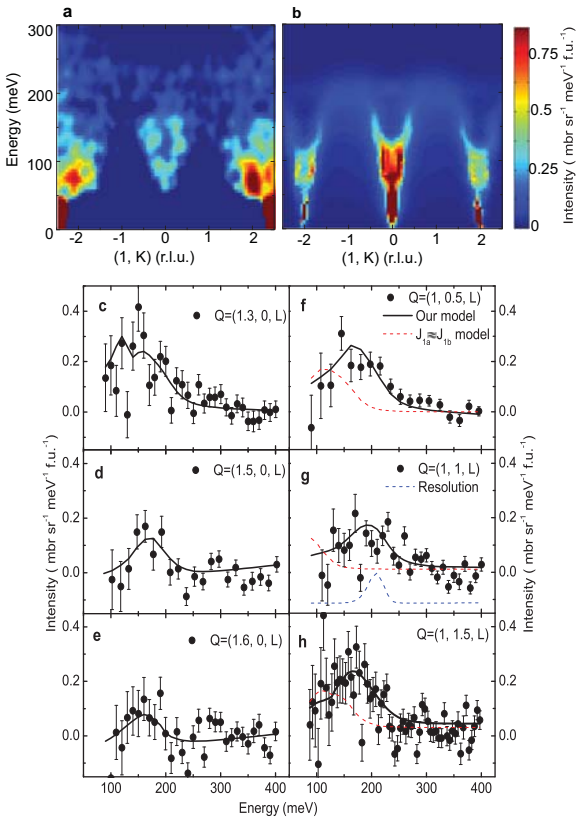

Figure 8.3: Observed and calculated spin waves at 10 K, and constant-Q cuts near the AF zone boundary. a) The projections are in the scattering plane formed by the energy transfer axis and (1,K) direction (with integration of H from 0.8 to 1.2 rlu) after subtracting the background integrated from $1.8 < H < 2.2$ and $-0.25 < K < 0.25$. $E_i = 450$ meV b) Calculated spin wave excitations using model specified in the text. c-h) Constant-Q cuts at various wave vectors near the zone boundary. $E_i = 600$ meV The solid ($J_{1a} > 0$,$J_{1b} < 0$) and dashed ($J_{1a} \approx J_{1b}$) lines are our models fits to the data

best fit to all spin wave data, we find $S_{eff} = 0.22 \pm 0.06$ which is somewhat smaller than previous measurements on powder samples of $BaFe_2As_2$ (ref. [136]). The value of S_{eff} and the measured 0.8 μ_B/Fe static moment [120] suggest of a $S \approx 1/2$ system. Theoretically, if we consider a spin 1/2 quantum Heisenberg model with the above exchange parameters, a simple calculation reveals elastic moment $= g(S - \delta S)\mu_B = 2(1/2 - 0.09)\mu_B = 0.82\mu_B$, where δS is the spin wave correction to the magnetic moment in quantum Heisenberg model [143], and $S_{eff} = Z_d S = 0.285$, where $Z_d = 0.57$ is an intensity-lowering renormalization factor of the one magnon cross section due to quantum fluctuations and magnon-magnon interactions [143].

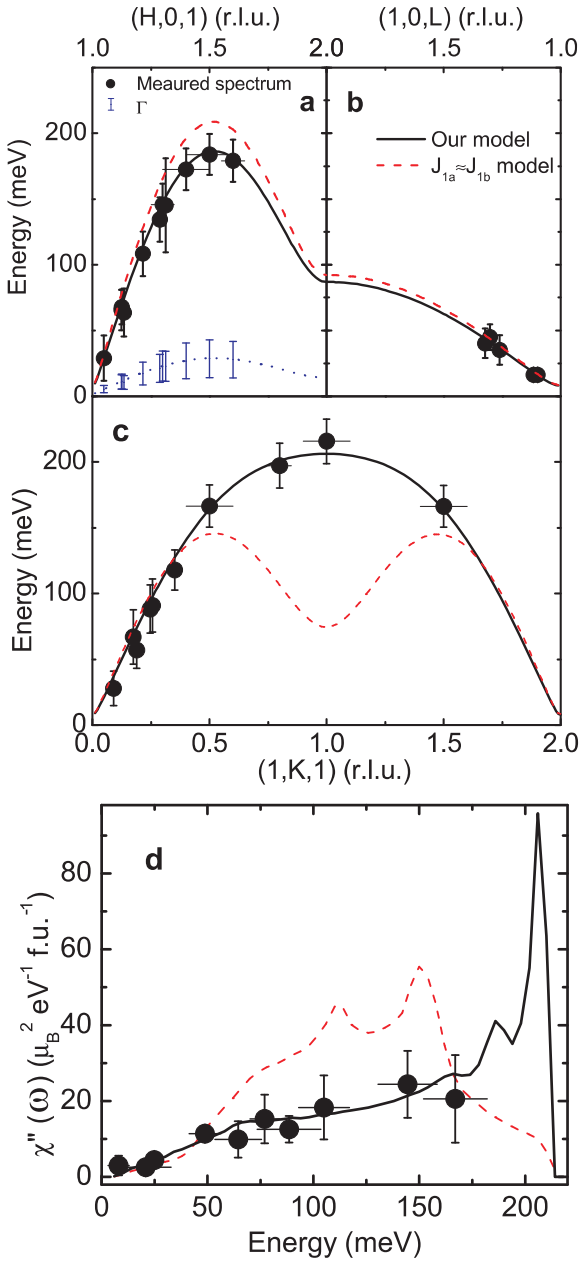

Figure 8.4: Spin-wave dispersion relation along high symmetry directions in the three-dimensional Brillouin zone and energy dependence of the local susceptibility. The solid circles in Figs. 8.a-c) are extracted from constant-E(-Q) cuts of various Ei data. The horizontal bars indicate the E(Q) integration range and vertical bars are errors calculated from least square fittings. Solid (dashed) lines are fits to spin-wave models discussed in the text. The lengths of the blue vertical bars indicate wave vector dependence of Γ, the$\Gamma/E \approx 0.15$ is much smaller than metallic ferromagnet $La_{2-2x}Sr_{1+2x}Mn_2O_7$ where (ref. [142]), thus suggesting smaller influence of itinerant electrons in $CaFe_2As_2$. The blue dotted line is guide to the eye. d) Energy dependence of the local susceptibility obtained by integrating raw intensities above background from $0.5 < H < 1.5$; $-0.5 < K < 0.5$; $L - 0.5 < L < L + 0.5$, where $L = 1, 3, 5$ in the (1,0,L) zone. Twinning effect has not been taken out. In our experiment set up, the energy, magnetic form factor, and the polarization factors are all weakly dependent within the Brillouin zone. For simplicity, we used appropriate values for these factors at the zone center Q=(1,0,L). Solid and dashed lines are expected energy dependence of the local susceptibility for the two models discussed in the text.

From fitting results in Figs. 8.2-4, we see that the spin wave dispersion and intensity in $CaFe_2As_2$ throughout the Brillouin zone can be well described by a Heisenberg Hamiltonian with effective nearest-neighbors and next-nearest neighbor exchange interactions. Figs. 8.4a-c summarize the spin-wave dispersions along all three high symmetry directions and Fig. 8.4d shows energy-dependence of the local susceptibility [21], together with calculations using $SJ_{1a} \approx SJ_{1b}$ (red dashed lines) or our models (solid lines). The former model clearly fails to describe the data. To test whether the spin-wave branch crosses the Stoner continuum as schematically illustrated in Fig. 8.1c, we plot spin-wave damping Γ versus E as dotted lines in Figs. 8.4a-c. Although Γ is approximately proportional to $0.15E$, there is no steep increase in Γ at any wave vector indicative of a Stoner continuum (Fig. 8.1c). Instead, the observed spin-wave broadening at high energies may arise from magnon-electron scattering due to the low-temperature metallic nature of the system, similar to ferromagnetic metallic manganites [141, 142].

8.3 Conclusions

The central message of our work is that one can fit spin waves of $CaFe_2As_2$ throughout the Brillouin zone with a simple Heisenberg Hamiltonian without the need for Stoner continuum- the hall mark of an itinerant electron system. The lack of direct evidence for a Stoner continuum below 200 meV suggests weak low energy electron-hole particle excitations. This is consistent with optical measurements, where 80% of the charge carriers are gapped out below T_N (ref. [144]) and therefore do not contribute to the low-energy electron-hole excitations. One local density approximation calculation has predicted essentially the correct in-plane magnetic exchange couplings [130], these results, however, are obtained within the tetragonal and collinear AF ordered structures contrary to the experiments. Furthermore, band structure calculations suggest that the Fermi velocity a/b anisotropy in $CaFe_2As_2$ is less than 8% in the low temperature orthorhombic phase (D. J. Singh, private communication). If spin-wave velocities in $CaFe_2As_2$ are proportional to $(v_e v_h/3)^{1/2}$ as those in chromium [122], they should be similar along the a/b directions. Although our results appear to favor a localized moment picture, a spin 1/2 model cannot be produced if all orbitals in iron are localized since there are even numbers of electrons per

iron. Moreover, it is difficult to understand why direct and super-exchange interactions within the Fe-As-Fe plane are so different along the a/b directions of the orthorhombic structure because the tetragonal to orthorhombic lattice distortion below T_N is small and only weakly affects the Fe-As-Fe bond distances/angles [12, 106]. The observed large difference may hint the involvement of other electronic degree of freedoms, such as orbital, in the magnetic transition. To achieve a comprehensive understanding of spin excitations, one must consider both the localized and itinerant electrons in these materials.

Chapter 9

Magnetic Field Effect on the Resonance Mode in $BaFe_{1.9}Ni_{0.1}As_2$

9.1 Introduction and motivation

The proximity of high-T_c superconductivity near antiferromagnetism in Fe based superconductors raised the possibility of a magnons mediated pairing mechansim [12, 75, 95, 106, 121, 145–147]. The high energy scale (200 meV) spin dynamics of their parent compounds also suggests the antiferromagnetism is a possible candidate for the driving force of the high T_c superconductivity. Actually soon after the discovery of superconductivity in $LaFeAsO_{1-x}F_x$ (ref. [95]), band-structure calculations for these materials find two hole cylinders around the Γ point and two electron cylinders around the M point. In theories of spin fluctuation mediated superconductivity [58, 79, 121, 145–147, 158, 159], electron pairing arises from quasiparticle excitations from the hole pocket to electron pocket (inset in Fig. 9.1c). While the normal-state spin excitations are dominated by the continuum of scattering, superconductivity arising from sign reversed interband scattering induces a resonance peak at the antiferromagnetic (AF) ordering wave vector Q = (0.5,0.5) in the spin excitations spectrum (Fig. 9.1b), whose energy should be at (or slightly less than) the addition of hole and electron superconducting gap energies ($\hbar\omega = |\Delta(k+Q)| + |\Delta(k)|$) refs. [58, 79, 158–160]. Although the resonance and its temperature dependence observed by inelastic neutron scattering in $Ba_{0.6}K_{0.4}Fe_2As_2$ (ref. [152]), $BaFe_{2-x}(Co,Ni)_xAs_2$

(refs. [152, 153, 155, 156]) are consistent with this picture, there have been no direct proof that the resonance energy is related to superconducting energy gap and therefore it is still unclear whether the mode is related to electron pairing. One way to resolve this problem is to study the effect of a magnetic field on superconductivity and spin excitations. A magnetic field can suppress T_c and reduce the magnitude of the superconducting energy gap via either orbital pair breaking of Cooper pairs in the superconducting state or Pauli paramagnetism due to Zeeman effect on electron spins. If the resonance is associated with quasiparticle excitations across the electron and hole [121, 145–147], application of a magnetic field that suppress the superconducting gaps should also reduce the energy of the resonance. We find this is indeed the case for $BaFe_{1.9}Ni_{0.1}As_2$ (Fig. 9.1), and our results thus provide the most compelling evidence that electron pairing in iron arsenide superconductors is directly correlated with magnetic excitations.

9.2 Experimental details and conclusions

In the undoped state, the parent compounds of iron arsenide superconductors are non-superconducting antiferromagnets with a spin structure as shown Fig. 9.1a (refs. [12,106]). Upon doping to induce optimal superconductivity, the static AF order is suppressed and low-energy magnetic excitations in the superconducting state are dominated by a spin gap and resonance above the spin gap energy [58,79,158–160]. For optimally electron-doped superconductor $BaFe_{1.9}Ni_{0.1}As_2$ with $T_c = 20$ K (Fig. 9.1c), the resonance occurs near$\hbar\omega \approx 8$ meV at Q = (0.5,0.5,0) reciprocal lattice unit (rlu) above $\hbar\omega \approx 3$ meV spin gap in the low temperature superconducting state [154, 155]. We used inelastic neutron scattering to study the effect of a 14.5-Tesla c-axis aligned magnetic field on the resonance and spin gap (Fig. 9.1). At zero field, energy scans in the normal state (T = 25 K) show clear gapless continuum of scattering at the signal Q = (0.5,0.5,0) position above the background Q = (0.62,0.62,0) (red filled and open circles in Fig. 9.1d). On cooling into the superconducting state (T = 2 K), a spin gap opens below$\hbar\omega \approx 3$ meV and the low energy spectral weight is transferred into the resonance at $\hbar\omega \approx 8$ meV (refs. [154,155]). While imposition of a 14.5-T magnetic field along the c-axis has little effect on the background (Fig. 9.1d) and normal state scattering at Q = (0.5,0.5,0) (not shown for clarity purpose), the resonance peak in

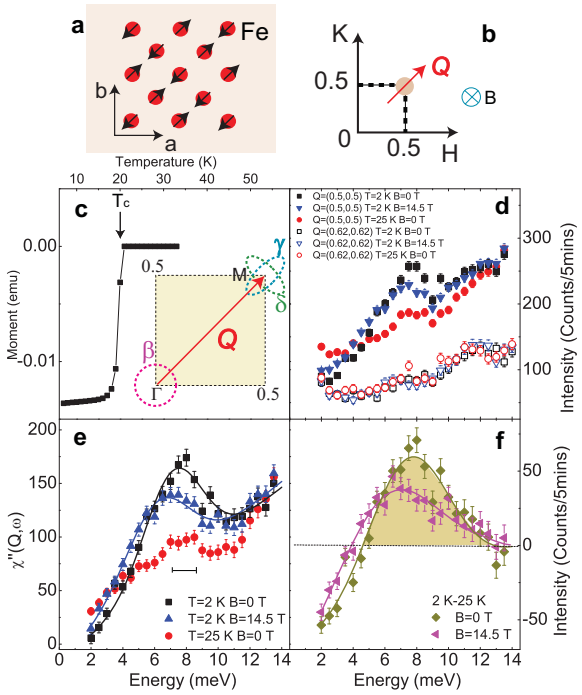

Figure 9.1: Magnetic structure, probed reciprocal lattice space and magnetic field dependence of the scattering at the antiferromagnetic wavevector for $BaFe_{1.9}Ni_{0.1}As_2$. Our inelastic neutron scattering experiments were carried out on the IN-22 thermal triple-axis spectrometer at the Institut Laue-Langevin, Grenoble, France. We co-aligned 5.5 grams of single crystals of $BaFe_{1.9}Ni_{0.1}As_2$ grown by self-flux (with in-plane mosaic of 2 degrees). We define the wave vector Q at (q_x,q_y,q_z) as $(H, K, L) = (q_x 2\pi/a, q_y 2\pi/b, q_z 2\pi/c)$, where a = b = 3.963, and c = 12.77 Åare the tetragonal unit cell lattice parameters. Our samples are aligned in the (H,K,0) horizontal scattering plane inside a 14.5 T vertical field magnet. The final neutron energy was fixed at 14.7 meV with a pyrolytic graphite filter before the analyzer. Field was always applied in the normal state at 25 K. a) Schematic diagram of the Fe spin ordering in $BaFe_2As_2$. b) Reciprocal space probed and direction of applied field. c) Susceptibility of our sample indicating T_c = 20 K. The inset shows schematic diagram of how the resonance is produced by quasiparticle excitations through the hole and electron pockets. d) Energy scans at the signal Q = (0.5,0.5,0) and background Q = (0.62,0.62,0) rlu positions for various fields and temperatures. The background scattering has negligible temperature and field dependence. e) Temperature and field dependence of χ"(Q, ω) at Q = (0.5,0.5,0). Horizontal bar indicates instrumental energy resolution. f) Difference spectra of the neutron intensity between T = 2 K ($< T_c$) and T = 25 K (T_c+5 K) at Q = (0.5,0.5,0) for B = 0 and a 14.5 T c-axis aligned field. Error bars indicate one sigma.

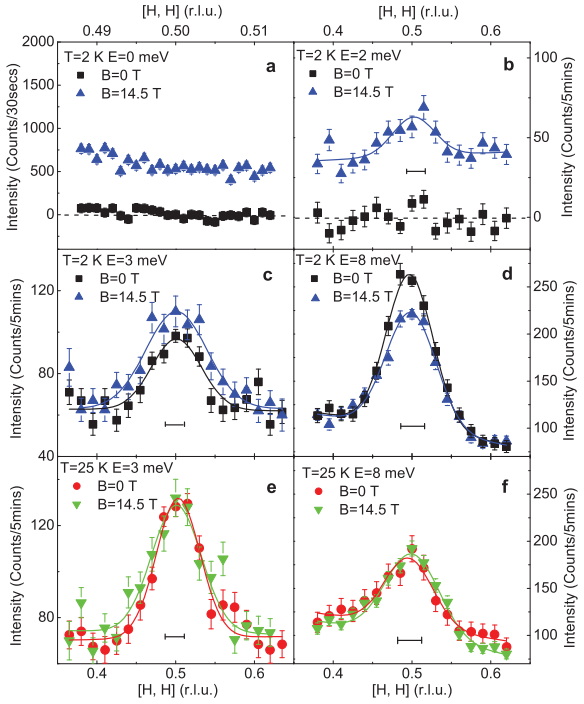

the superconducting state is clearly suppressed and shifted to a lower energy (blue triangles in Fig. 9.1d). Figure 9.1e plots the temperature dependence of the imaginary part of the dynamic susceptibility $\chi"(Q,\omega)$, obtained by subtracting the background scattering and correcting for the Bose population factor $\chi"(Q,\omega) == [1 - exp(-\hbar\omega/((k_BT)))]S(Q,\chi")$, where k_B is the Boltzmann constant. Inspection of the Figure reveals that application of a 14.5-T magnetic field shifted the energy of the resonance from $\hbar\omega \approx 7.3\pm0.15$ meV to 6 ± 0.2 meV, induced about 7% reduction in the integrated intensity of the mode, and broadened the mode only slightly. Comparison of the temperature difference plots at zero and 14.5-T in Fig. 9.4f confirms the shifting energy of the mode and indicates that the field-induced resonance intensity reduction is compensated by intensity gain at lower energies.

Although the constant-Q scans in Fig. 9.1 are excellent ways of determining the influence of a magnetic field on the resonance mode energy and peak intensity, they do not provide inform on how the field affects the momentum distribution of the magnetic excitations (spin-spin correlation function). Figure 9.2 summarizes Q-scans at energies $\hbar\omega = 0, 2, 3, 8$ meV which corresponds to elastic scattering, below and near spin gap energy, and at the resonance energy, respectively. At zero energy transfer ($\hbar\omega = 0$ meV) and

2 K, the scattering across Q = (0.5,0.5,0) are featureless at zero and 14.5-T (Fig. 9.2a), indicating that such a field does not induce AF long range static order. For $\hbar\omega = 2$ meV, the scattering at zero field show no peak consistent with the presence of a spin gap at 2 K. However, the identical Q-scan at 14.5-T shows a clear peak at Q = (0.5,0.5,0), suggesting a field-induced scattering due to the decreasing value of the zero field spin gap (Figs. 9.1e and 2b). Similarly, a 14.5-T field enhances the zero field $\hbar\omega = 3$ meV peak near Q = (0.5,0.5,0) in the superconducting state at 2 K (Fig. 9.2c) but has no effect above T_c at 25 K (Fig. 9.2e). In contrast, imposition of a 14.5-T field at 2 K suppresses the resonance intensity at $\hbar\omega = 8$ meV (Fig. 9.2d) but has no effect in the normal state at 25 K (Fig. 9.2f). Fourier transforms of the Gaussian peaks at $\hbar\omega = 8$ meV and 2 K in Fig. 9.2d give spin-spin correlation lengths of $\xi = 57 \pm 2$ Åand $\xi = 53 \pm 3$ Åfor 0 and 14.5-T, respectively. Therefore, a field can change the energy and intensity of the resonance, but has small effect on spin-spin correlation length much like the magnetic field effect on underdoped copper oxide superconductor $YBa_2Cu_3O_{6.6}$ (ref. [161]).

Figure 9.3 compares temperature dependence of the scattering at Q = (0.5,0.5,0) for $\hbar\omega = 2$ and 8 meV at zero and 14.5-T, respectively. Consistent with previous work [154, 155], we find that magnetic scattering at Q = (0.5,0.5,0) open a spin gap below T_c at $\hbar\omega = 2$ meV and display a superconducting order parameter-like increase for $\hbar\omega = 8$ meV (Figs. 9.3a and 3c). Upon application of a 14.5-T field, the kink in the zero field temperature dependence data at $\hbar\omega$ =2 meV indicative of the opening of the spin gap disappears (Fig. 9.3b). Instead, the scattering show no observable anomaly in the probed temperature range. On the other hand, temperature dependence of the scattering at the resonance energy ($\hbar\omega = 8$ meV) shows a clearly depressed Tc of $\sim$ 16 K at 14.5-T from $T_c = 20$ K at zero field (Figs. 9.3c and 3d). Since an applied magnetic field that suppresses T_c also decreases the superconducting gap energy, these results demonstrate that the resonance energy and its temperature dependence are directly correlated with the superconducting gap energy and electron pairing strength. Figures 9.4a and 4b show the magnetic field dependence of the scattering at the resonance energy in the superconducting state at 2 K and normal state at 25 K, respectively. While the normal state spin excitations have no observable field effect up to 14.5-T, the scattering at the resonance energy clearly decreases with increasing field. The black line is a linear fit to the data using $I/I_0 = 1 - B/B_{char}$ with

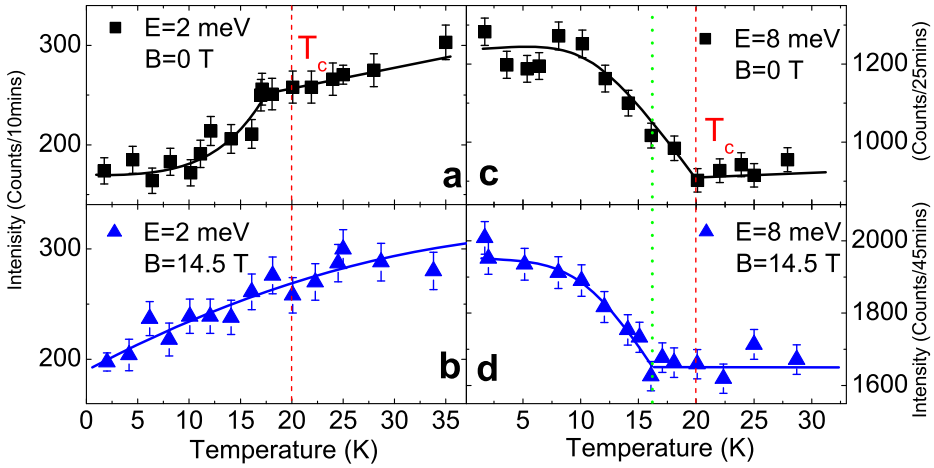

Figure 9.3: Effect of a magnetic field on the temperature dependence of the resonance and low-energy spin excitations at Q = (0.5,0.5,0). a) Temperature dependence of the scattering at $\hbar\omega = 2$ meV and zero field shows the opening of a spin gap slightly below Tc consistent with refs. 15,16. b) The same temperature dependence at 14.5T. The kink is gone. c) Temperature dependence of the scattering at the resonance energy of $\hbar\omega = 8$ meV and zero field displays order parameter like intensity increase below $T_c = 20$ K. d) Application of a 14.5-T field suppresses Tc to 16 K. Error bars indicate one sigma.

$B_{char} \approx 32$ T, where intensity of the resonance is suppressed to the normal state value. The dotted line represents a fit assuming $I/I_0 = 1 - (B/B_{char})^{1/2}$, where $B_{char} \approx 66$ T. Since the energy of the resonance is decreasing with increasing field, it is difficult to estimate the characteristic field B_{char} using the field dependent scattering at the resonance energy at zero field and compare with the upper critical field B_{c2}. We note, however, that scanning tunneling spectroscopy and magnetotransport measurements on $BaFe_{1.8}Co_{0.2}As_2$ samples ($T_c \approx 22 - 25.3$ K) showed an upper critical field of ~ 43 T (ref. [162]) and ~ 50 T (ref. [163]), respectively, for a c-axis aligned field. To see whether the total momentum sum rule $\int_{-\infty}^{+\infty} \int dQS(Q,\omega)$ is satisfied within the probed energy-moment space at zero and 14.5-T (ref. [143]), we plot in Figure 9.4c experimentally measured difference spectrum, S(Q,χ" ,B=0 T)-S(Q,χ",B=14.5 T), at Q = (0.5,0.5,0). Within the errors of our measurements, we find that the spectra weight loss of the resonance under a 14.5-T field is compensated by the field-induced subgap intensity gain, suggesting that $\int_{-\infty}^{+\infty} \int dQS(Q,\omega)$ is conserved within the probed Q-energy s In previous work on copper oxide superconductors, application of a magnetic field can suppress the intensity of the resonance [161] and induce AF order at the expense of the resonance [40, 164–167]. However, the energy of the resonance does not change with field [40, 161, 165–167]. Theoretically, several effects of a magnetic field on the resonance and spin excitations have been considered within the random-phase approximation: first, the supercurrents circulating around the field-induced vortices may broaden the resonance in energy without changing its Q-energy integrated weight; second, a field-induced uniform suppression of the superconducting gap magnitude should cause the resonance to shift to lower energy and decrease in intensity; third, the effect of field-induced suppression of the superconducting coherence factor might lead to suppression of the spectral weight and causing the resonance to shift to higher energy; and finally, suppression of the resonance within the filed-induced vortex cores could result in reduced resonance intensity without shifting its position, consistent with neutron scattering results on $YBa_2Cu_3O_{6.6}$ (refs. [161, 168]). Since we observed clear field-induced resonance energy and intensity reduction in $BaFe_{1.9}Ni_{0.1}As_2$ (Figs. 9.1-4), our data are mostly consistent with a field-induced suppression of the superconducting gap energy.

If this microscopic picture is indeed correct, we can use neutron scattering data in Figs. 9.1-4 to estimate the upper critical field B_{c2} and expected resonance energy shift at 14.5-

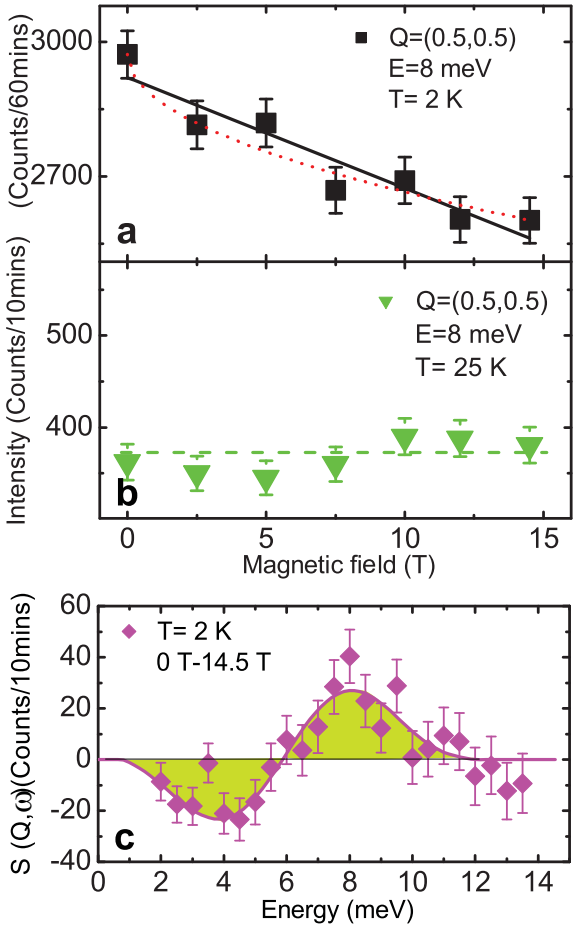

Figure 9.4: Magnetic field dependence of the resonance below and above T_c and total spin sum rule. a) The magnetic field dependence of the scattering at $\hbar\omega = 8$ meV, Q = (0.5,0.5,0), and 2 K. While the solid line is a fit using $I/I_0 = 1 - B/B_{char}$ with B_{char}32 T, the dotted line represents $I/I_0 = 1 - B/B_{char}^{1/2}$, where B_{char}66 T. b) The scattering at 25 K has no field observable field dependence. c) The difference spectrum of the neutron scattering intensities between zero and 14.5-T field at 2 K and Q = (0.5,0.5,0). The scattering should be centered around zero if spin excitations are not affected by the field. Positive scattering indicate field-induced suppression while negative scattering represents field-induced enhancement.

T field. In Ginzburg-Landau theory, magnetic field dependence of the superconducting gap $\Delta(B)$ is related to zero field gap $\Delta(0)$ via $\Delta(B)/\Delta(0) = (1 - B/B_{c2})^{1/2}$(ref. [168]). Since superconducting gap is proportional to T_c (i.e. $2\Delta \propto k_B T_c$, refs. [148, 149]), we estimate $B_{c2} = 40.3$ T using the measured T_c ($\sim$ 16 K) at 14.5 T in Fig. 9.3d and $B_{c2} = B/[1 - (T_c(14.5T)/T_c(0T)]$. This value is very close to the measured $B_{c2} = 43 - 50$ T for $BaFe_{1.8}Co_{0.2}As_2$ which has slightly higher T_cs. If the resonance energy is indeed associated with the superconducting gap energy via $\Delta = \Delta(k + Q) + \Delta(k)$, one should expect the resonance energy to shift from 7.3 meV at zero field to $\hbar\omega(14.5T) = ((T_c(14.5T))/(T_c(0T)))\hbar\omega(0T) \approx 6.0$ meV. Inspection of Fig. 9.1e shows that this is indeed the case with experimental observation of $\hbar\omega(0T)(14.5T) = 6.0 \pm 0.2$ meV. This is the most compelling evidence that the resonance is related to superconducting gap energy. Although our observation of a field-induced resonance intensity reduction is also consistent with field-suppressed superconducting gap picture [168], the multiband nature of the system [121,145–147] means that one needs a more detailed theoretical calculation to compare with the experiments. Finally, to test if the resonance directly measures electron spin singlet-to-triplet transition (from singlet spin S=0 for Cooper pairs to triplet spin S=1), we note that the Zeeman magnetic energy for a 14.5 T is at $\pm g\mu_B B\dot{S} \approx \pm 1.7$ meV (assuming the Lande factor g=2 and S=1). Experimentally, the energy widths of the resonance in Fig. 9.1e change from 4.8 ± 0.6 full-width-half-maximum (FHWM) at zero field to 5.6 ± 1 meV FHWM at 14.5 T, much less than that expected from Zeeman splitting. Therefore, while our data support the notion that the resonance is directly correlated with electron energy gap, it may not represent the long-sort single-to-triplet transition due to complication of the orbital effect for a c-axis aligned magnetic field. In any case, our data suggest that magnetic excitations are the most promising candidate for mediating electron pairing for superconductivity in iron arsenides.

Chapter 10

Conclusions

High T_c superconductivity in cuprates is still one of the biggest mysteries in condensed matter physics in spite of two decades of intensive theoretical and experimental research. Although the central issue on the "pairing glue" of the electron "Cooper pair" is still under debate, it is generally believed that phonons and magnons are two possible candidates for the mediators of "Cooper pair". The latter attracted more interest because cuprates have universal antiferromagnetic parent compounds. Neutron scattering has contributed tremendously in understanding the antiferromagnetism in cuprates for the past twenty years. However, because the magnons are much more difficult to measure and model than phonons, there is still no consensus about the role of antiferromagnetism in high T_c superconductivity. Experimentally, there are two prominent features in the antiferromagnetic fluctuations in hole doped cuprates: the "resonance mode" and "hour glass" like dispersions. Several theories attempted to explain these features in cuprates, including the itinerant model (Fermi liquid based approach) [168] and local moment model (such as "stripe model" or SO(5) theory [71, 169]), yet no consensus is reached. The discovery of high T_c superconductivity in Fe based materials greatly excited the community because it provided scientists an exciting subject to study the interplay between the high T_c superconductivity and antiferromagnetism. To tell what properties are universal for high T_c superconductivity and what properties are materials dependent could help to develop or test the theories for high T_c superconductivity in these two systems. In this thesis, we presented systematic neutron scattering studies on the magnetic properties in both electron

doped cuprates and Fe based superconductors. I hope these results could shed some new light on understanding the high T_c superconducitvity.

Shortly after the discovery of the Fe based superconductors, we performed powder and single crystal neutron diffraction measurements in the parent compounds in 1111 (CeFeAsO, PrFeAsO) and 122 ($SrFe_2As_2$) systems. They all have antiferromagnetic ground states which are similar to the cuprate parent compounds, although the detail magnetic structures are slightly different (Fig.1.1,1.3). In the case of CeFeAsO, the static antiferromagntic order is gradually suppressed upon electrons doping by replacing part of O with F. After the static order is completely suppressed, the superconductivity emerges at higher F doping, resulting a magnetic phase diagram very similar to those of cuprates. The proximity of high T_c superconductivity and a antiferromagnetic ground state in both systems thus suggests the magnetic degree of freedom is involved in the origin of high T_c.

Although the magnetic structures and magnetic phase diagrams in cuprates and Fe based superconductors are similar, the nature of the antiferromagnetism in these two systems may not be the same. Inelastic neutron scattering measurements in $CaFe_2As_2$ show that the whole spin wave spectra can be fitted with a three dimensional Heisenberg Hamiltonian. Since the Heisenberg model is a local moment approach, this result suggests the local moment physics still plays important role in the magnetic interactions in the system. On the other hand, the effective spin for the spin wave spectrum is only 0.22 which is much smaller than "spin 1" as expected by a simple local moment model for Fe^{2+}. The strikingly small moment as well as the metallic nature of the system indicates the magnetism has itinerant characters. Given the facts above, we conclude the magnetism in $CaFe_2As_2$ is neither purely local nor purely itinerant but the mix of the two, which is different from the purely local moment magnetism in cuprates. In addition, the in plane anisotropy of the exchange couplings in $CaFe_2As_2$ indicates the orbital ordering or spin orbital coupling is involved in the magnetic phase transition, which is also different from the single orbital material La_2CuO_4.

The magnetisms of the parent compounds in cuprates and Fe pnictides differ in several aspects, yet they become very similar as the systems are doped into superconducting regime. The low energy spin excitations in both Fe pnictides and cuprates are dominated by a "resonance mode". The lack of Zeeman splitting of the resonance mode under magnetic

field demonstrates that the resonance mode in $BaFe_{1.9}Ni_{0.1}As_2$ is not a collective "spin 1" excitation as suggested by a "spin exciton" model. Field dependence of the resonance energy measurements show that the resonance energy is proportional to superconducting gap, which is also similar to electron doped cuprate $Pr_{0.88}LaCe_{0.12}CuO_4$, indicating the resonance modes in these two systems have the same microscopic origin and are intimately related to the pairing mechanism.

In summary, we compared the magnetic properties in cuprates and Fe based superconductors and found a lot of important common features shared by these two systems. First of all, parent compounds of both systems have universal antiferromagnetic ground states and similar magnetic phase diagram as doping, which strongly indicates the antiferromangtism is important to high T_c superconductivity. Secondly, the spin dynamics of the parent compounds in both systems have needed high energy scales (200 to 300 meV) as the driving force to high T_c superconductivity. In addition, resonance modes dominate the low energy magnetic fluctuations in both systems. Furthermore, resonance energies are proportional to the superconducting gaps under fields. These universal properties shared by both cuprates and Fe pnictides strongly indicate the spin fluctuation is the "paring glue" of the high T_c superconductivity.

Universal properties are alway important for developing theories. On the other hand, differences sometimes can provide even more invaluable information, which can actually test our understanding on some long standing issues in cuprates. As we discussed in Chapter 8, pure local moment physics, suitable cuprate parent compounds, can not explained all the magnetic properties in the parent compounds of Fe pnictides which are obviously a more itinerant system with weaker electron correlations. However, in both systems, Femi liquid based itinerant picture can model the magnetic fluctuations (resonance modes) in superconducting samples reasonably well, which suggests the Mott physics may not be so critical in both systems in the superconducting regime. Other details observed in hole doped cuprates such as "hour glass" dispersions, stripe phase, pseudo gaps, which were believed to be fundamental to high T_c superconductivity, may not be so critical as such properties are absent in electron doped cuprates and Fe pnictides.

Bibliography

Bibliography

[1] H. Kamerlimgh Onnes. Leiden Comm, 120b, 122b, 124c (1911).

[2] W. Meissner and R. Ochsenfeld, Naturwissenschaften **21**, 787 (1933).

[3] J. Bardeen, L. N. Cooper, and J.R. Schrieffer, Phys. Rev. **108**, 1175 (1957).

[4] J. G. Bednorz and K. A. Muller, Z. Phys. B-Condens. Mat. 64, 189 (1986).

[5] M. K. Wu *et al.*, Phys. Rev. Lett. **58**, 908 (1987).

[6] A. Schilling *et al.*, Nature **363**, 56 (1993).

[7] Y. Kamihar *et al.* J. Am. Chem. Soc. **130**, 3296 (2008).

[8] X. H. Chen *et al.* Nature. **453**, 761 (2008).

[9] G. F. Chen *et al.* Phys. Rev. Lett. **100**, 247002 (2008).

[10] Z. A. Ren *et al.* Euro. Phys. Lett. **83**, 17002 (2008).

[11] Jan-Willem G. Bos *et al.* Chem. Commun. **2008**, 3634 (2008).

[12] C. de la Cruz *et al.* Nature **453**, 899 (2008).

[13] D. Vaknin,*et al.*Phys. Rev. Lett. **58**, 2802 (1987).

[14] K. Haule,*et al.*Phys. Rev. Lett. **100**, 226402 (2008).

[15] G. L. Squires, Introduction to the Theory of Thermal Neutron Scattering, Dover Publications (1996).

[16] G. Shirane, S. M. Shapiro, and J. M. tranquada, Neutron Scattering with a Triple-Axis Spectrometer: Basic Techniques, Cambridge University Press (2002).

[17] Stephen W. Lovesey, The Theory of Neutron Scattering from Condensed Matter (Volumes I and II), Oxford University Press, New York (1986).

[18] K. Yamada,*et al.*Solid State Comms. **64**, 753 (1987).

[19] L. J. D. Jongh, Solid State Comms. **65**, 963 (1988).

[20] T. Kaplan,*et al.*J. App. Phys. **69**, 5382 (1991).

[21] S. M. Hayden,*et al.*Phys. Rev. Lett. **76**, 1344 (1996).

[22] R. Coldea,*et al.*Phys. Rev. Lett. **86**, 5377 (2001).

[23] J. Rossat-Mignod,*et al.*Physica C **185**, 86 (1991).

[24] H. F. Fong,*et al.*Nature **398**, 588 (1999).

[25] H. He,*et al.*Phys. Rev. Lett. **86**, 1610 (2001).

[26] H. He,*et al.* Science **295**, 1045 (2002).

[27] S. D. Wilson,*et al.*Nature **442**, 59 (2006).

[28] R.J. Birgeneau,*et al.*J. Phys. Soc. Jpn **75**,111003 (2006).

[29] C. Stock,*et al.*Phys. Rev. B. **71**, 024522 (2005).

[30] M. A. Kastner *et al.*, Rev. Mod. Phys. **70**, 897 (1998).

[31] D. J. Scalapino, Science **284**, 1282 (1999).

[32] H. F. Fong *et al.*, Phys. Rev. B **61**, 14733 (2000).

[33] Pengcheng Dai *et. al.*, Phys. Rev. B **63**, 054525 (2001).

[34] H. Woo *et al.*, Nature Physics **2**, 600 (2006).

[35] K. Yamada *et al.*, Phys. Rev. Lett. **75**, 1626 (1995).

[36] T. E. Mason *et al.*, Phys. Rev. Lett. **77**, 1604 (1996).

[37] J. M. Tranquada *et. al.*, Nature (London) **429**, 534 (2004).

[38] N. B. Christensen *et. al.*, Phys. Rev. Lett. **93**, 147002 (2004).

[39] B. Vignolle *et al.*, Nature Physics **3**, 163 (2007).

[40] J. M. Tranquada *et al.*, Phys. Rev. B **69**, 174507 (2004).

[41] Y. Tokura, H. Takagi, and S. Uchida, Nature (London) **337**, 345 (1989).

[42] K. Yamada *et al.*, Phys. Rev. Lett. **90**, 137004 (2003).

[43] H. J. Kang *et al.*, Nature (London) **423**, 522 (2003).

[44] A. T. Boothroyd *et. al.*, Phys. Rev. B **45**, 10075 (1992).

[45] S. D. Wilson *et al.*, Phys. Rev. B **74**, 144514 (2006).

[46] L. Shan *et al.*, cond-mat/0703256.

[47] S. A. Kivelson *et al.*, Rev. Mod. Phys. **75** 1201 (2003).

[48] J. Zaanen *et al.*, Phil. Mag. B **81**, 1485 (2001).

[49] M. Vojta, T. Vojta, and R. K. Kaul, Phys. Rev. Lett. **97**, 097001 (2006).

[50] I. Ermin *et al.*, Phys. Rev. Lett. **94**, 147001 (2005).

[51] M. Eschrig, Adv. Phys. **55**, 47 (2006).

[52] I. Ermin *et al.*, cond-mat/0702375.

[53] F. Krüger *et al.*,Phys. Rev. B **76**,094506 (2007).

[54] F. C. Niestemski *et al.,* Unpublished

[55] G. M. Eliashberg, JETP **11**, 696 (1960).

[56] J. R. Schrieffer, D. J. Scalapino, and J. W. Wilkins,Phys. Rev. Lett. **10**, 336 (1963).

[57] W. L. McMillan and J. M. Rowell, Phys. Rev. Lett. **14**, 108 (1965).

[58] T. A. Maier, D. Poilblanc, and D. J. Scalapino, arXiv:0801.4506v1.

[59] P. W. Anderson, Science **316**, 1705 (2007).

[60] P. Monthoux, D. Pines, and G. G. Lonzarich, Nature (London) **450**, 1177 (2007).

[61] J. Lee *et al.,* Nature (London) **442**, 546 (2006).

[62] F. C. Niestemski *et al.,* Nature (London) **450**, 1058 (2007).

[63] J. Chang *et al.*, Phys. Rev. Lett. **98**, 077004 (2007).

[64] C. Stock *et al.*, Phys. Rev. B. **73**, 100504(R) (2006).

[65] J.P. Ismer *et al.*, Phys. Rev. Lett. **99**, 047005 (2007).

[66] S. Li *et al.*, Phys. Rev. B. **77**, 014523 (2008).

[67] T. Dahm *et al.*, Nat. Phys. **5**, 217 (2009).

[68] A. T. Boothroyd *et al.*, Phys. Rev. B. **45**, 10075 (1992).

[69] T. Moriya Spin Fluctuations in Itinerant Electron Magnetism (Springer, 1985).

[70] P. A. Lee *et al.*, Rev. Mod. Phys. **78**, 17-85 (2006).

[71] J. M. Tranquada, in Handbook of High-Temperature Superconductivity, edited by J. R. Schrieffer and J. S. Brooks (Springer, New York, 2007), p. 257.

[72] M. Fujita *et al.*, Phys. Rev. B **67**, 014514 (2003).

[73] W. Yu *et al.*, Phys. Rev. B **76**, 020503(R) (2007).

[74] H. H. Wen *et al.* Euro. Phys. Lett. **82**, 17009 (2008).

[75] M. Rotter *et al.*, Phys. Rev. Lett. **101**, 107006 (2008).

[76] Q. Si,*et al.*,Phys. Rev. Lett. **101**, 076401.

[77] C. Fang *et al.*, Phys. Rev. B **77**, 224509 (2008).

[78] C. Xu *et al.*, Phys. Rev. B **78**, 020501(R).

[79] I. I. Mazin *et al.*, Phys. Rev. Lett. **101**, 057003 (2008).

[80] Z. P. Yin, *et al.*, Phys. Rev. Lett. **101**, 057001 (2008).

[81] F. J. Ma Z. Y. Lu, Phys. Rev. B **78**, 033111 (2008).

[82] M. Tegel *et al.*, Preprint at http://arxiv.org/abs/0805.1208

[83] T. M. McQueen *et al.*, Phys. Rev. B **78**, 024521 (2008).

[84] M. Rotter, *et al.,* Phys. Rev. B **78**, 020503(R)

[85] T. Nomura *et al.,* Preprint at http://arxiv.org/abs/0804.3569

[86] S. A. J. Kimber *et al.,* Preprint at http://arxiv.org/abs/0807.4441v1

[87] J. Zhao, *et al.,* Phys. Rev. B **78** 132504 (2008)

[88] Y. Chen, *et al.,* Phys. Rev. B **78**, 064515 (2008)

[89] J. Dong,*et al.,* Euro. Phys. Lett. **83**, 27006

[90] S. Komura *et al.,* J. Phys. Soc. Jpn. **23**, 171 (1967).

[91] E. Facett Rev. Mod. Phys. **60**, 209 (1988).

[92] C. L. Zhang, *et al.,* Preprint at http://arxiv.org/abs/0808.2134

[93] J. S. Wu *et al.,* Preprint at http://arxiv.org/abs/0805.2167v1

[94] T. Yildirim, Phys. Rev. Lett. 101, 057010 (2008)

[95] Y. Kamihara, *et al.,* J. Am. Chem. Soc. 128, 10012 (2006).

[96] Y. Qiu *et al.,* Preprint at http://arxiv.org/abs/0806.2195v4

[97] C. Tarantini *et al.,* Preprint at http://arxiv.org/abs/0805.4445v1

[98] H. Luetkens, *et al.,* Preprint at http://arxiv.org/abs/0806.3533

[99] S. Margadonna, *et al.,* Preprint at http://arxiv.org/abs/0806.3962

[100] A. J. Drew *et al.,* Preprint at http://arxiv.org/abs/0807.4876

[101] Q. Huang *et al.,* Phys. Rev. B 78 054529 (2008)

[102] R. H. Liu *et al.,* Phys. Rev. Lett. (in the press), Preprint at http://arxiv.org/abs/0804.2105

[103] M. Rotter,M. Tegel D.Johrendt, arXiv.org:0805.4630 (2008).

[104] G. F. Chen, *et al.*, arXiv.org:0806.1209 (2008).

[105] H.-H. Klauss, arxiv.org/abs/0805.0264 .

[106] Jun Zhao, *et al.*, Nature Materials 7, 953-959 (2008).

[107] M. A. McGuire, A. D. Christianson, A. S. Sefat, B. C. Sales, M. D. Lumsden, arxiv.org/abs/0806.3878.

[108] Q. Huang, Y. Qiu, Wei Bao, J.W. Lynn, M.A. Green, Y. Chen, T. Wu, G. Wu, X.H. Chen, arxiv.org/abs/0806.2776.

[109] Jun Zhao, W. Ratcliff II, J. W. Lynn, Phys. Rev. B 78, 140504 (R) (2008).

[110] A.I. Goldman, D.N. Argyriou, B. Ouladdiaf,P.C. Canfield, R. J. McQueeney, arxiv.org/abs/0807.1525.

[111] J. Drew, G. Wu, X. H. Chen, I. Watanabe, V. K. Malik, A. Dubroka, K. W. Kim, M. Roessle, and C. Bernhard, arxiv.org/abs/0805.1042.

[112] Z. A. Ren, J. Yang, W. Lu, W. Yi, G. C. Che, X. L. Dong, L. L. Sun, Z.X. Zhao, Materials Research Innovations 12, 1 (2008).

[113] M. Rotter *et al.*, Preprint at http://arxiv.org/abs/0805.4021

[114] K. Sasmal *et al.*, Preprint at http://arxiv.org/abs/0806.1301v2

[115] C. Krellner *et al.*, Preprint at http://arxiv.org/abs/0806.1043v1

[116] J.-Q. Yan *et al.*, Preprint at http://arxiv.org/abs/0806.2711v1

[117] G. F. Chen *et al.*, Preprint at http://arxiv.org/abs/0806.2648v2

[118] K. Sasmal *et al.*, arXiv:0806.1301.

[119] G. Wu *et al.*, arXiv:0806.4279.

[120] A.I. Goldman *et al.*, arXiv.org:0807.1525.

[121] I. I. Mazin *et al.*, arXiv.org:0806.1869v2.

[122] E. Fawcett, Rev. Mod. Phys. **60**, 209 (1988).

[123] F. J. Ma, Z. Y. Li, and T. Xiang, arXiv.org:0804.3370v3.

[124] A. Jesche *et al.*, arXiv.org:0807.0632v1.

[125] D. X. Yao and E. W. Carlson, Phys. Rev. B (in the press), arXiv.org:0804.4115v4.

[126] F. J. Ma, Z.-Y. Lu, and T. Xiang, arXiv.org:0806.3526v1.

[127] L. X. Yang *et al.*, arXiv.org:0806.2627v2.

[128] I. I. Mazin M. D. Johannes, Nature Physics **5**, 141-145 (2009).

[129] T. Kariyado Ogata, Preprint at http://arxiv.org/abs/0812.4664v1

[130] M. J. Han, Q. Yin, W. E. Pickett S. Y. Savrasov Phys. Rev. Lett. (in press), Preprint at http://arxiv.org/abs/0811.0034v2

[131] T. Yildirim, Physica C (in press), Preprint at http://arxiv.org/abs/0902.3462v1

[132] Y. Endoh, *et al.*, Magnetic excitations in metallic ferro- and antiferromagnets J. Phys. Soc. Jpn. **75**, 111002

[133] J. H. Dai, Q. Si, J. S. Zhu E. Abrahams, , Preprint at http://arxiv.org/abs/0808.0305v3

[134] E. Manousakis,,J. Ren, S. Meng, E. Kaxiras, Preprint at http://arxiv.org/abs/0902.3450

[135] J. Zhao *et al.*,. Phys. Rev. Lett. **101**, 167203 (2008).

[136] R. A. Ewings *et al.*, Phys. Rev. B **78**, 220501(R) (2008).

[137] R. J. McQueeney *et al.*, Phys. Rev. Lett. **101**, 227205 (2008).

[138] K. Matan, R. Morinaga, K. Iida T. Sato, J. Phys. Rev. B **79**, 054526 (2009).

[139] S. O. Diallo, *et al.*, Preprint at http://arxiv.org/abs/0901.3784

[140] G. Wu, *et al.*, Journal of Physics: Condensed Matter **20**, 422201 (2008).

[141] T. G. Perring, *et al.*, Phys. Rev. Lett. **87**, 217201 (2001).

[142] F. Ye *et al.* Phys. Rev. B **75**, 144408 (2007).

[143] J. Lorenzana, G. Seibold R. Coldea, Phys. Rev. B **72**, 224511 (2005).

[144] W. Z. Hu *et al.*, Phys. Rev. Lett. **101**, 257005 (2008).

[145] A. V. Chubukov Physica C **469**, 640-650 (2009).

[146] F. Wang, *et al.*, Phys. Rev. Lett. **102**, 047005 (2009).

[147] K. Seo, B. A. Bernevig, J. P. Hu, Phys. Rev. Lett. **101**, 206404 (2008).

[148] H. Ding, *et al.*, EPL **83**, 47001 (2008).

[149] V. B. Zabolotnyy, *et al.*, Nature **457**, 569-572 (2009).

[150] K. Terashima, *et al.*, PNAS **106**, 7330-7333 (2009).

[151] P. Vilmercati, *et al.*, Phys. Rev. B **79**, 220503(R) (2009).

[152] A. D. Christianson, *et al.*, Nature **456**, 930-932 (2008).

[153] M. D. Lumsden, *et al.*, Phys. Rev. Lett. **102**, 107005 (2009).

[154] S. Chi *et al.*Phys. Rev. Lett., **102**, 107006 (2009).

[155] S. Li, *et al.*, Phys. Rev. B **79**, 174527 (2009).

[156] D. S. Inosov, *et al.*,http://arxiv.org/abs/0907.3632v1

[157] T. A. Maier, D. J. Scalapino, Phys. Rev. B **78**, 020514(R) (2008).

[158] T. A. Maier, S. Graser, D. J. Scalapino P.Hirschfeld Phys. Rev. B **79**, 134520 (2009).

[159] M. M. Korshunov, I. Eremin, Phys. Rev. B **78**, 140509(R) (2008).

[160] K. Seo, C. Fang, B. A. Bernevig J. Hu, Phys. Rev. B **79**, 235207 (2009).

[161] P. Dai, H. A. Mook, G. Aeppli,, S. M. Hayden, Nature **406**, 965-968 (2000).

[162] Y. Yin, *et al.*, Phys. Rev. Lett. **102**, 097002 (2009).

[163] A. Yamamoto, *et al.*., App. Phys. Lett. 94, 062511 (2009).

[164] B. Lake, et al., Science **291**, 1759-1762 (2001).

[165] J. Chang, *et al.*, Phys. Rev. Lett. **102**, 177006 (2009).

[166] S. D.Wilson *et al.*,. PNAS **104**, 15259-15263 (2007).

[167] D. Haug, *et al.* Phys. Rev. Lett. **103**, 017001 (2009).

[168] M. Eschrig M. R. Norman, Phys. Rev. B **64**, 134509 (2001).

[169] E. Demler, W. Hanke, and Shou-Cheng Zhang, Rev. Mod. Phys. **76**, 909 (2004).

Vita

Jun Zhao was born on May 3, 1980 in Chenzhou, Hunan Province, China. He graduated from Guangdong Beijiang High School in Shaoguang, Guangdong Province in 1998. He received a Bachelor of Science degree in Physics from Tsinghua University in July, 2002. He studied in Institute of Physics, Chinese Academy of Sciences in Prof. Zhongxian Zhao's group from 2002 to 2005 and revceived his M.S. in Physics. In 2005, he came to U.S. and attended the graduate program in physics at the University of Tennessee and expects to receive his Doctorate of Philosophy degree in physics in May of 2010.